

AD E 300 471

DNA 4688F

DDC FILE COPY
AD A0 66974

STATUS REPORT ON WEPH CODE MODELING-1978

**General Electric Company—TEMPO
816 State Street
Santa Barbara, California 93101**

1 November 1978

Final Report for Period 15 October 1977—1 November 1978

CONTRACT No. DNA 001-78-C-0043

**APPROVED FOR PUBLIC RELEASE;
DISTRIBUTION UNLIMITED.**

**THIS WORK SPONSORED BY THE DEFENSE NUCLEAR AGENCY
UNDER RDT&E RMSS CODE B322078484 S89QAXHE04338 H2560D.**

**Prepared for
Director
DEFENSE NUCLEAR AGENCY
Washington, D. C. 20305**

DDC
APR 6 1979
**REPRODUCED BY
NATIONAL TECHNICAL
INFORMATION SERVICE
U. S. DEPARTMENT OF COMMERCE
SPRINGFIELD, VA. 22161**

79 02 21 011

128

UNCLASSIFIED

SECURITY CLASSIFICATION OF THIS PAGE (When Data Entered)

REPORT DOCUMENTATION PAGE		READ INSTRUCTIONS BEFORE COMPLETING FORM
1. REPORT NUMBER DNA 4688F	2. GOVT ACCESSION NO.	3. RECIPIENT'S CATALOG NUMBER
4. TITLE (and Subtitle) STATUS REPORT ON WEPH CODE MODELING — 1978		5. TYPE OF REPORT & PERIOD COVERED Final Report for Period 15 Oct 77—1 Nov 78
7. AUTHOR(s) Warren S. Knapp		6. PERFORMING ORG. REPORT NUMBER GE78TMP-69
9. PERFORMING ORGANIZATION NAME AND ADDRESS General Electric Company—TEMPO 816 State Street Santa Barbara, California 93101		8. CONTRACT OR GRANT NUMBER(s) DNA 001-78-C-0043
11. CONTROLLING OFFICE NAME AND ADDRESS Director Defense Nuclear Agency Washington, D.C. 20305		10. PROGRAM ELEMENT, PROJECT, TASK AREA & WORK UNIT NUMBERS NWED Subtask S99QAXHE043-36
14. MONITORING AGENCY NAME & ADDRESS (if different from Controlling Office)		12. REPORT DATE 1 November 1978
		13. NUMBER OF PAGES 132
		15. SECURITY CLASS (of this report) UNCLASSIFIED
		15a. DECLASSIFICATION/DOWNGRADING SCHEDULE
16. DISTRIBUTION STATEMENT (of this Report) Approved for public release; distribution unlimited.		
17. DISTRIBUTION STATEMENT (of the abstract entered in Block 20, if different from Report)		
18. SUPPLEMENTARY NOTES This work sponsored by the Defense Nuclear Agency under RDT&E RMSS Code B322078464 S99QAXHE04336 H2590D.		
19. KEY WORDS (Continue on reverse side if necessary and identify by block number) Nuclear Weapon Effects Hydrodynamic Motion Wind Fields Atmospheric Chemistry Atmosphere Ionosphere		
20. ABSTRACT (Continue on reverse side if necessary and identify by block number) This report describes phenomenology and atmospheric models developed for the WEPH code during 1978. Models described include atmosphere and ionosphere models, fireball wake and heave models, atmospheric chemistry models, and late-time debris models.		

SUMMARY

The WEPH code is a computer program that provides calculations of electromagnetic propagation in nuclear disturbed environments. This report describes phenomenology and atmospheric models developed for the WEPH code during 1978. Models described include atmosphere models (Section 1), ionosphere models (Section 2), fireball wake and heave models (Section 3), atmospheric chemistry models (Section 4), and late-time debris models (Section 5).

ACCESSION NO.		
NTIS	Write Section <input checked="" type="checkbox"/>	
ORGANIZATION	CI	
IDENTIFICATION		
BY		
DATE		
DATE	DATE	SPECIAL
A		

79 02 21 011

TABLE OF CONTENTS

<u>Section</u>	<u>Page</u>
SUMMARY	1
1 AMBIENT ATMOSPHERE MODEL	7
INTRODUCTION	7
REFERENCES	25
2 AMBIENT IONOSPHERE AND ION NEUTRAL COLLISION FREQUENCY MODELS	26
INTRODUCTION	26
CURRENT WEPH MODELS	27
D-REGION IONOSPHERE MODELS	27
Theoretical Models	27
Empirical Models for Low Frequency Propagation	30
E- AND F-REGION IONOSPHERE MODELS	33
Theoretical Models	33
Empirical Models for HF Propagation	35
NEW IONOSPHERE MODEL	36
General	36
E- and F-Region Model	40
D-Region Model	43
Examples of Model Output	45
New Ion-Neutral Collision Frequency Model	49
COMPARISONS WITH PROPAGATION DATA	53
ELF Propagation Data	53
VLF Propagation Data	59
HF Propagation Data	65
SUMMARY	68

<u>Section</u>	<u>Page</u>
REFERENCES	70
3 HEAVE MODEL	72
INTRODUCTION	72
Fireball Wake Model	72
REFERENCES	78
4 CHEMISTRY MODELS	79
INTRODUCTION	79
D-REGION CHEMISTRY MODEL	79
E- AND F-REGION CHEMISTRY MODEL	87
REFERENCES	96
5 POST STABILIZATION DEBRIS MODELS	97
INTRODUCTION	97
NUMERICAL MODEL	97
ANALYTIC MODEL	102
REFERENCES	106
 <u>APPENDIX</u>	
A REACTIONS AND REACTION RATE COEFFICIENTS USED IN D-REGION CHEMISTRY MODEL	107
B REACTIONS AND REACTION RATE COEFFICIENTS USED IN E- AND F-REGION AND HEATED REGION CHEMISTRY MODELS	117
C PROBABILITY DISTRIBUTION OF THE ABSOLUTE DIFFER- ENCE OF TWO INDEPENDENT RANDOM VARIABLES	123

LIST OF ILLUSTRATIONS

<u>Figure</u>		<u>Page</u>
1-1	Illustration of profiles obtained from interpolation model.	10
2-1	Daytime D-region ionization rates.	28
2-2	Parabolas for daytime ionosphere and selected transition altitudes for use in Booker formulation.	42
2-3	Comparison of current and new ionosphere models for daytime conditions.	46
2-4	Comparison of current and new ionosphere models for nighttime conditions.	47
2-5	D-region ionization, 30 degrees latitude, 15 June 1961.	48
2-6	Comparisons of daytime profiles obtained with new ionosphere model.	50
2-7	Comparisons of nighttime profiles obtained with new ionosphere model.	51
2-8	Electron density profiles used for nighttime ELF calculations.	55
2-9	Electron density profiles used for daytime ELF calculations.	56
2-10	Ion-neutral collision frequency profiles used for ELF calculations.	57
2-11	Propagation from San Francisco to Hawaii, May 18-19, 1965 (NPM 24 kHz).	60
2-12	Propagation from Utah to Hawaii (daytime, February 1974), (28 kHz).	61

<u>Figure</u>	<u>Page</u>
2-13 Daytime electron density profiles used for VLF calculations.	62
2-14 Propagation from Ontario, California to Hawaii (nighttime, 7 February 1969), (28 kHz).	64
2-15 Nighttime electron density profile used for VLF calculation.	65
3-1 Lagrangian contours at burst time.	74
3-2 Lagrangian contours adjusted for fireball rise by the wake model.	74
4-1 Changes in the steady-state odd oxygen concentration at 60 km as a function of the odd nitrogen concentration.	82
4-2 Changes in the steady-state odd oxygen concentration as a function of $[O]_0/\xi_0$, $\delta = 4 \times 10^{10} \text{ cm}^{-3}$.	83
4-3 Changes in the steady-state odd oxygen concentration at 60 km as a function of $[NO_2]_0/\delta_0$, $\delta = 4 \times 10^{10} \text{ cm}^{-3}$.	83
4-4 Current and modified values for ambient daytime NO_2 concentration.	85
4-5 Reduction in odd oxygen as a function of altitude, $N_0 = 10^{11} \text{ ion pairs cm}^{-3}$.	86
4-6 Nitrogen vibrational temperature following ionization impulse of $10^{11} \text{ ion pairs cm}^{-3}$.	88
4-7 Comparison of nitrogen vibrational temperature at interface between D-region and E- and F-region models.	90
5-1 Comparison of current and revised numerical models.	103
5-2 Comparison of current and revised analytic models.	105

LIST OF TABLES

<u>Table</u>	<u>Page</u>
1-1 Conditions for Tables 1-2 and 1-3.	12
1-2 Revised ambient daytime atmosphere species and temperatures.	13
1-3 Revised ambient nighttime atmosphere species and temperatures.	19
2-1 Predicted values of h_w and α_w from Equations 2-1 and 2-2 for selected conditions (quiet magnetic absorption index).	32
2-2 Effective values of h_w and α_w for daytime obtained from VLF and LF propagation measurements.	34
2-3 Effective values of h_w and α_w for nighttime obtained from VLF and LF propagation measurements, Midlatitude (Pacific), winter.	34
2-4 E- and F-region data for March, 40 degrees longitude.	37
2-5 E- and F-region data for June, 40 degrees longitude.	38
2-6 E- and F-region data for December, 40 degrees longitude.	39
2-7 Scaling parameters for use in Booker formulation.	41
2-8 ELF calculations.	54
2-9 15 mHz one-way vertical absorption, noon.	67
3-1 Comparison of electron density and initial air altitude at 240 seconds after burst on the burst axis with and without wake model.	76
4-1 Ambient species concentrations (cm^{-3}) for H, OH, and HO ₂ used in ROSCOE.	81

SECTION 1 AMBIENT ATMOSPHERE MODEL

INTRODUCTION

The ambient atmosphere models used in the current WEPH code are essentially the same as those developed by Science Applications Incorporated (SAI) for ROSCOE (References 1-1 and 1-2). Quantities modeled include pressure, density, temperature, density scale height, and major and minor neutral species.

The altitude region is divided into a low altitude region ($h \leq 120$ km) where the major and inert species are thoroughly mixed so that the fractional concentrations are (almost) altitude independent, and a high-altitude region ($h \geq 120$ km) where diffusive separation prevails. In the low-altitude region a day-night change in certain species concentrations is provided for but there are no changes with season, latitude, or solar cycle. In the high-altitude region the species and properties are modeled as a function of solar flux.

Recently, SAI revised the ROSCOE atmosphere model for use in optical predictions (Reference 1-3). The revision includes:

1. Addition of new species; $N(^2D)$, N_2O , CO , CH_4 , $O(^1D)$, H , OH , HO_2
2. Provision for determining atmospheric temperature below 120 km as a function of latitude and season
3. Provision for determining the species O_3 , H_2O , N_2O , $N(^4S)$, $N(^2D)$, and NO as a function of latitude and season. Provision for determining the species $N(^4S)$, $N(^2D)$, and NO as a function of local time.

Most of the above changes have been incorporated into a revised WEPH code atmosphere model (the species CO and CH₄ are not modeled). In addition, the structure of the revised WEPH code atmosphere model and the smoothing procedures used were changed to facilitate use in propagation codes.

In the WEPH Code atmosphere model (and also in the ROSCOE model) initialization calculations are made for a given location, date, and time prior to determining atmospheric properties at specific altitudes. The initialization calculations require use of a number of special routines that are only used during initialization. In the current model the initialization calculations and the atmospheric evaluation calculations are made from the same routine resulting in all the atmosphere routines being present (in core) when atmospheric properties are calculated. In the revised atmospheric model the initialization calculations and the evaluation calculations are separated. This allows overlaying the initialization routine to reduce core storage when initialization is only done once for a given region.

A major objective in the development of the atmosphere model by SAI was obtaining continuous derivatives for modeled quantities. To this end polynomial fits are used to describe quantities between specified altitudes. The use of high order polynomials (12th degree in many cases) can lead to numerical difficulties in solving for the coefficients and in subsequent evaluation of the polynomial for some machines. As described in Section 2, Booker (Reference 1-4) has suggested use of an exponential formulation for fitting multi-region ionospheric profiles of electron density that provides continuous derivatives. The formulation suggested by Booker (see Equation 2-10 in Section 2) can be used as an interpolation procedure by choosing the smoothing scales so that the effects of smoothing outside the interpolation region are negligible within the interpolation region. For the atmosphere model the smoothing scale was chosen as one-tenth the distance between data points.

Thus,

$$B_n = \frac{10}{z_{n+1} - z_n} \quad (1-1)$$

For this choice of B_n a 4-point interpolation can be used. Let $N(z)$ be specified at $z_1, z_2, z_3,$ and z_4 . Then $N(z)$ between z_2 and z_3 is given by

$$\begin{aligned} \ln[N(z)] = & \ln[N_r] + A_1(z_1 - z_r) \\ & + (A_2 - A_1) \left\{ f(z - z_2, B_2) - f(z_r - z_2, B_2) \right\} \\ & + (A_3 - A_2) \left\{ f(z - z_3, B_3) - f(z_r - z_3, B_3) \right\} \end{aligned} \quad (1-2)$$

$$z_2 \leq z \leq z_3$$

where

$$A_1 = \frac{\ln \left[\frac{N(z_2)}{N(z_1)} \right]}{z_2 - z_1}$$

$$A_2 = \frac{\ln \left[\frac{N(z_3)}{N(z_2)} \right]}{z_3 - z_2}$$

$$A_3 = \frac{\ln \left[\frac{N(z_4)}{N(z_3)} \right]}{z_4 - z_3}$$

$$N_r = N(z_1)$$

$$z_r = z_1$$

Figure 1-1 shows values obtained by interpolation between data given at 5 km altitude intervals. Note that the interpolated values do not exactly reproduce the data points since this is where the smoothing

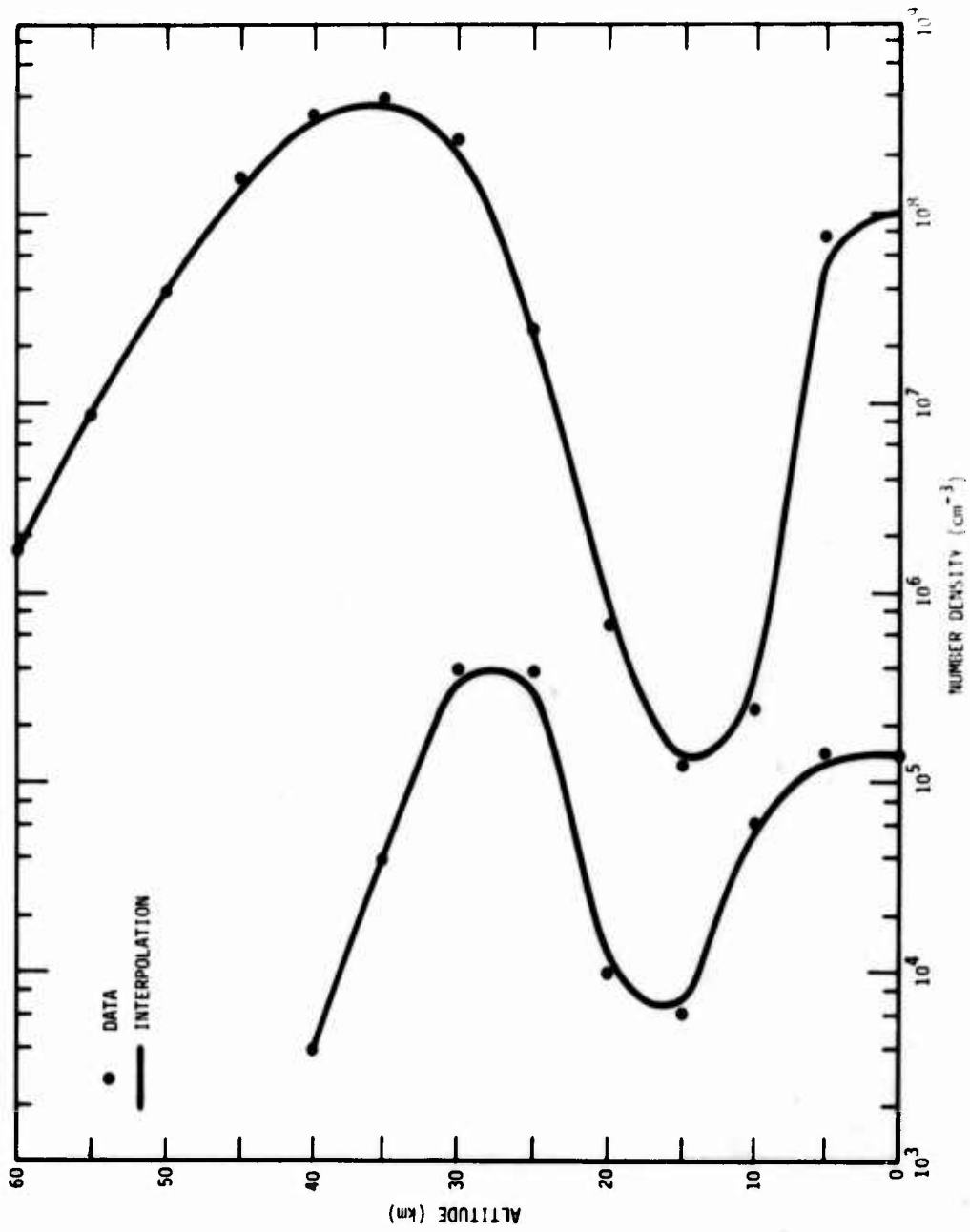


Figure 1-1. Illustration of profiles obtained from interpolation model.

is done to provide continuous derivatives. If the derivative of $N(z)$ is required, it can be obtained from

$$\frac{dN(z)}{dz} = N(z) \left\{ A_1 + \frac{A_2 - A_1}{1 + \exp[-(z-z_2)B]} + \frac{A_3 - A_2}{1 + \exp[-(z-z_3)B]} \right\} \quad (1-3)$$

In the WEPH code (and ROSCOE) chemistry models effective photodissociation rates for photodissociation of O_2 , O_3 , and NO_2 are determined from ambient species concentrations. As discussed in Section 4 the use of the nominal SAI model for NO_2 results in a negative effective photodissociation rate for NO_2 above about 50 km. In order to prevent this the ambient daytime NO_2 is limited to a value determined from a nominal photodissociation rate ($6.8 \times 10^{-3} \text{ sec}^{-1}$) used by Schiebe in the DCHEM code.

Tables 1-2 and 1-3 show results obtained with the revised atmospheric model for conditions shown in Table 1-1 (see Section 6 in Reference 1-1 for values obtained with the current atmospheric model). Potentially significant changes to species concentrations previously modeled are the reduction in NO and H_2O in the D-region. The NO concentration has been reduced by about a factor of 5 and the H_2O concentration has been reduced by a factor of 2 in the lower D-region to about a factor of 5 in the upper D-region. Results from the ambient ionosphere model are also shown in Tables 1-2 and 1-3. The quantities VEM, VIM, and VEI shown in Tables 1-2 and 1-3 are the electron-neutral, ion-neutral, and electron-ion collision frequencies, respectively. Changes to the ambient ionosphere and ion-neutral collision frequency models are described in Section 2.

Table 1-1. Conditions for Tables 1-2 and 1-3.

	<u>Table 1-2</u>	<u>Table 1-3</u>
North Latitude (deg)	45	45
East Longitude (deg)	235	235
Year	1977	1977
Month	September	September
Day	1	2
Hour	12:00	0:00
Solar Flux ($\times 10^{22} \text{ W m}^{-2} \text{ Hz}^{-1}$)	158	158

Table 1-2. Revised ambient daytime atmosphere species and temperatures.

ALT	N2 1/CC	O2 1/CC	CO 1/CC	NO 1/CC	NO2 1/CC	CO2 1/CC	O(1D) 1/CC	N(4S) 1/CC	N(2D) 1/CC	O3 1/CC	H2O 1/CC
	C2(1D) 1/CC	M 1/CC	CH 1/CC	HO2 1/CC	W2O 1/CC	NO 1/CC		PRESSURE DYN/CM2	DENSITY GRAMS/CC	DEN SC MT KM	TEMP DEG K
	NEM 1/SEC	VIM 1/SEC	WEI 1/SEC	O 1/CC SEC	E 1/CC	Mo 1/CC		ALPHAD CC/SEC	ALPMAI CC/SEC	A 1/SEC	D 1/SEC
0.	1.99E 19	5.37E 18	5.80E 02	1.00E 10	2.50E 10	9.14E 15	1.00E-02	4.08E 00	7.35E-04	6.91E 11	9.00E 13
	2.60E 06	7.00E-03	1.70E 06	1.00E 05	5.10E 12			1.01E 04	1.22E-03	1.00E 01	2.80E 02
	1.53E 11	6.00E 09	3.14E-09	3.53E-01	1.71E-07			6.04E-04	2.87E-04	6.31E 07	2.90E-02
	1.18E 19	3.19E 18	6.24E 03	3.45E 09	7.92E 09			8.39E 00	1.95E-05	6.85E 11	5.77E 13
	8.81E 06	7.70E-03	1.80E 06	7.07E 05	2.62E 12			5.83E 05	7.27E-04	9.38E 00	2.61E 02
	6.22E 10	3.39E 09	4.18E-08	3.68E 08	2.00E-06			6.99E-06	2.20E-04	2.02E 07	2.94E-02
	2.69E 07	1.80E 18	2.59E 04	1.33E 09	1.59E 09			1.73E 01	4.64E-05	1.14E 12	3.60E 13
	4.11E 10	1.80E 09	3.26E-07	1.60F 08	1.55E 12			2.72E 01	4.09E-04	8.09E 00	2.32E 02
	3.29E 18	9.90E 17	1.69E 05	6.67E 08	1.37E-05			6.10E-06	1.68E-04	5.58E 06	2.72E-02
	1.29E 18	1.89E-02	1.16E 06	6.64E 04	8.83E 11			3.55E 01	1.16E-04	2.57E 12	1.79E 13
	1.91E 10	8.63E 04	2.07E 06	1.14F 01	8.24E-05			1.27E 05	2.03E-04	6.61E 00	2.17E 02
	1.50E 18	4.05E 17	1.06E 06	7.70E 08	1.80E 09			6.10E-04	1.00E-04	1.26E 04	2.69E-02
	8.76E 08	5.44E-02	1.52E 06	1.13E 07	2.64E 11			5.78E 04	9.24E-05	4.41E 12	8.44E 12
	8.72E 09	3.94E 08	1.10E-05	7.90E 00	4.54E-04			6.10E-04	6.97E-07	6.30E 00	2.18E 02
	8.00E 17	1.84E 17	2.71E 06	1.59E 04	2.36E 09			6.10E-04	4.97E-07	2.63E 05	2.76E-02
	1.28E 09	3.29E-01	4.91E 07	1.48E 07	6.90E 10			2.67E 04	4.19E-04	6.08E 12	3.79E 12
	4.03E 09	1.80E 08	4.91E-05	4.19E 00	2.10E-03			6.10E-06	2.45E-07	5.55E 04	2.82E 02
	3.11E 17	8.43E 16	4.67E 07	1.99E 00	2.30E 09			3.99E 02	1.89E-03	2.52E 12	1.64E 12
	2.78F 09	3.18E 00	3.99E 04	1.59E 07	1.61E 10			1.26E 04	1.92E-05	6.43E 00	2.28E 02
	1.90E 09	8.37E 07	1.44E-08	1.69E 00	8.80E-03			6.10E-04	1.39E-07	1.21E 04	2.83E-02
	1.44E 17	3.89E 16	2.53E 08	1.71E 09	1.19E 09			6.37E 02	4.64E-03	1.20E 12	7.00E 11
	8.69E 09	1.19E 02	6.75E 06	1.48E 07	3.08E 09			6.10E 03	8.87E 04	6.57E 00	2.39E 02
	6.20F 08	3.94E 07	5.91E-04	9.09E-01	3.12E-02			6.07E 04	9.24E-08	2.73E 03	2.60E-02
	6.86F 16	1.88E 16	1.93E 09	1.24E 09	3.04E 08			1.31E 03	1.17E-02	5.17E 11	2.97E 11
	1.76E 10	2.81E 04	1.72E 07	1.20E 07	5.23E 08			3.07E 03	4.23E-06	6.94E 00	2.53E 02
	4.69E 08	1.94E 07	1.39E-03	4.61E-01	8.14E-02			5.81E-06	7.35E-08	6.84E 02	2.10E-02
	3.61E 16	9.22E 15	3.11E 09	8.36F 00	3.44E 07			2.70E 03	2.94E-02	2.05E 11	1.27E 11
	2.67E 10	9.97E 04	1.09E 07	9.07E 04	8.29E 07			1.60E 03	2.10E-04	7.39E 00	2.64E 02
	2.42E 08	9.89E 05	3.03E-03	2.21E-01	1.94E-01			5.25E-04	6.59E-08	1.73E 02	1.64E-02
	1.78E 16	4.83E 15	7.24E 09	5.08E 08	3.24E 07			8.55E 03	7.39E 02	7.33E 10	5.54E 10
	1.30F 08	2.30E 10	3.55E-02	4.54E 04	1.14E 07			6.84E 02	1.10E 06	6.10E 00	6.72E 02
	9.81E 15	2.65E 15	1.52E 10	2.14E-01	2.53E 08			4.84E 04	6.29E-06	4.88E 01	2.74E-02
	2.13E 07	5.05E 03	2.19E 06	4.71E 08	3.45E 05			1.49E 04	1.66E-01	2.36E 10	2.52E 10
	5.39E 07	3.27E 06	2.95E-01	6.51E-02	1.22E 06			4.62E 02	6.05E-07	6.44E 00	2.66E 02
	5.39E 15	1.44E 13	2.55E 10	1.39E 08	1.79E 01			3.80E-06	6.17E-08	1.44E 01	4.36E-01
	3.64E 07	2.94E 05	5.28E 04	2.14E 06	8.89E 05			2.33E 02	4.60E-01	7.82E 09	1.00E 10
	3.64E 07	2.94E 06	7.84E-01	4.05E-02	5.99E 01			3.40E-06	6.10E-08	4.15E 00	1.57E 00
	2.90E 15	7.84E 14	3.23E 10	6.26E 07	5.75E 03			4.86E 04	1.79E-07	8.24E 09	4.44E 09
	9.94F 09	1.85E 06	3.69E 06	9.52E 05	3.18E 05			1.24E 02	1.70E 07	8.04E 00	2.40E 02
	1.84E 07	1.21E 14	6.39E 00	9.44E-01	4.49E 02			3.57E-04	6.04E 08	1.13E 00	3.28E 00
	1.52E 15	4.12E 14	3.39E 10	2.68E 07	1.84E 04			1.00E 05	2.94E 09	6.19E 08	1.1E 09
	6.03E 09	4.89E 05	2.84F 04	4.02E 06	1.64E 05			5.89E 01	9.39E-08	7.44E 08	2.22E 02
	9.04E 09	7.03E 05	2.84F 01	9.52E 00	1.64E 05			2.93E-06	6.04E-08	2.82E-01	5.09E 00
	7.59E 14	2.05E 14	4.85E 10	1.25E 07	9.80E 02			2.76E 04	7.46E 00	1.61E 08	3.18E 00
	3.16E 09	1.56E 06	1.10E 07	6.27E 04	4.08E 03			2.74E 01	4.67E-08	6.85E 00	2.04E 02
	4.13E 06	3.85E 05	6.74E 01	1.26E 01	4.08E 03			1.35E-06	6.03E-06	6.20E-02	6.69E 00

Table 1-2 (Continued)

ALT	M2 1/CC	O2 1/CC	Q 1/CC	NO 1/CC	NO2 1/CC	CO2 1/CC	U(1D) 1/CC	N(4S) 1/CC	N(2D) 1/CC	O3 1/CC	M20 1/CC
	C(211D) 1/CC	M 1/CC	OM 1/CC	MO2 1/CC	M20 1/CC	% 1/CC		PRESSURE DYN/CM2	DENSITY GRAMS/CC	DEN SC KM	TEMP DEG K
	VEP 1/5FC	VIM 1/5FC	VE1 1/5EC	O 1/1CC SEC	E 1/CC			ALPHAD CC/SEC	ALPHAI CC/SEC	A 1/SEC	D 1/SEC
80.00	3.52E 14	9.53E 13	7.47E 10	6.19E 06	6.96E 02	1.45E 11	1.16E 01	4.26E 05	1.88E 01	8.60E 07	4.71E 07
	2.19E 09	3.47E 07	6.32E 05	6.59E 04	3.84E 04			1.16E 01	2.17E-08	4.12E 00	1.64E 02
	1.75E 04	1.97E 05	9.74E 01	2.44E 01	4.86E 03	4.94E 03		1.04E-04	4.01E-08	1.20E-02	1.43E 01
85.00	1.48E 14	3.99E 13	1.21E 11	4.62E 04	1.25E 02	6.08E 10	4.67E 01	8.79E 05	4.74E 01	1.19E 08	5.61E 06
	3.23E 09	8.00E 07	6.95E 04	6.91E 04	1.61E 04			8.93E 00	9.10E-09	5.38E 00	1.77E 02
	6.98E 05	9.22E 04	1.12E 02	2.61E 01	5.64E 03	5.44E 03		8.21E-07	4.01E-08	2.51E-03	2.29E 01
90.00	5.73E 13	1.54E 13	1.91E 11	7.62E 06	1.67E 02	2.35E 10	6.31E 01	1.81E 06	1.19E 02	2.88E 07	9.18E 05
	1.26E 09	7.29E 07	6.30E 03	5.64E 03	6.28E 03			1.81E 00	3.53E-09	5.22E 00	1.70E 02
	2.73E 05	4.13E 04	1.79E 02	5.15E 01	9.27E 03	9.27E 03		5.99E-07	6.00E-08	6.49E-04	3.68E 01
95.00	2.18E 13	5.71E 12	3.74E 11	1.73E 07	3.15E 02	8.94E 09	2.19E 02	3.75E 06	3.01E 02	2.41E 06	2.40E 05
	2.96E 08	4.96E 07	5.40E 02	5.10E 02	2.45E 04			7.31E-01	1.34E-09	5.24E 00	1.88E 02
	1.10E 05	1.04E 04	7.64E 02	1.04E 03	4.55E 04	4.54E 04		5.19E-07	4.00E-08	5.60E-04	7.38E 01
100.00	8.89E 12	2.12E 12	4.70E 11	3.10E 07	4.90E 02	3.57E 09	7.79E 02	7.77E 04	7.61E 02	2.42E 05	7.17E 04
	5.60E 07	3.00E 07	6.70E 01	7.40E 01	9.59E 02			3.15E-01	5.36E-10	5.48E 00	2.01E 02
	4.64E 04	8.93E 03	1.26E 03	3.39E 03	8.19E 04	8.39E 04		4.82E-07	6.00E-08	6.20E-04	9.23E 01

Table 1-2 (Continued)

ALT	N ₁ 1/CC	O ₂ 1/CC	VIM 1/5FC	VFI 1/5SEC	F TEMP DEG K	O 1/CC	NO ₂ 1/CC	CO ₂ 1/CC	O ₁₁ D ₁ 1/CC	M(SI) PRESSURE DYN/CM ²	M(ZDI) DENSITY GRAMS/CC	AP DEN SC MT CM	ME TEMP DEG K
	VEP 1/5FC							F 1/CC	O ₂ 1/CC	M ₀ 1/CC	ALPHAD CC/SEC	BETA 1/SEC	
260.00	8.27E 08	7.46F 07	1.21E 09	5.91E 07	2.26F-01	6.98E 03	2.28E 03	4.80E 07	2.43E 06	1.17E 04	5.52E 06		
	4.28E 01	4.27E 00	3.55E 02	1.96F 03	5.69E 03	6.02E 05	4.44E 05	3.01E-04	7.47E-14	4.80E 01	1.30E 03		
280.00	5.08E 08	4.29E 07	9.06E 08	6.13E 07	7.02E-02	3.39E 03	1.99E 03	1.55E-04	2.01E 04	4.11E-08	4.85E-03		
	2.76E 01	2.98E 00	3.28E 02	2.04E 03	4.46F 03	7.17E 05	6.10E 05	2.70E-04	5.01E-14	2.19E 01	1.34E 03		
300.00	3.19F 08	2.53E 07	6.98E 08	6.35E 07	2.70E-02	1.80E 03	1.87E 03	1.84E 05	1.67E 06	3.87E-08	3.06E-03		
	1.81E 01	2.13E 00	4.52E 02	2.11E 03	3.35E 03	9.49E 05	7.68E 05	1.95E-04	3.45E-14	5.55E 01	4.72E 06		
320.00	2.03F 08	1.51E 07	5.29E 08	6.59F 07	9.34E-03	7.93E 02	1.43E 03	2.04E 07	1.30E 06	5.68E-08	1.96E-03		
	1.20F 01	1.55E 00	4.79E 02	2.17E 03	2.42E 03	9.49E 05	9.02E 05	1.43E-04	2.43E-14	5.80E 01	1.30E 03		
340.00	1.31E 08	9.19E 06	4.09F 08	6.83F 07	3.23F-03	4.09E 02	1.22E 03	4.52E 04	1.15E 04	8.70E 04	4.11E 04		
	8.03E 00	1.15E 00	4.86E 02	2.23F 03	1.65E 03	9.97E 05	9.64E 05	1.07E-04	1.75E-14	6.20E 01	1.40E 03		
360.00	8.48F 07	5.86E 06	3.19E 08	7.09F 07	1.11E-03	2.04E 02	1.04E 03	3.07E 04	9.52E 07	5.39E-08	8.29E-04		
	5.55E 00	8.60E-01	4.59E 02	2.27F 03	1.74E 03	9.49E 05	9.27E 05	8.93E-05	1.27E-14	4.49E 01	1.41E 03		
380.00	5.55E 07	3.45E 06	2.50E 08	7.35E 07	3.84E-04	1.09E 02	9.00E 02	2.88E 04	7.89E 05	5.20E-08	5.47E-04		
	3.71E 00	6.31E-01	3.88E 02	2.32E 03	6.29E 02	6.38F 05	8.24E 05	6.11E-05	9.42E-15	2.59E 04	3.61E 04		
400.00	3.68E 07	2.15F 06	1.96E 08	7.02E 07	1.33F-04	5.47E 01	7.61E 02	6.51E 06	6.54E 05	5.18E-08	1.42E 03		
	2.55F 00	4.97E-01	3.24E 02	2.36E 03	3.74E 02	7.13E 05	7.01E 05	4.69E-05	7.05E-15	7.03E 04	4.40E 04		
420.00	2.421 07	1.34E 06	1.55E 08	7.61E 07	4.60E-05	2.87E 01	6.59E 02	1.94E 04	5.43E 05	5.09E-08	1.42E 03		
	1.77E 00	3.82E-01	2.63F 02	2.40E 03	2.25F 02	5.89E 05	5.81E 05	4.80F 04	5.33E-15	7.85E 03	3.20E 04		
440.00	1.61E 07	8.41E 05	1.23E 08	8.20F 07	1.59F-05	1.51E 01	5.96E 02	3.82E-05	4.50E 05	7.28E 01	1.43E 03		
	1.23F 00	2.94E-01	2.10F 02	2.43F 03	1.36E 02	4.76E 05	4.71E 05	3.68E 06	4.07E-15	5.01E-08	1.62E-04		
460.00	1.07E 07	5.30E 05	9.721 07	8.50E 07	5.48F-06	8.03E 00	4.75E 02	2.82E-05	3.73E 05	7.51E 01	1.43E 03		
	8.681-01	2.30E-01	1.45E 02	2.47E 03	8.29E 01	3.77E 05	3.73E 05	5.79E 03	3.13E-15	4.93E-08	1.09E-04		
480.00	7.24F 04	3.36F 05	7.73F 07	8.62E 07	1.69E-06	4.28E 00	4.04E 02	2.21E-05	3.10E 05	7.72E 01	2.84E 06		
	6.14E-01	1.80E-01	1.261 02	2.50E 03	5.05F 01	2.91E 05	4.04E 02	2.08E 04	2.92E-15	4.87E-08	7.34E-05		
500.00	4.84F 06	2.13E 05	6.14E 07	9.15E 07	6.55E-07	2.30E 00	2.80E 02	1.74E 05	2.62E-15	7.92E 01	1.44E 03		
	4.38F-01	1.41E-01	4.99E 01	2.56E 03	3.05F 01	2.19E 05	2.16E 05	3.80E 03	2.37E 05	8.80E-08	4.97E-05		
520.00	3.28E 06	1.36F 05	4.91E 07	9.49F 07	2.26E-07	1.24E 00	2.97E 02	1.37E-05	1.89E-15	8.02E 02	2.53E 06		
	3.19E-01	1.12E-01	6.95E 01	2.56E 03	1.64E 01	1.60E 05	1.99E 05	2.64E 03	2.13E 05	4.57E 02	2.39E 05		
540.00	2.20E 06	8.09E 04	3.93E 07	9.64E 07	7.81E-08	6.68E-01	2.54E 02	2.04E 03	1.48E-15	8.29E 01	1.44E 03		
	2.29F-01	8.83E-02	4.92E 01	2.59E 03	1.11F 01	1.14E 05	1.54E 05	8.84E 05	1.77E 05	2.62E 02	2.29E-05		
560.00	1.44E 06	5.37F 04	3.14E 07	1.02E 08	2.70E-08	3.63E-01	2.17E 02	2.04E 03	1.17E-15	8.45E 01	1.44E 03		
	1.68E-01	7.01E-02	3.52E 01	2.61E 03	6.71E 00	8.33E 04	8.15E 04	6.88E 06	1.64E 05	1.50E 02	2.14E 04		
580.00	1.02E 06	3.95E 04	2.57E 07	1.04E 08	9.33F-09	1.99E-01	1.85E 02	1.75E 03	9.22E-16	8.81E 01	1.44E 03		
	1.24E-01	5.98E-02	2.51E 01	2.64E 03	4.09E 00	5.94E 04	5.81E 04	5.00E 05	1.21E 05	8.66E 01	2.02E 06		
								5.63E-06	7.32E-16	4.54E-08	7.35E-08		

Table 1-2 (Continued)

ALT	1/2 1/CC	O2 1/CC	V14 1/SEC	VE1 1/SEC	W0 1/CC	E TEMP DEG R	G 1/1CC SEC)	E 1/CC	CO2 1/CC	O11D) 1/CC	M14S) 1/CC	N12D) 1/CC	AP 1/CC	ME 1/CC
	VEH 1/SEC										PRESSURE DYN/CM2	DENSITY GRAMS/CC	DEN SC EM	TEMP DEG R
											M0 1/CC	DENSITY GRAMS/CC	ALPHAD CC/SEC	BETA 1/SEC
940.00	1.40E-03	1.94E-01	5.87E-05	2.04E-08	4.59E-17	6.38E-06	1.10E-01	1.10E-01	1.10E-01	2.94E-03	2.79E-07	4.10E-03	7.24E-03	7.89E-05
940.00	1.58E-03	1.25E-03	2.87E-01	3.04E-03	3.59E-03	5.74E-02	4.16E-02	4.16E-02	4.16E-02	1.59E-02	1.59E-02	2.09E-17	1.24E-02	1.44E-03
946.00	9.93E-02	1.31E-01	4.81E-03	2.11E-08	1.59E-17	3.70E-06	6.61E-00	6.61E-00	6.61E-00	2.21E-03	2.21E-03	3.47E-03	3.94E-08	1.21E-08
980.00	1.27E-03	1.03E-03	1.05E-01	3.95E-05	5.47E-18	2.15E-06	8.04E-02	8.04E-02	8.04E-02	2.44E-07	1.42E-02	1.79E-17	1.20E-02	1.44E-03
980.00	7.04E-02	8.82E-00	3.95E-05	2.19E-08	5.47E-18	2.15E-06	8.04E-02	8.04E-02	8.04E-02	1.42E-02	1.42E-02	2.87E-03	3.92E-08	8.60E-09
1000.00	1.64E-03	8.43E-04	1.94E-01	3.08E-03	2.07E-03	4.20E-02	2.93E-02	2.93E-02	2.93E-02	2.22E-07	1.64E-03	1.53E-17	2.71E-03	7.15E-05
1000.00	5.02E-02	5.97E-00	3.25E-05	2.27E-08	1.89E-18	1.24E-06	6.88E-00	6.88E-00	6.88E-00	1.25E-03	1.25E-03	2.34E-03	3.99E-08	1.44E-03
1040.00	8.52E-04	6.93E-04	1.60E-01	3.10E-03	1.59E-03	3.61E-02	2.47E-02	2.47E-02	2.47E-02	2.01E-07	1.64E-03	1.32E-17	1.39E-02	1.44E-03
1040.00	2.53E-02	2.74E-00	2.70E-05	2.45E-08	2.26E-19	4.32E-07	5.02E-00	5.02E-00	5.02E-00	1.14E-02	1.14E-02	1.64E-03	3.87E-08	4.40E-09
1080.00	5.75E-04	4.70E-04	1.04E-01	3.14E-03	9.51E-04	2.79E-02	1.78E-02	1.78E-02	1.78E-02	1.67E-07	9.22E-01	1.64E-03	1.50E-02	1.44E-03
1080.00	1.29E-02	1.27E-00	1.50E-05	2.63E-08	2.69E-20	1.50E-07	3.67E-00	3.67E-00	3.67E-00	4.09E-02	4.09E-02	1.13E-03	3.82E-08	2.27E-09
1120.00	3.91E-04	3.20E-04	7.78E-02	3.18E-03	5.77E-04	2.04E-02	1.29E-02	1.29E-02	1.29E-02	1.42E-07	7.49E-01	7.72E-18	1.44E-02	1.44E-03
1120.00	6.44E-01	5.95E-01	1.05E-05	2.83E-08	3.22E-21	5.27E-08	2.68E-00	2.68E-00	2.68E-00	2.26E-02	2.26E-02	1.13E-03	3.70E-08	1.18E-09
1160.00	2.47E-04	2.19E-04	5.95E-02	3.21E-03	3.53E-04	1.54E-02	9.32E-01	9.32E-01	9.32E-01	1.22E-07	6.13E-01	6.12E-18	1.81E-02	1.44E-03
1160.00	3.43E-01	2.80E-01	7.05E-04	3.04E-08	3.84E-22	1.67E-08	1.96E-00	1.96E-00	1.96E-00	1.28E-02	1.28E-02	5.33E-02	3.63E-05	4.84E-05
1200.00	1.83E-04	1.50E-04	4.41E-02	3.25E-03	2.18E-04	1.17E-02	6.73E-01	6.73E-01	6.73E-01	1.07E-07	5.02E-01	4.94E-18	2.09E-02	1.44E-03
1200.00	1.79E-01	1.33E-01	4.06E-04	3.27E-08	4.58E-23	6.73E-09	1.43E-00	1.43E-00	1.43E-00	7.02E-01	7.02E-01	3.67E-02	3.70E-08	3.24E-10
1200.00	1.27E-04	1.03E-04	3.33E-02	3.28E-03	1.35E-04	8.94E-01	4.82E-01	4.82E-01	4.82E-01	9.40E-08	9.40E-08	4.10E-18	2.22E-02	1.44E-03
										4.12E-01	4.12E-01	4.10E-18	3.64E-08	1.72E-10

Table 1-3 (Continued)

ALT	M2 1/CC	O2 1/CC	O 1/CC	NO 1/CC	MO2 1/CC	MO2 1/CC	CO2 1/CC	O1(D) 1/CC	N1(S) 1/CC	N2(D) 1/CC	O3 1/CC	M2O 1/CC	PRESSURE		DENSITY		TEMP	
													DYN/CM2	ALPHA2	GRAMS/CC	ALPHA1	DEN SC	HT
	C21(D) 1/CC	M 1/CC	OH 1/CC	MO2 1/CC	N2O 1/CC	E 1/CC	% 1/CC		ALPHA2 CC/SEC	ALPHA1 CC/SEC	A 1/SEC							
80.00	3.52F 14	9.51E 13	2.43E 10	1.97F 06	3.59E 04	1.44E 11	1.00E 00	1.00E 00	3.33E 05	5.02E-05	9.01E 07	4.70E 07						
	1.12E 05	4.25E 07	1.44E 06	6.59F 06	3.83E 04	1.44E 11	1.00E 00	1.00E 00	1.14E 01	2.17E-08	6.13E 00	1.07E 02						
	1.75E 04	1.94E 05	2.40E 01	2.87E 00	1.44E 03	1.47E 03	1.00E 00	1.00E 00	1.34E-04	6.01E-08	1.20E-02	5.74E-01						
85.00	5.71E 07	3.98E 13	6.79E 10	4.28F 04	1.22E 04	6.09E 10	1.00E 00	1.00E 00	4.81E 05	1.44E-04	5.02E 08	5.90E 04						
	6.99E 05	9.21E 04	1.62E 01	6.91E 04	1.61E 04	1.86E 03	1.00E 00	1.00E 00	4.83E 00	9.09E-09	5.39E 00	1.77E 02						
90.00	5.73E 13	1.54E 13	1.50E 11	7.92F 06	6.40E 03	2.35E 10	1.00E 00	1.00E 00	1.01E-06	6.01E-08	4.07E-03	8.61E-01						
	1.88E 08	7.28E 07	1.70E 04	5.64F 03	6.28F 03	2.31E 03	1.00E 00	1.00E 00	1.39E 06	3.63E-04	1.69E 08	9.18E 05						
95.00	2.73F 05	4.13E 04	4.69E 01	3.72F 00	2.31E 03	2.31E 03	1.00E 00	1.00E 00	6.94E-07	6.00F-08	5.22E 00	1.79E 02						
	2.18E 13	5.72E 12	3.75E 11	1.73E 07	3.40E 03	8.94E 09	1.00E 00	1.00E 00	2.84E 04	9.07E-04	2.47E 07	2.40E 05						
	1.19E 05	4.84E 07	1.73E 03	5.10E 02	2.40E 03	2.67E 03	1.00E 00	1.00E 00	7.33E-01	1.33E-09	5.25E 00	1.88E 02						
100.00	8.71E 12	2.12E 12	4.71E 11	2.98F 07	1.82E 03	3.57E 09	1.00E 00	1.00E 00	5.99E-07	6.00E-08	6.41E-04	7.28E-01						
	5.40E 07	3.00E 07	2.20E 02	7.40E 01	9.55F 02	3.57E 09	1.00E 00	1.00E 00	3.14E-01	5.37E-10	5.48E 00	2.01E 02						
	4.45E 04	8.95E 03	4.47E 01	4.59E 00	2.64F 03	2.84E 03	1.00E 00	1.00E 00	5.88E-07	6.00E-08	8.32E-04	1.44E 00						

Table 1-3 (Continued)

ALT	MZ 1/CC	OZ 1/CC	WIM 1/SEC	O 1/CC	MO 1/CC	MOZ 1/°C	C02 1/CC	O11D1 1/CC	M(4S1) 1/CC	M(2D1) 1/CC	AR 1/CC	ME 1/CC
	WEM 1/SEC	VIM 1/SEC	VEI 1/SEC	L TEMP DEG K	O 1/CC	SEC1 1/CC	E 1/CC	O*	PRESSURE DYN/CM2	DENSITY GRAMS/CC	DEN SC MT KW	TEMP DEG K
									M*		ALPHAD CC/SEC	BETA 1/SEC
600.00	4.44F 04	9.58E 02	4.95E 02	1.07F 04	3.22F-09	1.20E-03	1.00E 00	9.76E 03	9.31E-03	8.69E-01	1.50E 04	
	8.10E-03	9.86E-03	1.37F 02	1.04F 03	2.32F-02	9.02E 04	9.02E 04	8.96E-01	1.41E-16	6.91E 01	1.04E 03	
620.00	2.62E 04	5.25E 02	3.59E 02	6.98F 03	1.11E-09	5.23E-04	1.00E 00	6.75E 03	6.66F-03	1.15E-07	9.55E-08	
	5.88E-03	6.54F-03	1.16E 02	1.04E 03	1.44F-02	7.57E 04	7.57E 04	7.22E-07	1.06E-16	7.04E 01	1.04E 03	
640.00	1.55F 04	2.84F 02	2.68E 04	4.54E 03	3.89E-10	2.30E-04	1.00E 00	4.17E-01	4.76E-03	1.15E-07	5.54E-08	
	4.20F-03	4.84E-03	9.81E 01	1.04F 03	9.19F-03	6.34E 04	6.34E 04	5.72E-07	8.00F-17	7.23E 01	1.04E 03	
660.00	9.21F 03	1.59E 02	1.99E 02	2.95E 03	1.33E-10	1.01E-04	1.00E 00	3.04E-01	3.40E-03	1.15E-07	3.25E-08	
	3.11F-03	3.59E-03	4.28E 01	1.04F 03	6.01F-03	5.34E 04	5.34E 04	2.68E 03	6.09E-17	9.23E-02	1.20E 06	
680.00	5.49F 03	6.79E 01	1.47F 06	1.92E 03	4.59E-11	4.49E-05	1.00E 00	1.79E-01	2.43E-03	1.15E-07	1.90E-08	
	2.28F-03	2.67E-03	6.99E 01	1.04F 03	4.01F-03	4.58E 04	4.58E 04	3.73E-07	4.67E-17	7.64E 01	1.04E 03	
700.00	3.28E 03	4.80E 01	1.10E 04	1.25F 03	1.59F-11	7.00E-05	1.00E 00	1.13E 03	1.74E-03	2.11E-02	1.04E 06	
	1.68E-03	1.99E-03	5.99E 01	1.04E 03	2.71E-03	3.74E 04	3.74E 04	6.33E-02	1.75E-01	4.41E-02	1.12E 06	
720.00	1.96F 03	7.72E 01	1.17E 05	8.12E 02	5.48F-12	8.92E-06	1.00E 00	7.38E 02	1.24E-03	1.02E-02	9.63E 05	
	1.24E-03	1.48E-03	4.98E 01	1.04E 03	1.89E-03	3.15E 04	3.15E 04	2.57E-07	2.82E-17	8.23E 01	1.04E 03	
740.00	1.10E 03	1.52E 01	6.11F 05	5.28E 02	1.89E-12	4.01E-06	1.00E 00	4.80E 02	8.87E-04	1.15E-07	3.92E-09	
	9.18E-04	1.11E-03	4.20E 01	1.04E 03	1.28E-03	2.65E 04	2.65E 04	2.17E-07	2.22E-17	8.60E 01	1.04E 05	
760.00	7.11E 02	6.52E 00	4.58E 05	3.43E 02	6.54E-13	1.81E-06	1.00E 00	3.12E 02	6.34E-04	1.17E-07	2.33E-09	
	6.89E-04	6.29E-04	3.55E 01	1.04F 03	8.86E-04	2.22E 04	2.22E 04	1.66E-07	1.77E-17	9.03E 01	1.04E 03	
780.00	4.29E 02	4.79E 00	3.43F 05	2.23E 02	2.26E-13	8.19E-07	1.00E 00	2.03E 02	4.53E-04	1.17E-03	7.75E 05	
	5.10E-04	6.22E-04	2.99E 01	1.04E 03	6.17E-04	1.66E 04	1.66E 04	1.61E-07	4.53E-04	9.54E 01	1.04E 03	
800.00	2.60E 02	2.70E 00	2.59E 05	1.45E 02	7.81E-14	3.73E-07	1.00E 00	1.32E 02	3.24E-04	1.15E-07	8.35E-10	
	3.81E-04	4.67E-04	2.53E 01	1.04E 03	4.31E-04	1.54E 04	1.54E 04	1.41E-07	1.17E-17	1.01E 02	1.04E 03	
820.00	1.59E 02	1.53E 00	1.94E 05	9.44E 01	2.70F-14	1.71E-07	1.00E 00	8.58E 01	2.32E-04	2.60E-04	6.72E 05	
	2.84F-04	3.51E-04	2.13E 01	1.04F 03	3.02E-04	1.31E 04	1.31E 04	3.27E-03	9.62E-18	1.08E 02	1.04E 05	
840.00	9.63E 01	8.69E-01	1.46E 05	6.14F 01	9.32F-15	7.83E-08	1.00E 00	5.58E 01	1.66E-04	1.15E-07	3.63E-10	
	2.15E-04	2.65E-04	1.10E 05	3.99E 01	3.22E-15	3.61E-08	1.00E 00	1.11E-07	8.05E-18	1.16E 02	1.04E 03	
860.00	5.89F 01	4.65E-01	1.10E 05	3.99E 01	2.12F-04	1.10E 04	1.00E 00	3.63E 03	1.18E-04	1.19E-07	8.83E-10	
	1.62E-04	2.06E-04	1.52E 01	1.04E 03	1.48E-04	9.23E 03	9.23E 03	1.00E-07	6.81E-18	1.24E 02	1.04E 03	
880.00	3.61E 01	2.83E-01	8.14E 04	2.59F 01	1.11E-15	1.67E-08	1.00E 00	2.34E 01	8.44E-05	3.40E-05	5.44E 05	
	1.22E-04	1.51E-04	1.28E 01	1.04E 03	1.04E-04	7.74E 03	7.74E 03	7.92E-04	5.83E-18	1.34E 02	1.04E 03	
900.00	2.22E 01	1.62E-01	6.31E 04	1.65E 01	3.84E-16	7.78E-09	1.00E 00	1.53E 01	6.04E-05	1.70E-07	6.77E-11	
	9.23E-05	1.14E-04	1.08E 01	1.04E 03	7.33E-05	6.50E 03	6.50E 03	5.11E-04	5.05E-18	1.44E 02	1.04E 03	
920.00	1.34E 01	9.32E-02	4.79E 04	1.10E 01	1.33E-16	3.63E-09	1.00E 00	9.97E 00	4.32E-05	1.15E-07	4.74E 05	
	6.99E-05	6.64E-05	9.13E 00	1.04E 03	5.16E-05	5.45E 03	5.45E 03	2.69E-04	4.42E-18	1.55E 02	1.04E 03	
												2.53E-11

Table 1-3 (Continued)

ALT	M2 1/CC	O2 1/CC	VIM 1/SEC	VEI 1/SEC	NO 1/CC	MOZ 1/CC	CO2 1/CC	O11D1 1/CC	M14S1 1/CC	M12D1 1/CC	AR 1/CC	ME 1/CC
	VEH 1/SEC		VIM 1/SEC	VEI 1/SEC	E TEMP DEG K	Q 1/CC SEC1	E 1/CC	Q- 1/CC	M+ 1/CC	DENSITY GRAMS/CC	DEN SC MT KM	TEMP DEG K
											ALPHAD CC/SEC	BETA 1/SEC
940.00	8.43E-00	5.37E-02	3.63E-04	7.13E-00	4.59E-17	1.70E-09	1.00E-00	1.00E-00	6.48E-00	3.09E-05	4.28E-04	4.42E-05
	5.30E-05	6.50E-05	7.70E-00	1.04E-03	3.63E-05	4.58E-03	4.58E-03	4.58E-03	6.89E-08	3.90E-18	1.67E-02	1.04E-03
960.00	5.22E-00	3.11E-02	2.76E-04	4.64E-00	1.58E-17	8.02E-10	1.00E-00	1.00E-00	2.16E-04	2.21E-05	1.15E-07	1.54E-11
	4.03E-05	5.00E-05	6.50E-00	1.04E-03	2.55E-05	3.84E-03	3.84E-03	3.84E-03	4.35E-08	3.68E-18	2.16E-04	4.13E-05
980.00	3.24E-00	1.60E-02	2.10E-04	3.02E-00	5.67E-18	3.79E-10	1.00E-00	1.00E-00	1.50E-04	1.58E-05	1.15E-07	1.04E-03
	3.07E-05	3.81E-05	5.48E-00	1.04E-03	1.80E-05	3.22E-03	3.22E-03	3.22E-03	2.74E-04	3.12E-18	1.92E-02	3.69E-05
1000.00	2.02E-00	1.05E-02	1.61E-04	1.96E-00	1.89E-18	1.80E-10	1.00E-00	1.00E-00	5.86E-08	1.13E-05	1.15E-07	1.04E-03
	2.34E-05	2.91E-05	4.63E-00	1.04E-03	1.26E-05	2.70E-03	2.70E-03	2.70E-03	1.78E-00	2.82E-18	2.04E-02	3.60E-05
1040.00	7.87E-01	3.58E-03	9.38E-03	8.29E-01	2.28E-18	4.11E-11	1.00E-00	1.00E-00	5.42E-08	1.13E-05	1.15E-07	1.04E-03
	1.37E-05	1.77E-05	3.29E-00	1.04E-03	6.27E-06	1.90E-03	1.90E-03	1.90E-03	4.41E-05	5.76E-04	1.64E-07	3.68E-12
1080.00	3.10E-01	1.24E-03	5.51E-03	3.51E-01	2.69E-20	9.51E-12	1.00E-00	1.00E-00	7.54E-01	2.34E-18	2.27E-02	1.04E-03
	8.03E-06	9.98E-06	2.34E-00	1.04E-03	3.11E-06	1.34E-03	1.34E-03	1.34E-03	4.67E-08	2.94E-04	1.15E-07	1.43E-12
1120.00	1.24E-01	4.32E-04	3.28E-03	1.48E-01	3.22E-21	2.24E-12	1.00E-00	1.00E-00	4.17E-05	2.94E-04	3.87E-08	2.76E-05
	4.67E-02	5.90E-04	1.67E-00	1.04E-03	1.54E-06	5.34E-13	1.00E-00	1.00E-00	3.19E-01	1.98E-18	2.48E-02	1.04E-03
1160.00	4.67E-02	1.53E-04	1.94E-03	6.27E-02	3.84E-22	5.34E-13	1.00E-00	1.00E-00	4.05E-08	1.98E-18	2.48E-02	1.04E-03
	2.82E-04	3.51E-04	1.19E-00	1.04E-03	7.64E-07	4.55E-02	4.55E-02	4.55E-02	1.00E-05	1.50E-06	1.04E-08	2.42E-05
1200.00	2.07E-02	5.66E-05	1.16E-03	2.65E-02	4.58E-23	1.30E-13	1.00E-00	1.00E-00	3.53E-08	1.69E-18	2.65E-02	1.04E-03
	1.68E-04	2.10E-04	8.45E-01	1.04E-03	3.79E-07	4.88E-02	4.88E-02	4.88E-02	2.71E-08	1.27E-18	1.15E-07	1.04E-03
									4.16E-07			3.58E-14

REFERENCES

- 1-1. Hamlin, D.A. and M.R Schoonover, *The ROSCOE Manual, Volume 14a: Ambient Atmosphere (Major and Minor Neutral Species and Ionosphere)*, DNA 3964F-14a, Science Applications, Inc., 13 June 1975.
- 1-2. Myers, B.F., *The ROSCOE Manual, Volume 14b: Midlatitude Density Profile of Selected Atmospheric Species*, DNA 3964F-146, Science Applications, Inc., 13 June 1975.
- 1-3. Hamlin, D.A., et al, *ROSCOE Program Listings Obtained*, 1 March 1978.
- 1-4. Booker, H.G., "Fitting of Multi-region Ionospheric Profiles of Electron Density by a Single Analytic Function of Height," *J. Atmos. Terr. Phys.*, Vol. 39, pp 619-623, 1977.

SECTION 2

AMBIENT IONOSPHERE AND ION NEUTRAL COLLISION FREQUENCY MODELS

INTRODUCTION

Simple models of the daytime (noon) and nighttime (midnight) normal ionospheres are used in the WEPH code to indicate when nuclear burst produced ionization has fallen to normal (ambient) levels and to provide a reference for electromagnetic propagation effects. The models have generally been satisfactory for propagation frequencies above the HF band where propagation effects are dependent on the integral of ionization along the propagation path, but can result in significant errors at lower frequencies where the gradient of ionization is important (effects of striations and local inhomogeneities are neglected in this discussion).

Effective, D-region ionosphere models have recently been prepared that provide improved predictions for propagation in the VLF and LF bands (References 2-1 and 2-2). These models are used in conjunction with E- and F-region ionosphere models developed for use in HF propagation predictions (Reference 2-3) to prepare a new ambient ionosphere model for the WEPH code.

A simple model for the ion-neutral collision frequency has also been used in the WEPH code due to uncertainties in theoretical and experimental data. While there is still considerable uncertainty in specifying the ion-neutral collision frequency the model has been reformulated in terms of ion mobility. Mobility values are used which are consistent with recent measurements and which result in ion-neutral collision frequencies similar to those used at the Naval Ocean Systems Center (NOSC) to obtain agreement with ELF propagation data.

CURRENT WEPH MODELS

In the current WEPH code the ion-pair production rate for altitudes below 90 km is obtained from relations developed by Science Application Inc. (SAI) for ROSCOE (Reference 2-4). The electron and ion densities for ambient conditions are found from the ion-pair production rate and the D-region chemistry model. For altitudes above 90 km the electron density is obtained from relations given in Reference 2-4 and an effective ion-pair production rate derived using the E- and F-region chemistry model. Ambient models for the electron and nitrogen vibrational temperatures are also obtained from relations given in Reference 2-4. The ambient ionosphere model is independent of sunspot number, geographic location, season, and local time (other than day or night).

The ion-neutral collision frequency in the current WEPH code is calculated in terms of the average electron-neutral collision frequency

$$\bar{\nu}_{im} = \frac{\bar{\nu}_{em}}{20} .$$

For altitudes below about 100 km the electron neutral collision frequency can be expressed in terms of number density and temperature or pressure

$$\bar{\nu}_{im} = \frac{2 \times 10^{-10} nT}{20} = \frac{1.5 \times 10^5 p}{20} \quad h < 100 .$$

The average electron-neutral collision frequency is the high frequency average (for use when $\omega \gg \nu$) defined by Shkorofsky (Reference 2-5). The average ion-neutral collision frequency is the low frequency average (for use when $\omega \ll \nu$).

D-REGION IONOSPHERE MODELS

Theoretical Models

Theoretical models for the D-region can be developed by formulating ion-pair production rates and atmospheric chemistry models.

In general, both the production rate and chemistry models are dependent on solar conditions, geographic location, season, and local time. If an ambient electron density profile is known or assumed, it can be used in conjunction with an atmospheric chemistry model to derive an effective ion-pair production rate. This will insure that the desired ambient electron density is obtained when the ion-pair production rate is equal to the effective value. However, if the chemistry model is in error, then the effective ion-pair production rate will be in error and calculations of the transition from disturbed to ambient conditions can be distorted.

Figure 2-1 shows an example of daytime, D-region ionization rates. Below about 90 km galactic cosmic rays and Lyman α radiation dominate. Relations for these sources are given in the literature (see for example References 2-6, 2-7, and 2-8). For galactic cosmic rays the daytime and nighttime ion-pair production rate can be approximated from relations given in Reference 2-8 as

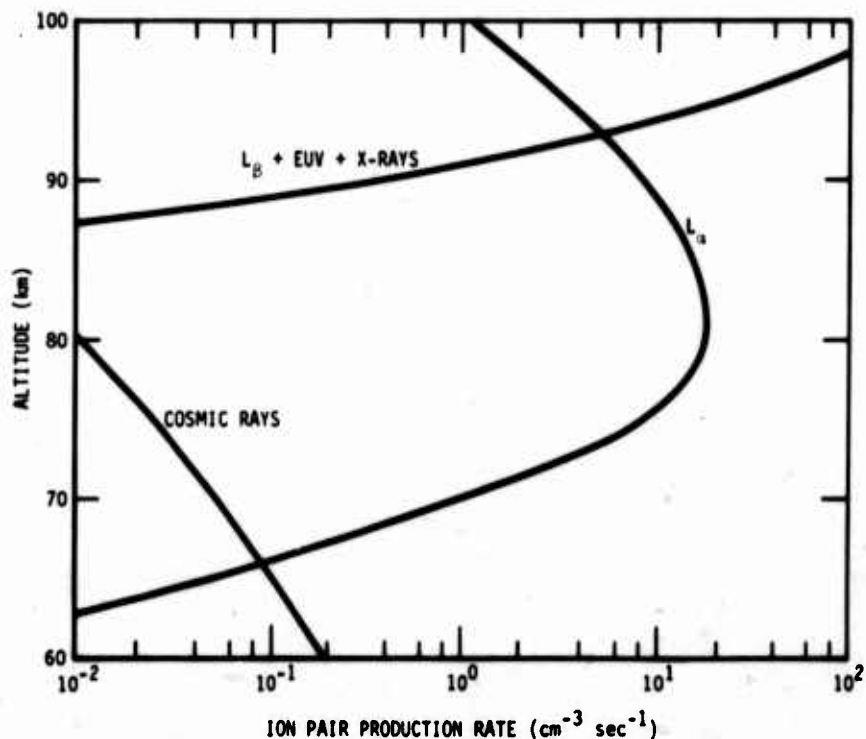


Figure 2-1. Daytime D-region ionization rates.

$$q_c = \bar{q} + R \cos x \quad (2-1)$$

where

$$x = \begin{cases} \frac{Y}{9} 2\pi & Y \leq 4.5 \\ \frac{Y}{13} 2\pi & 4.5 < Y \leq 11 \end{cases}$$

$$Y = \text{MOD}(y-9, 11)$$

y = number of the year in the 1900
(eg, 1974 becomes 74)

$$R = \frac{1}{2}(q_{c\max} - q_{c\min})$$

$$\bar{q} = \frac{1}{2}(q_{c\max} + q_{c\min})$$

$$q_{c\max} = \begin{cases} (0.056 + 0.7 \sin^4 \theta) ab & a \geq 1 \\ [(0.107 + 0.7 \sin^4 \theta)a - 0.8]b & a > 1 \end{cases}$$

$$q_{c\min} = \begin{cases} (0.056 + 0.48 \sin^4 \theta) ab & a \leq 1 \\ [(0.12 + 0.48 \sin^4 \theta)a - 1]b & a > 1 \end{cases}$$

$$a = 4 \times 10^{-17} n$$

$$b = \exp(-6 \times 10^{-6} p)$$

n = number density of neutral particles (cm^{-2})

p = atmospheric pressure (dynes cm^{-2})

θ = minimum (magnetic latitude, 60°) .

Note that the galactic cosmic source is maximum at sunspot minimum and minimum at sunspot maximum.

For Lyman α radiation the daytime ion-pair production rate is given in Reference 2-7 as

$$q_{L\alpha} = \begin{cases} \frac{(q_{L\alpha})_{\max}}{2} \left[1 + \frac{Y}{4} \right] & 0 \leq Y \leq 4 \\ (q_{L\alpha})_{\max} \left[1 - \frac{Y - 4}{14} \right] & 4 \leq Y \leq 11 \end{cases} \quad (2-2)$$

where

$$(q_{L\alpha})_{\max} = 6 \times 10^{-7} [\text{NO}] \exp(-0.047p \sec\chi)$$

χ = solar zenith angle

p = atmospheric pressure (dynes cm^{-2})

$[\text{NO}]$ = nitric oxide number density (cm^{-3}) .

At night scattered Lyman α radiation may be important, but the decay of daytime ionization probably dominates above about 70 km.

A relatively detailed D-region chemistry model is used in the WEPH code to determine electron and ion densities for a given ion-pair production rate. Electron and ion densities are dependent on the presence of minor neutral species (eg, O, $\text{O}_2(^1\Delta)$, NO, NO_2 , H_2O) as well as the major species. However, the model was developed for disturbed conditions and may not include sufficient detail to model the atmospheric response to low-level ionization sources. Further, the current minor neutral species model (obtained from Reference 2-4) does not include variations with solar activity, geographic location, season, or local time other than day or night.

Empirical Models for Low Frequency Propagation

Davis and Berry (Reference 2-1) have analyzed over 600 electron density profiles published in the literature and have derived an electron density model for use in predicting VLF and LF propagation. The model is based on the assumption that VLF and LF propagation

in the ambient ionosphere can be predicted with an exponential electron density profile of the form

$$N_e = N_w \exp[\alpha_w(h - h_w)] \quad (2-3)$$

where

$$N_w = 1.43 \times 10^7 \exp(-0.15h_w)$$

and h_w and α_w are parameters chosen to fit the electron density profiles in the altitude region where VLF and LF reflection occurs. This region is located near altitude h_o defined by

$$h_o = h_w - \frac{3.65}{\alpha_w + 0.15} \quad (2-4)$$

The expressions for h_w and α_w given in Reference 2-1 are

$$h_w = 71.81 - 7.84X_1 + 8.04X_2 - 1.23X_3 - 0.0371X_4 - 7.03X_5 \quad (2-5)$$

$$\alpha_w = 0.353 - 0.120X_1 - 0.072X_3 + 0.171X_5 \quad (2-6)$$

where

$X_1 = \cos \chi$, the solar zenith angle

$X_2 = \cos \theta$, the geographic latitude

$X_3 = \cos \phi$, a seasonal variable, $\phi = \frac{m - 0.5}{12}(2\pi)$

m = month number

X_4 = SSN, the Zurich smoothed, relative sunspot number for month of prediction

X_5 = absorption index, with values 0.0 for quiet conditions, 1.0 for disturbed conditions.

Table 2-1 shows predicted values for h_w and α_w given in Reference 2-1 for selected conditions.

Table 2-1. Predicted values of h_w and α_w from Equations 2-1 and 2-2 for selected conditions (quiet magnetic absorption index).

Month	Local Time	Latitude	Sunspot Number	Predicted h_w	Predicted α_w
6	12	10	10	72.86	.305
		40	100	69.51	.305
		70	10	71.27	.307
		10	100	67.92	.307
		40	10	70.07	.339
	00	10	100	66.73	.339
		40	10	86.92	.522
		70	100	83.57	.522
		10	10	82.20	.476
		40	100	78.86	.476
12	12	10	10	74.96	.415
		40	100	71.61	.415
		70	10	71.61	.183
		10	100	68.26	.183
		40	10	72.92	.230
	00	10	100	69.57	.230
		40	10	73.56	.291
		70	100	70.21	.291
		10	10	85.67	.401
		40	100	82.32	.401
70	70	10	100	83.85	.399
		40	100	80.50	.399
		70	10	78.44	.367
			100	75.09	.367

In deriving Equations 2-5 and 2-6 from the electron density data a propagation frequency of 30 kHz was used to define the reflection altitude h_o . Use of a lower or higher frequency would change h_o and thus the portion of the measured electron density profile modeled by Equation 2-3. While for typical electron density profiles the change in h_o would be only a few kilometers, the electron density gradient could change significantly. Only a few of the profiles used to derive Equations 2-5 and 2-6 were for nighttime conditions. Also, at night the reflection altitude is high and the electron density required to cause reflection is relatively low. Thus measured data near the reflection altitude can have considerable uncertainty. Finally, the variation of electron density during sunrise and sunset can be considerably more rapid than indicated in Equations 2-3, 2-5, and 2-6, particularly below about 70 km where changes in minor neutral species can affect deionization chemistry.

Morfitt (Reference 2-2) has derived effective exponential electron density profiles from analysis of VLF and LF field strength measurements. The field strength data include several radials outward from Hawaii, several transmission paths across the continental United States, and high latitude propagation over the Greenland Ice Cap. Table 2-2 shows effective values of h_w and α_w given in Reference 2-2 for daytime conditions. Also shown are the values of h_w and α_w predicted by Equations 2-5 and 2-6 for similar conditions. Table 2-3 shows similar data for nighttime conditions (nighttime data were only taken for the Pacific paths). The value of α_w has a relatively strong dependence on frequency suggesting that the actual slope of the electron density profile increases with altitude in the reflection region.

E- AND F-REGION IONOSPHERE MODELS

Theoretical Models

Theoretical models for the E- and F-regions can also be developed (see, for example, Reference 2-9), but the formulation is

Table 2-2. Effective values of h_w and α_w for daytime obtained from VLF and LF propagation measurements.

Propagation Path Location	Season	h_w	α_w	(Equations 2-3 and 2-4)	
				h_w	α_w
Midlatitude-Pacific	Summer	70	0.35	71.5	0.3
	Winter	74	0.15	72.4	0.22
Midlatitude-U.S.	Summer	72	0.15	71.3	0.31
	Winter	72	0.15	72.9	0.23
Greenland Ice Cap	Summer	72	0.15	69.5	0.33

Table 2-3. Effective values of h_w and α_w for nighttime obtained from VLF and LF propagation measurements, Midlatitude (Pacific), winter.

Frequency (kHz)	h_w	α_w	(Equations 2-3 and 2-4)	
			h_w	α_w
Below 10	87	0.15		
10-15	87	0.25		
15-25	87	0.35		
25-30	88	0.45		
30-40	88	0.55	81.3	0.35
40-60	88	0.65		

more complex and is dependent on phenomena such as diffusion which are difficult to model.

Empirical Models for HF Propagation

Stanford Research Institute (SRI) prepared E- and F-region electron density models for use in the NUCOM code that are based on Institute for Telecommunication Sciences (ITS) data obtained from vertical-incidence sounders (Reference 2-3).

At altitudes between 90 km and the peak of the F₂ region the electron density is specified by three profiles of the form

$$N_e(h) = N_{\max} \left[1 - \left(\frac{h_m - h}{y_m} \right)^2 \right] \quad h_m + y_m > h > h_m - y_m \quad (2-7)$$

where h_m is the height of the profile maximum, N_{\max} is the electron density at that maximum and y_m is the profile semithickness. Two of the profiles model the E-region and the F₂ region and values for N_{\max} , h_m , and y_m are obtained from ITS data for these regions. A third profile is used as a filler or connecting region and the values for N_{\max} , h_m and y_m are derived in terms of the parameters for the E- and F₂-regions. For altitudes above the peak of the F₂-region the electron density is computed from

$$N_e(h) = N_{\max} \exp \left\{ \frac{1}{2} \left[1 - \frac{h - h_m}{0.542 y_m} - \exp \left(- \frac{h - h_m}{0.542 h_m} \right) \right] \right\} \quad (2-8)$$

$$h > h_m$$

where N_{\max} , h_m , and y_m are the values for the F₂-region.

For the E-region the parameters are taken as

$$h_{\max} = 115 \text{ km}$$

$$y_m = 25 \text{ km}$$

$$N_{\max} = 1.24 \times 10^4 f_{OE}^2$$

where f_{OE} is the E-region critical frequency obtained from the ITS data. For the F_2 -region the parameters h_{max} , y_m , and N_{max} are all obtained from ITS data. The filler or connecting region (called the F_1 -region) is derived by requiring that it overlays with the F_2 -region by half the semithickness of the F_1 -region and by choosing the bottom of the F_1 -region as 130 km. The peak electron density of the F_1 -region is related to the peak density of the E-region by requiring that the F_1 -region critical frequency be twice the E-region critical frequency when the semithickness of the F_1 -region is 120 km. The formula used is

$$f_{OF1} = f_{OE} \alpha^n \quad (2-9)$$

where

$$n = \frac{y_m}{120}$$

and y_m is the F_1 -region semithickness.

Tables 2-4, 2-5, and 2-6 show values of f_{OE} , f_{OF2} , h_{mF2} , and y_{mF2} obtained from ITS data for selected conditions.

NEW IONOSPHERE MODEL

General

The new ionosphere model is similar to the current WEPH model in that effective ion-pair production rates are derived that produce specified electron density profiles when used with the WEPH code chemistry models. For the E- and F-regions electron density data obtained from the SRI model are used. For the daytime D-region the electron density profile obtained from Davis and Berry (Equation 2-3) is used to normalize cosmic ray and Lyman α production rates. This is done since only a limited altitude region is described by Equation 2-3. For the nighttime D-region the electron density obtained from Equation 2-3 is used to derive an exponential production rate for the upper D-region that can be combined with the cosmic production rate.

Table 2-4. E- and F-region data for March, 40 degrees longitude.

Parameter	Latitude	Sunspot Number			
		10		130	
		Local Time		Local Time	
		0	12	0	12
f_{OE} (MHz)	0	0.288	3.731	0.451	4.549
	30	0.177	3.688	0.318	4.386
	60	0.393	2.805	0.557	3.314
f_{OF2} (MHz)	0	6.776	8.729	11.584	12.756
	30	3.611	7.251	7.015	12.627
	60	2.355	4.756	4.874	8.33
h_{MF2} (km)	0	281	378	323	454
	30	328	283	375	353
	60	331	261	408	346
y_{mF2} (km)	0	77	189	107	201
	30	68	105	95	177
	60	69	81	110	137

Table 2-5. E- and F-region data for June, 40 degrees longitude.

Parameter	Latitude	Sunspot Number			
		10		130	
		Local Time		Local Time	
		0	12	0	12
f_{OE} (MHz)	0	0.222	3.586	0.295	4.458
	30	0.199	3.627	0.266	4.337
	60	0.768	3.071	1.106	3.653
f_{OF2} (MHz)	0	3.661	7.013	8.069	10.75
	30	4.538	6.517	8.412	9.66
	60	3.421	4.597	5.191	6.141
h_{MF2} (km)	0	292	398	351	469
	30	316	313	381	375
	60	490	314	368	394
y_{mF2} (km)	0	79	186	112	206
	30	69	127	103	188
	60	69	126	108	197

Table 2-6. E- and F-region data for December, 40 degrees longitude.

Parameter	Latitude	Sunspot Number			
		10		130	
		Local Time		Local Time	
		0	12	0	12
f_{OE} (MHz)	0	0.234	3.707	0.34	4.545
	30	0.401	3.205	0.656	3.9
	60	0.635	2.108	0.904	2.445
f_{OF2} (MHz)	0	5.535	8.53	10.269	12.591
	30	2.817	6.38	4.747	11.448
	60	2.066	4.843	4.351	10.552
h_{MF2} (km)	0	268	340	336	433
	30	307	239	340	311
	60	305	239	377	299
y_{mF2} (km)	0	73	159	107	195
	30	62	86	85	128
	60	62	65	100	97

As in the current model, only representative day (noon) and representative night (midnight) profiles are modeled. Diurnal modeling greatly increases the data storage requirements for the E- and F-regions and requires detailed energy deposition and chemistry modeling in the D-region where most of the variation occurs near sunrise and sunset.

E- and F-Region Model

Use of the parabolas described in Equation 2-7 results in discontinuities in electron density at $h_m + y_m$. While generally not significant for the intended application, it is desirable to prevent discontinuities and a profile fitting procedure described by Booker (Reference 2-10) is used to model the E- and F-regions.

In order to prevent discontinuities in the electron density or any of its derivatives, Booker suggests fitting the electron density profile with exponential fits between selected altitudes (transition altitudes) and then using smoothing functions at the transition altitudes which smooth the electron density over a prescribed scale length. The relation for electron density presented by Booker is

$$\log N_e(z) = \log N_0 + A_{01}(z - z_0) + \sum_{n=1}^m (A_{n,n+1} - A_{n-1,n}) + \left\{ f(z - z_n, B_n) - f(z_0 - z_n, B_n) \right\} \quad (2-10)$$

where

$z = h$ = altitude

z_n = transition altitudes used to describe electron density profile

$A_{n,n+1}$ = slope of $\log N_e(z)$ versus z for $z_n < z < z_{n+1}$

B_n = reciprocal of smoothing scale used at transition altitudes

$$f(z, B) = \begin{cases} B^{-1} \ln\{1 + \exp(Bz)\} & zB < 100 \\ z & zB \geq 100 \end{cases}$$

The above formulation is used in the WEPH code model by choosing scaling parameters from the E- and F-region parabola parameters given in Tables 2-4, 2-5, and 2-6. Figure 2-2 shows an example of the parabolas used to fit the daytime ionosphere. Transition altitudes used in determining parameters for the Booker formulation are shown in Figure 2-2 and are described in Table 2-7 along with the choice for the reciprocal of B. The electron density slope below z_1 is found by setting the electron density at $h_{mE} - y_E$ equal to $N_{mE}/1000$. The electron density slope above z_7 is found by computing the the electron density at $h_{mF2} + 2y_{F2}$ from Equation 2-8.

Table 2-7. Scaling parameters for use in Booker formulation.

Transition Altitude	Description	Smoothing Scale
z_1	$h_{mE} - 0.8 y_E$	0.5
z_2	h_{mE}	$0.1(y_E)$
z_3	$0.5(h_{mE} + y_E + h_{mF1} - y_{F1})$	$0.1(y_E + y_{F1})/2$
z_4	h_{mF1}	$0.1(y_{F1})$
z_5	$0.5(h_{mF1} + y_{F1} + h_{mF2} + y_{F2})$	$0.1(y_{F1} + y_{F2})/2$
z_6	h_{mF2}	$0.1(y_{F2})$
z_7	$h_{mF2} + y_{F2}$	$0.1(y_{F2})$

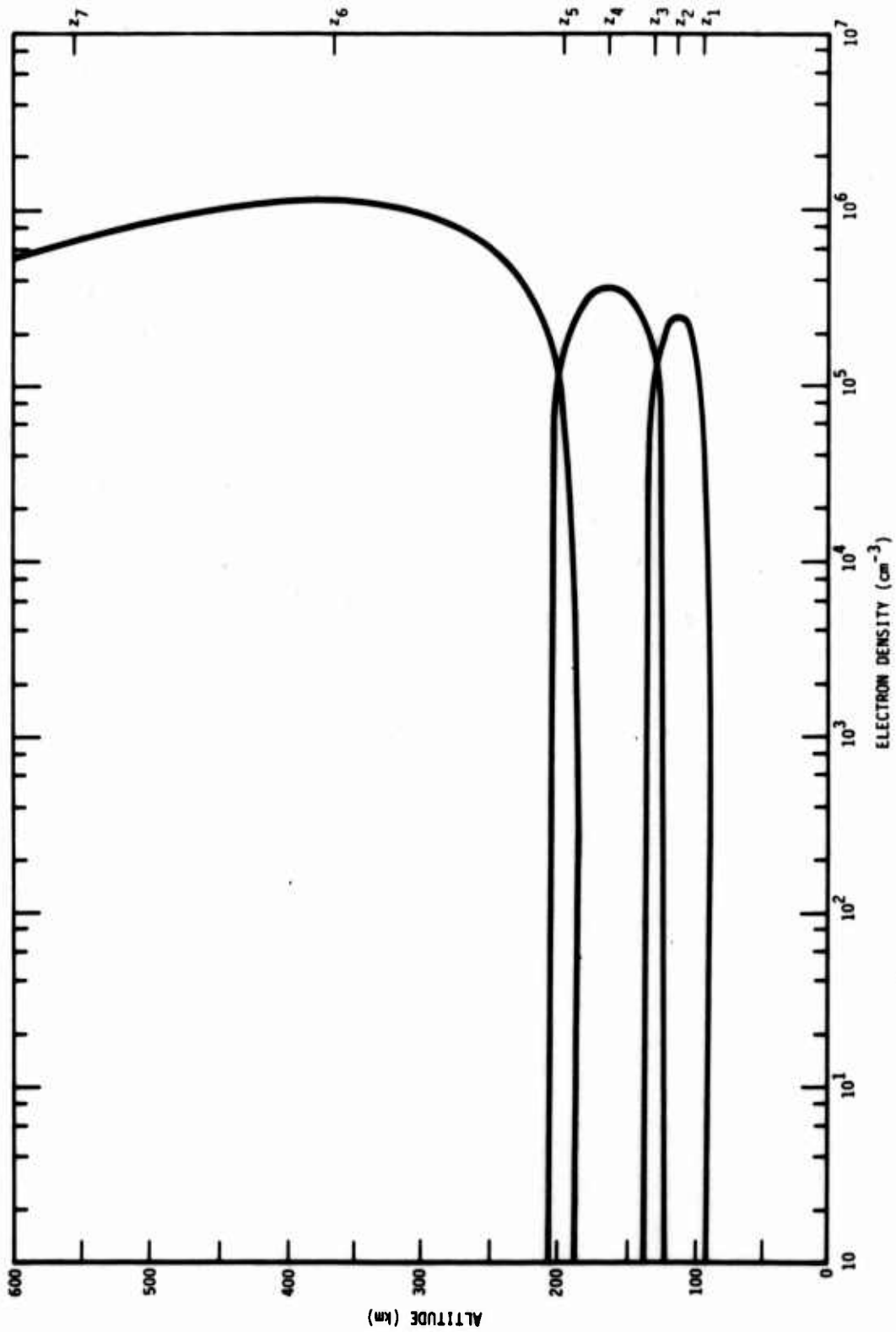


Figure 2-2. Parabolas for daytime ionosphere and selected transition altitudes for use in Booker formulation.

After the electron density at a specified altitude is found, the ion-pair production rate is determined from the chemistry model as in the current WEPH code ionosphere model.

D-Region Model

For the D-region model Equations 2-3 through 2-6 are used to define the electron density at altitude h_1 and h_2 where

$$h_1 = h_0 + \frac{1}{\alpha_w} \quad (2-11)$$

$$h_2 = h_0 - \frac{1}{\alpha_w} \quad (2-12)$$

Then the D-region chemistry model is used to determine the total effective ion-pair production rates (q_1 and q_2) required to produce the specified electron densities at h_1 and h_2 . In computing the sun-spot number the following relation obtained from Reference 2-3 is used

$$SSN = - 406.35 + \sqrt{93608 + 1117 \bar{F}}$$

where \bar{F} is the average 10.7 cm solar flux. The quantity \bar{F} is obtained from the SAI atmospheric model developed for ROSCOE in which \bar{F} is based on an assumed sinusoidal 11-year (4018 day) variation with a maximum value of 250 and a minimum value of 65.

The cosmic ray production rates at h_1 and h_2 are found from Equation 2-1, and ion-pair production rates that can be added to the cosmic ray production rates determined from

$$q_1 = q(h_1) - q_c(h_1) \quad (2-14)$$

$$q_2 = q(h_2) - q_c(h_2) \quad (2-15)$$

If the cosmic ray production rate is larger than the total q required at either h_1 or h_2 , the cosmic ray production rate is reduced to a value slightly less than the total production rate ($q_c = 0.9q$).

For daytime conditions an effective Lyman α production rate is defined in terms of q_1 and q_2 by

$$q_{L\alpha} = C[\text{NO}] \exp(-\beta p) \quad (2-16)$$

where

$$\beta = - \frac{\ln\left(\frac{q_1 [\text{NO}]_2}{q_2 [\text{NO}]_1}\right)}{p(h_1) - p(h_2)}$$

$$C = \frac{q_1}{[\text{NO}]_1 \exp[-\beta p(h_1)]}$$

$[\text{NO}]_1$ = nitric oxide density at h_1

$[\text{NO}]_2$ = nitric oxide density at h_2 .

The Lyman α and cosmic ray production rates are added to obtain the total production rate. The above procedure results in a value of β for a number of conditions smaller than the value derived for Lyman radiation in Reference 2-7. This results in underestimating the Lyman α ionization in the upper D-region. To prevent this the value of β is limited to be equal or greater than 0.05. Then to maintain the ionization gradient between h_1 and h_2 the cosmic ray production rate is modified so that

$$q_2 = q_{L\alpha}(h_2) + q_c(h_2) \quad (2-17)$$

For nighttime conditions an exponential ion-pair production rate is determined in terms of q_1 and q_2 from

$$q_E = C \exp[\beta(p)] \quad (2-18)$$

where

$$\beta = \frac{\ln\left(\frac{q_1}{q_2}\right)}{p(h_1) - p(h_2)}$$

$$C = \frac{q_1}{\exp[-\beta p(h_1)]}$$

The value of β is not allowed to become negative, which can happen when the chemistry and electron density models are not consistent.

Note that the above procedures result in an exponential variation in production rate rather than electron density near the altitude h_0 . However, the difference in the electron density profile near h_0 is small and the above procedure results in a better fit to the electron density below h_0 where atmospheric chemistry can affect the gradient.

Examples of Model Output

Figures 2-3 and 2-4 show comparisons of electron density obtained from the current and new ionosphere models for conditions similar to those for which the current model is applicable.

Figure 2-5 shows the D-region results from the new model in more detail. The quantity α is the reciprocal of the electron density scale height. Note that α is not constant but does equal α_w specified in Equation 2-6 near h_0 . For daytime conditions the electron density is nearly constant between h_w and the bottom of the E-region. The ion-pair production rate and electron density would increase above h_w if the NO concentration was increased (see Section 1). For nighttime conditions the altitude h_0 is below the altitude where there is significant change in the electron loss rate in the WEPH code chemistry model. This requires an increase in the ion-pair production rate with decreasing altitude and results in a negative value for β in Equation 2-18. Limiting the value of β to zero results in a slightly larger value of α near h_0 than α_w . The inconsistency between the electron density model and the chemistry model could be resolved if more detailed latitude, season, and solar cycle variations were included in the chemistry model. The limiting value of β also results in a nearly constant electron density between h_w and the bottom of the E-region

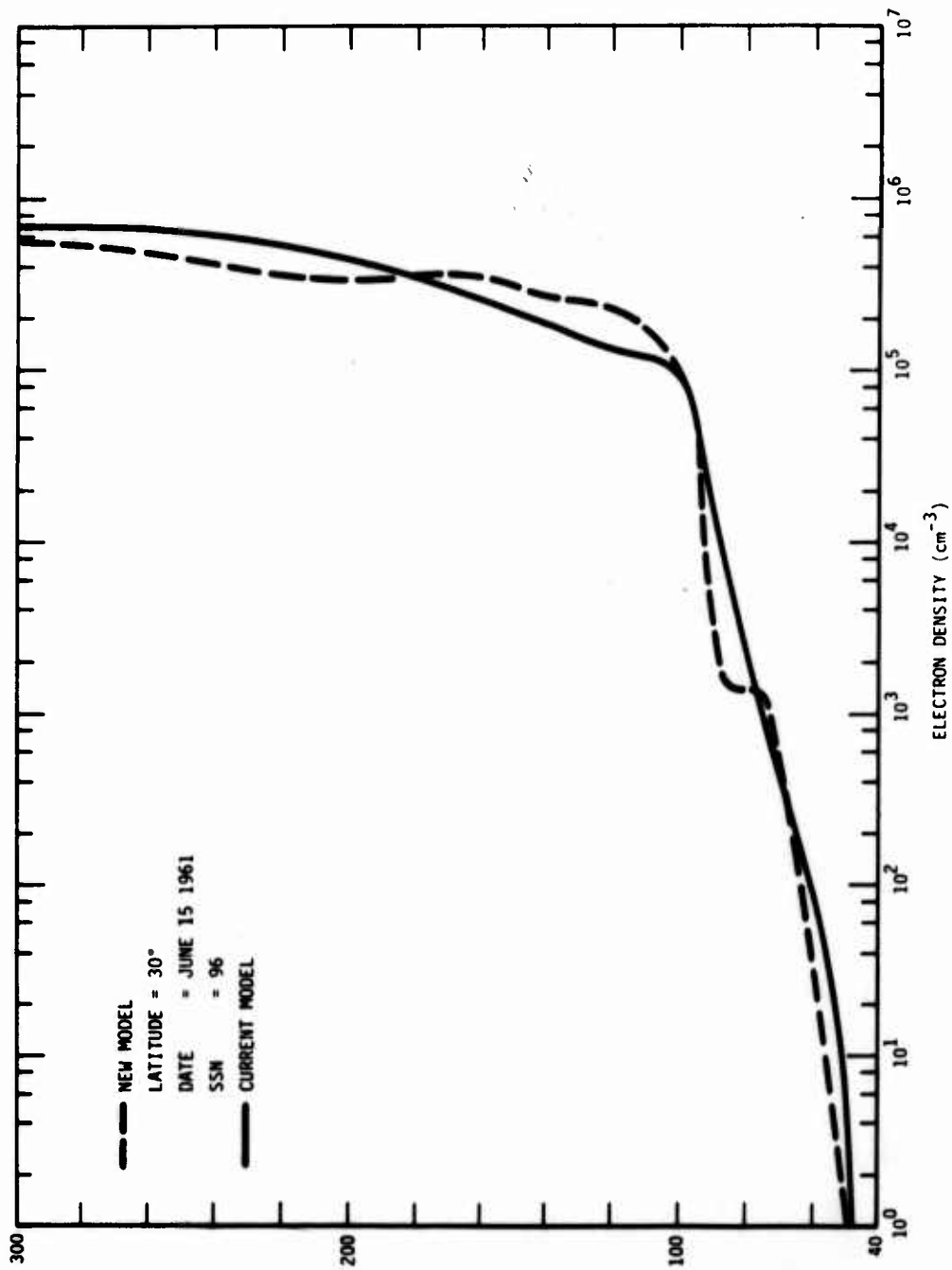


Figure 2-3. Comparison of current and new ionosphere models for daytime conditions.

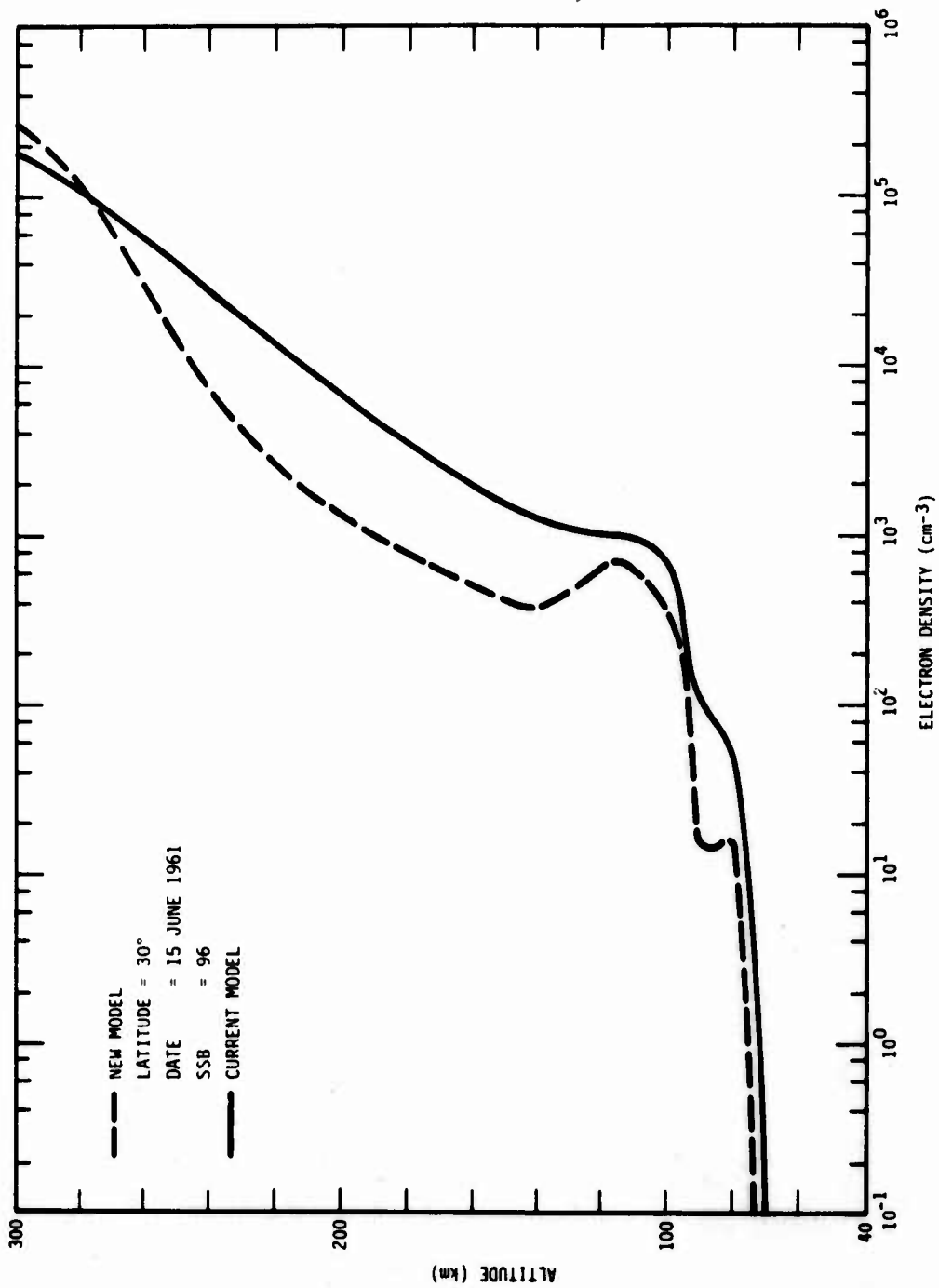


Figure 2-4. Comparison of current and new ionosphere models for nighttime conditions.

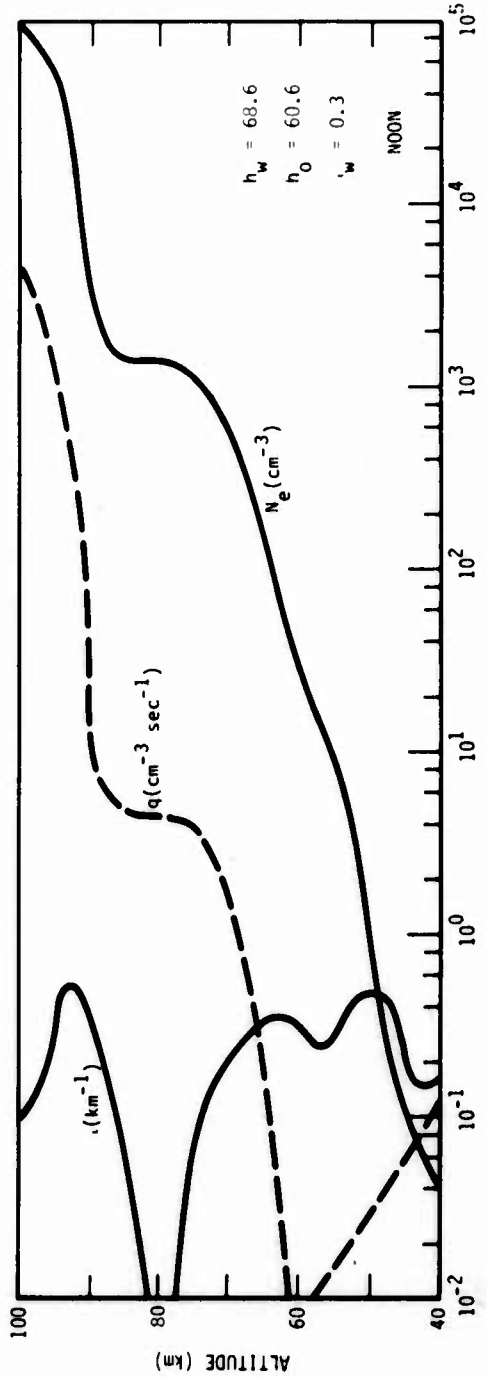
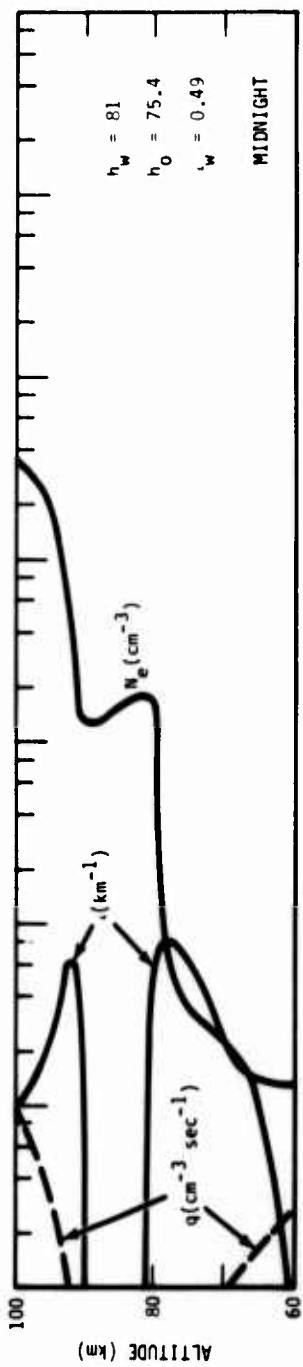


Figure 2-5. D-region ionization, 30 degrees latitude, 15 June 1961.

for nighttime conditions. Use of an exponential fit between h_w and the E-region might provide a better model.

The positive and negative ion densities predicted by the model also depend on the ion-pair production rate and the atmospheric chemistry model. The D-region chemistry model used in the WEPH code was developed for moderate to large production rates and may result in significant errors when used to predict ambient ion concentrations. Also, the lack of latitude, seasonal and solar cycle dependencies may result in incorrect variations in ion densities with these parameters.

Figures 2-6 and 2-7 show day and night profiles obtained with the new model for different conditions. The variation in the nighttime E-region electron density can be large with relatively low values occurring at midlatitudes during sunspot minimum (see Tables 2-4, 2-5, and 2-6).

New Ion-Neutral Collision Frequency Model

As previously mentioned, there is considerable uncertainty in ion-neutral collision frequency predictions and a simple formulation in terms of the electron-neutral collision frequency is currently used in the WEPH code. Recently, the U.S. Army Electronics Command initiated systematic measurements of atmospheric ion mobility (Reference 2-11), and it appears appropriate to model the ion-neutral collision frequency in terms of ion mobility.

The low frequency ion-neutral collision frequency is given in terms of ion mobility in Reference 2-12 as

$$\bar{\nu}_{im} = \frac{9.6 \times 10^{11} n}{M_i u_i} \text{ sec}^{-1} \quad (2-19)$$

where

$$n = \text{neutral particle density, cm}^{-3}$$

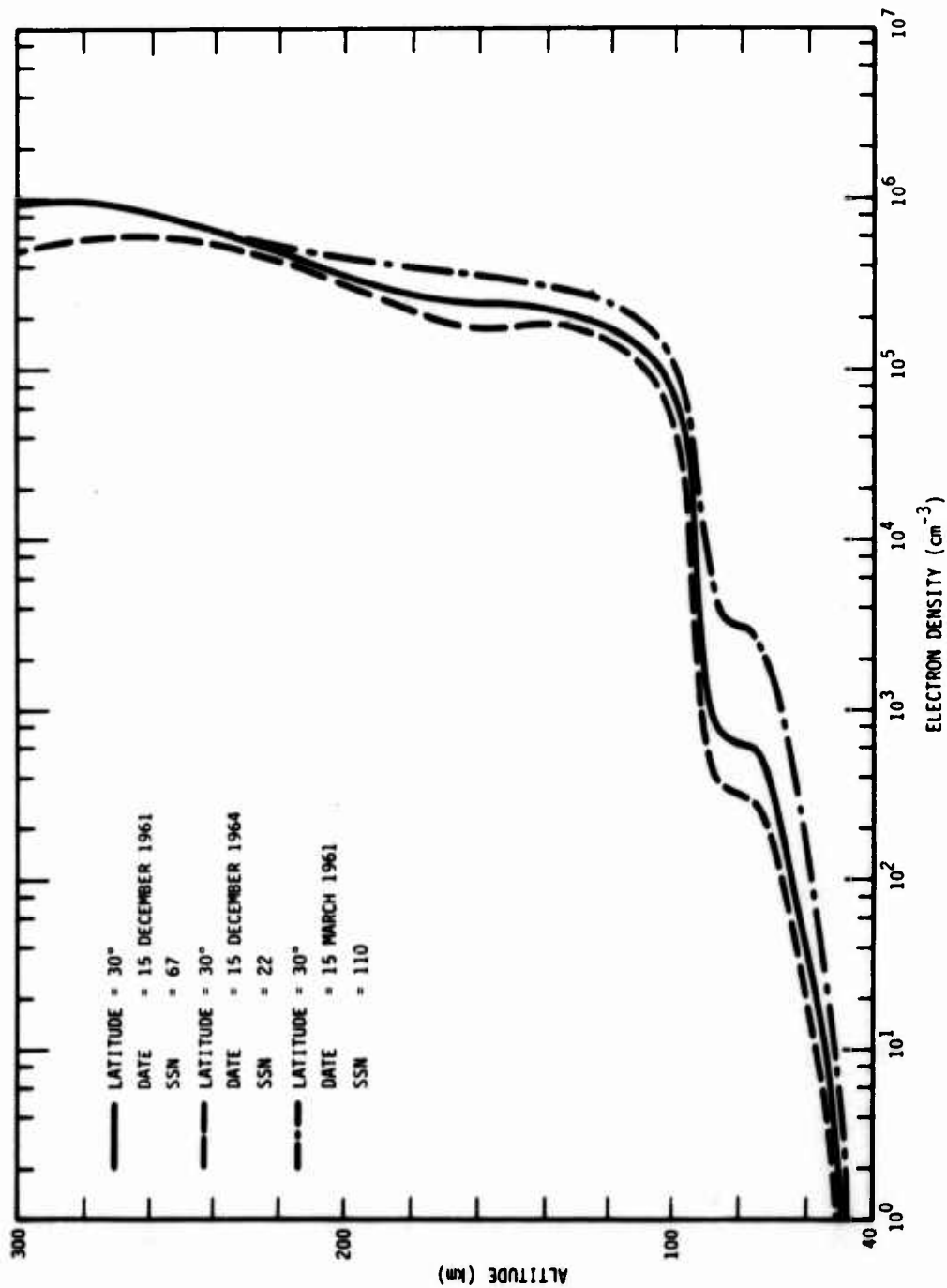


Figure 2-6. Comparisons of daytime profiles obtained with new ionosphere model.

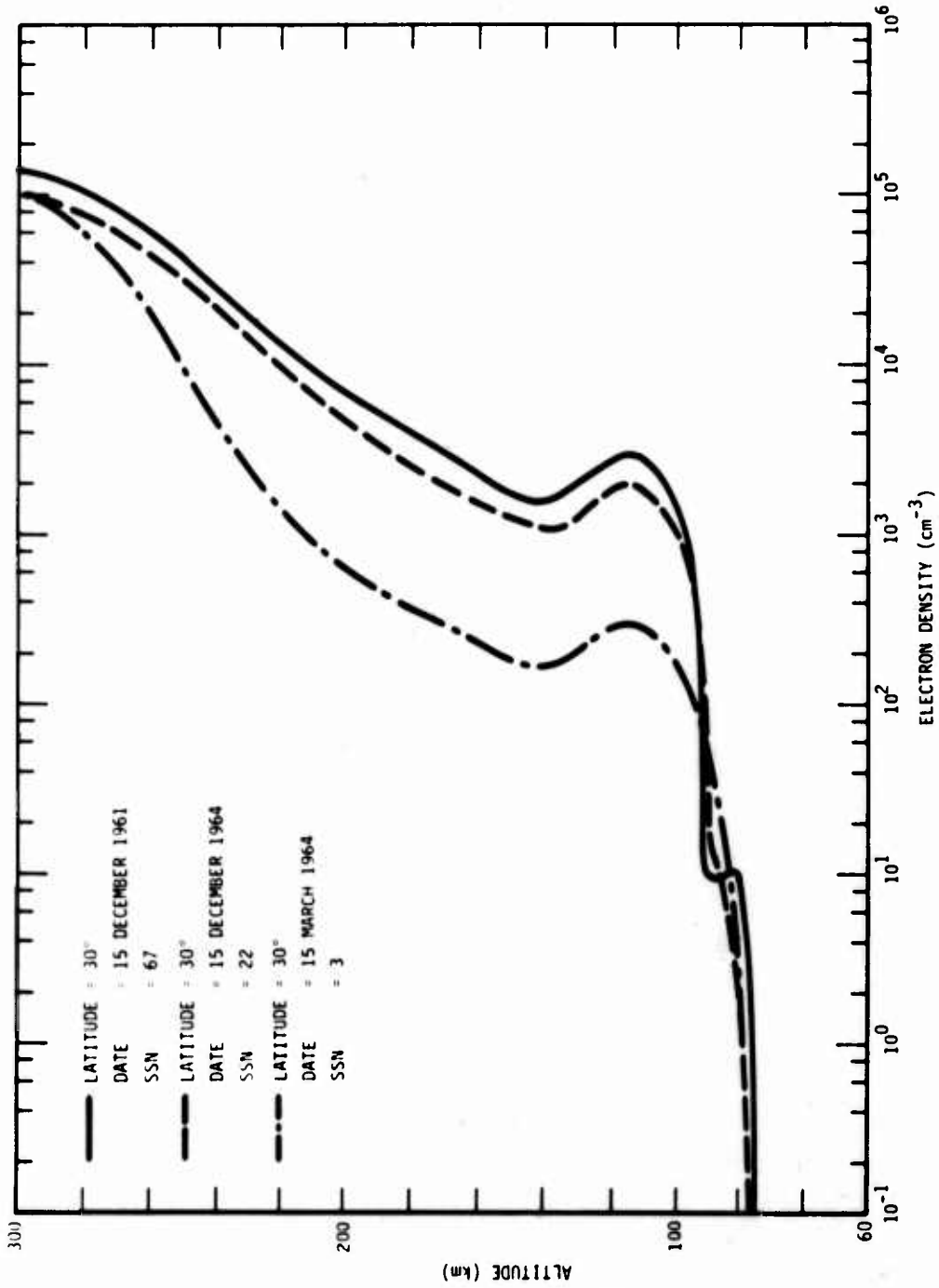


Figure 2-7. Comparisons of nighttime profiles obtained with new ionosphere model.

$$M_r = \text{reduced mass} = \frac{M_i M_n}{M_i + M_n}$$

M_i, M_n = ion and neutral particle mass respectively, AMU

u_i = ion mobility $V^{-1} cm^{-1} sec^{-1}$.

Note that the reduced mass only varies by a factor of two as the ion mass varies from M_n (≈ 30) to a value much larger than M_n . The thermal ion mobility is also given in terms of the reduced mass in Reference 2-12;

$$\mu_i \propto \frac{1}{\sqrt{M_r}} \quad (2-20)$$

Thus, the ion-neutral collision frequency may be relatively insensitive to ion mass.

For an assumed ion mass of 60 AMU and $\mu_i \propto 1/\sqrt{T}$, Equation 2-19 becomes

$$\bar{\nu}_{im} = \frac{2.8 \times 10^9 n T^{1/2}}{\mu_i} \quad sec^{-1} \quad (2-21)$$

Theoretical calculation for ion mobilities in air given in Reference 2-12 vary from about $9 \times 10^{19} V^{-1} cm^{-1} sec^{-1}$ for NO^+ to about $6 \times 10^{19} V^{-1} cm^{-1} sec^{-1}$ for a hydrated ion. Atmospheric measurement for positive and negative ion mobilities given in Reference 2-13 vary from about 8×10^{19} to $22 \times 10^{19} V^{-1} cm^{-1} sec^{-1}$ (some much smaller values believed to be associated with aerosol particles are also reported for altitudes above about 60 km). The above range in ion mobilities results in ion-neutral collision frequencies that vary from $\bar{\nu}_{em}/5$ to $\bar{\nu}_{em}/20$ where $\bar{\nu}_{em}$ is the high-frequency electron-neutral collision frequency ($\bar{\nu}_{im} = \bar{\nu}_{em}/20$ in the current WEPH code model).

In performing low frequency propagation calculations NOSC has adapted an ion-neutral collision frequency that varies exponentially from $10^{10} sec^{-1}$ at sea level to $8 \times 10^3 sec^{-1}$ at 100 km for nighttime

conditions and is about half these values for daytime conditions (Reference 2-14). These values correspond to $\bar{v}_{em}/20$ at sea level and $\bar{v}_{em}/5$ at 100 km. The smaller values of \bar{v}_{em}/v_{em} in the upper D-region appear to result in better agreement with ambient propagation data than the larger sea level values.

The following expression for ion mobility is used in Equation 2-21 for the new ion-neutral collision frequency model

$$\mu_i = \begin{cases} 20 \times 10^{19} & h \leq 50 \text{ km} \\ 20 \times 10^{19} \exp[-0.277(h-50)] & 50 \text{ km} \leq h \leq 100 \text{ km} \\ 5 \times 10^{19} & h \geq 1000 \text{ km} \end{cases} \quad (2-22)$$

These values for ion mobility are reasonably consistent with measurements reported in Reference 2-13 and result in ion-neutral collision frequencies similar to those used at NOSC in the upper D-region.

COMPARISONS WITH PROPAGATION DATA

ELF Propagation Data

In Reference 2-15, 78 Hz propagation measurements between Mt. Airy, North Carolina and Goose Bay, Labrador (midpoint $\approx 48^\circ\text{N}$ latitude, 290°E longitude) are presented that indicate that the attenuation rate varied from about 1 dB per megameter at night to about 1.4 dB per megameter during the day. Similar values were presented in Reference 2-16 for an eastwest path between Hawaii and Utah. Table 2-8 shows attenuation rates for these paths obtained with several ionosphere and collision frequency models.

The first group of calculations shown in Table 2-8 are for the north-south path. Figures 2-8 and 2-9 show the several electron density profiles used. The nighttime profile labeled WEDCOM is a modification of the WEPH profile that is similar to the profile used at NOSC (Reference 2-14). The profiles labeled New Model (preliminary) were obtained with a preliminary version of the new ionosphere model previously described. The profiles labeled New Model with NOSC

Table 2-8. ELF calculations.

North Carolina to Goose Bay, Labrador
(Midpoint $\approx 48^\circ$ N Lat., 290° E Long.)

<u>Ionosphere Model</u>	<u>Collision Frequency Model</u>	<u>Attenuation Rate (dB/1000 km)</u>	
		<u>Night</u>	<u>Day</u>
WEPH	WEDCOM	1.86	1.64
WEDCOM	WEDCOM	0.82	1.64
WEDCOM	New	1.0	1.73
New (15 Dec 66)	WEDCOM	1.2	1.22
New (15 Dec 66)	WEPH	1.46	1.25
New (15 Dec 66)	New	1.42	1.26
New (15 Dec 66) with NOSC parameters	New	0.78	1.1

Utah to Hawaii
(Midpoint $\approx 30^\circ$ N Lat., 220° E Long.)

New (15 March 71)	WEDCOM	1.26	-
New (15 March 61)	WEDCOM	1.19	-
New (15 March 64)	WEDCOM	3.2	-

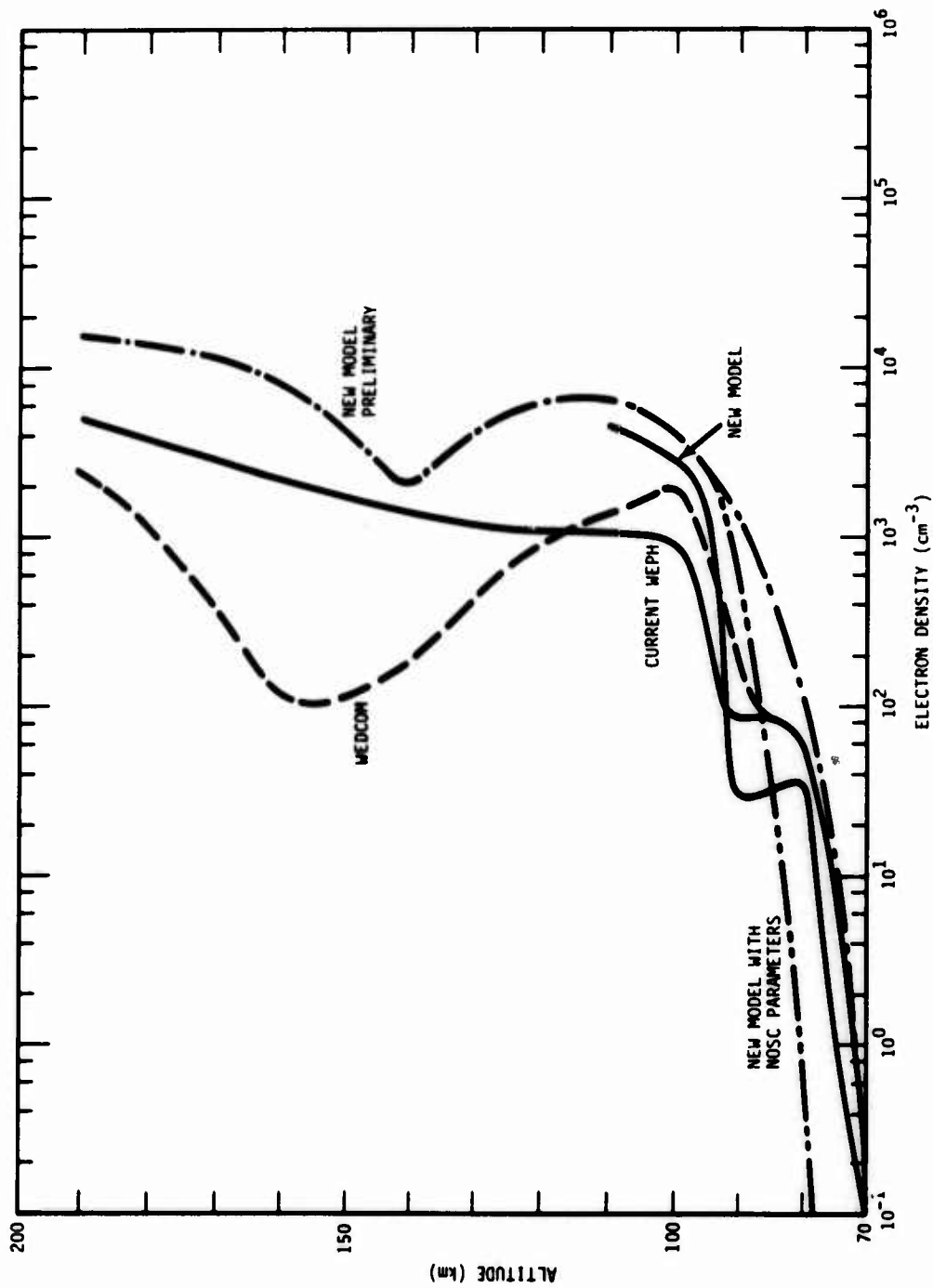


Figure 2-8. Electron density profiles used for nighttime ELF calculations.

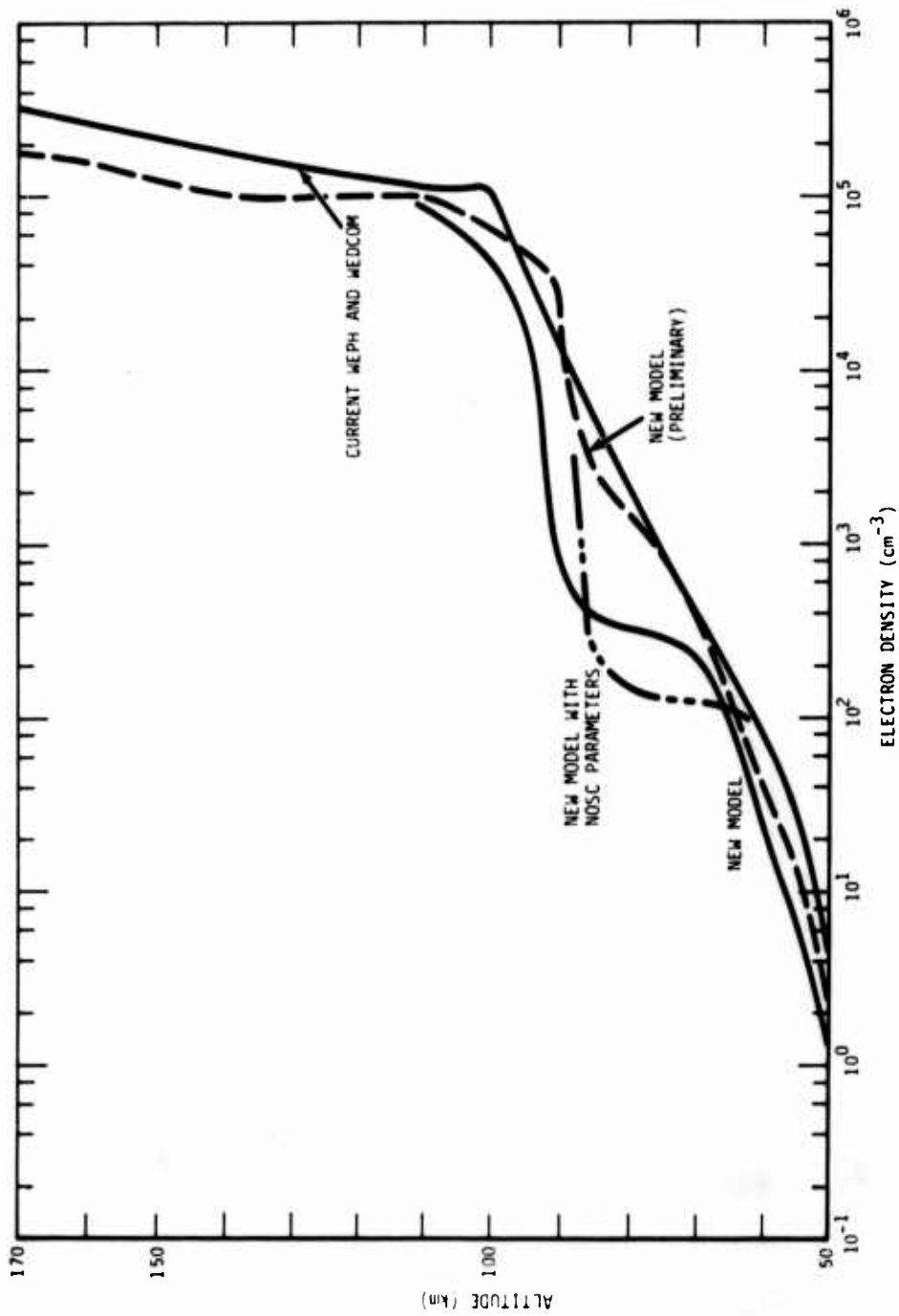


Figure 2-9. Electron density profiles used for daytime ELF calculations.

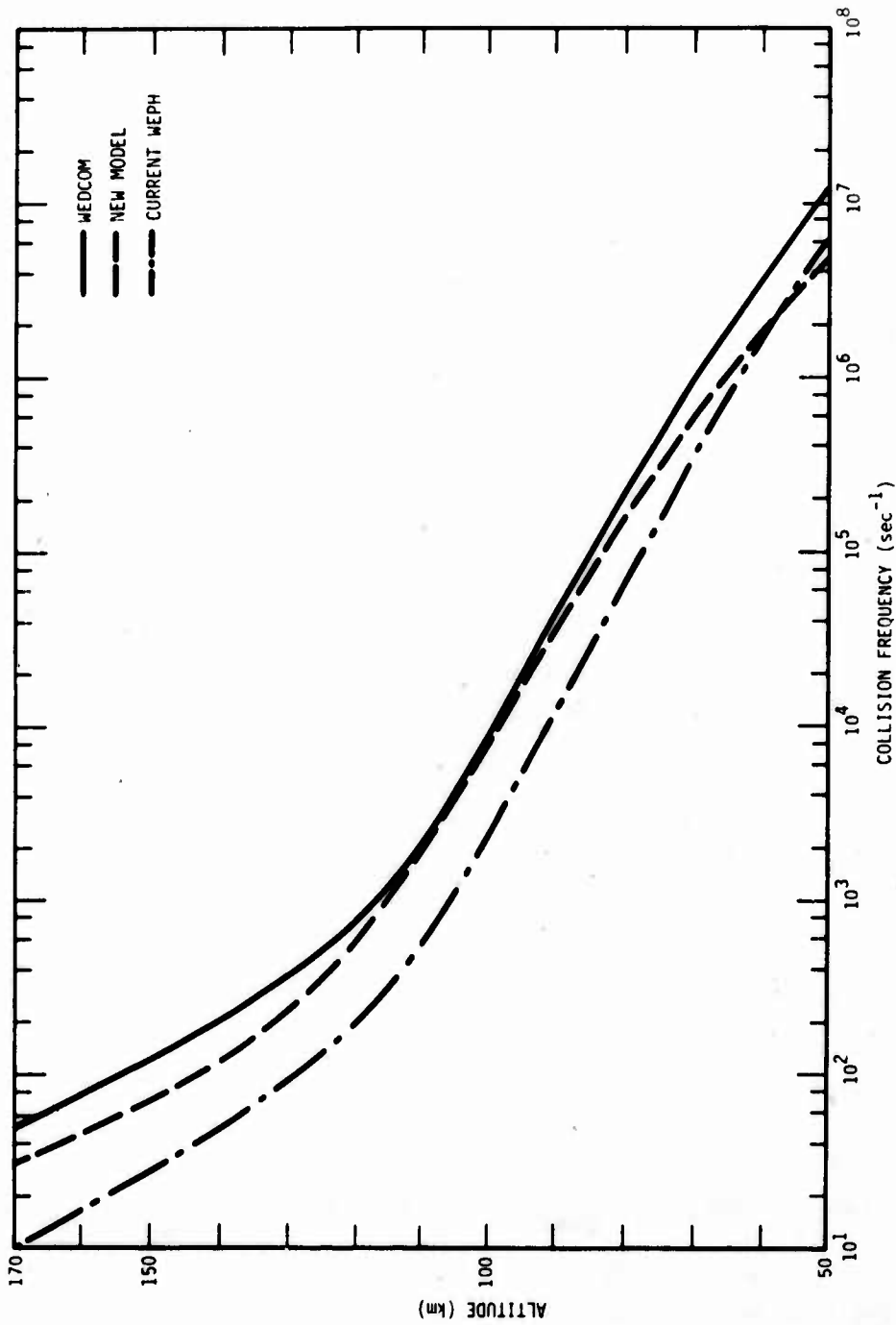


Figure 2-10. Ion-neutral collision frequency profiles used for ELF calculations.

parameters were obtained by using $h_w = 88$ km, $\alpha_w = 0.35$ for nighttime and $h_w = 72$ km, $\alpha_w = 0.15$ for daytime in the preliminary version of the new model. The profiles labeled New Model are for the final version of the new ionosphere model and are shown for reference. They were not used for low frequency calculations.

Figure 2-10 shows the ion-neutral collision frequency profiles used. The profile labeled WEDCOM is similar to the profile used at NOSC.

The daytime results are relatively insensitive to the ion-neutral collision frequency model, but are sensitive to the electron density profile. The results for the new ionosphere model and particularly for the new model with NOSC parameters are more consistent with the propagation data than the current WEPH and WEDCOM models. The difference appears to be due to the larger gradient in electron density between 80 and 100 km in the new model. The final version of the new model has a larger gradient than the preliminary version shown in Figure 2-9 and should result in somewhat lower attenuation rates.

For nighttime conditions, both the electron density and ion-neutral collision frequency profiles are important. The WEDCOM electron density profile results in attenuation rates consistent with measured values with either the WEDCOM or new ion-neutral collision frequency models. When the new ionosphere model with D-region parameters (h_w, α_w) chosen from Equations 2-5 and 2-6 is used, the attenuation rate is high even when the WEDCOM ion-neutral collision frequency profile is used. If the D-region parameters developed from propagation data by NOSC are used, the nighttime attenuation rate is significantly reduced. Calculations are also shown in Table 2-8 for a nighttime path between Utah and Hawaii. Except for sunspot minimum (1964) the results are similar to those for the northsouth path. For sunspot minimum conditions near 30 degrees latitude the E-region electron density is predicted to be quite small (see Table 2-4 and Figure 2-7) and the resulting ELF attenuation rate is large.

Clearly, the nighttime attenuation rates are critically dependent on the details of the electron density profile in the D- and E-regions. Calculations of reflected energy similar to those presented in Reference 2-17 are needed to study the relative importance of the regions. The nighttime electron densities obtained with the new model and NOSC parameters are smaller than would be predicted from the decay of daytime electron densities with the WEPH code chemistry model indicating that either the chemistry model is in error (detachment rates too high between 80 and 90 km), or the NOSC value of h_w is too high. The nighttime results also show some sensitivity to the ion-neutral collision frequency depending on the ion densities in the D-region. The ion densities in the new model (particularly the new model with NOSC D-region parameters) may be too low since the steady-state value of ion density can be less than the transient decay of the daytime ion density. Thus, the significance of the ion-neutral collision frequency may be understated if the actual ion densities are larger than modeled.

VLF Propagation Data

Figures 2-11 and 2-12 show results of daytime VLF measurements for propagation between Hawaii and San Francisco for summer conditions and Hawaii and Utah for winter conditions presented in Reference 2-2. Also shown are NOSC calculations for exponential electron density profiles. As discussed in Reference 2-2, the profile defined by $h_w = 70$, $\alpha_w = 0.35$ gives the best results for summer conditions and the profile defined by $h_w = 75$, $\alpha_w = 0.15$ gives the best results for winter conditions.

WEDCOM calculations at about 400 km intervals obtained with the new ionosphere (preliminary version) and ion-neutral collision frequency models are shown in Figures 2-12 and 2-13 for comparison with the measured data. The results for the 24 kHz propagation during summer are in reasonable agreement with the data and are about

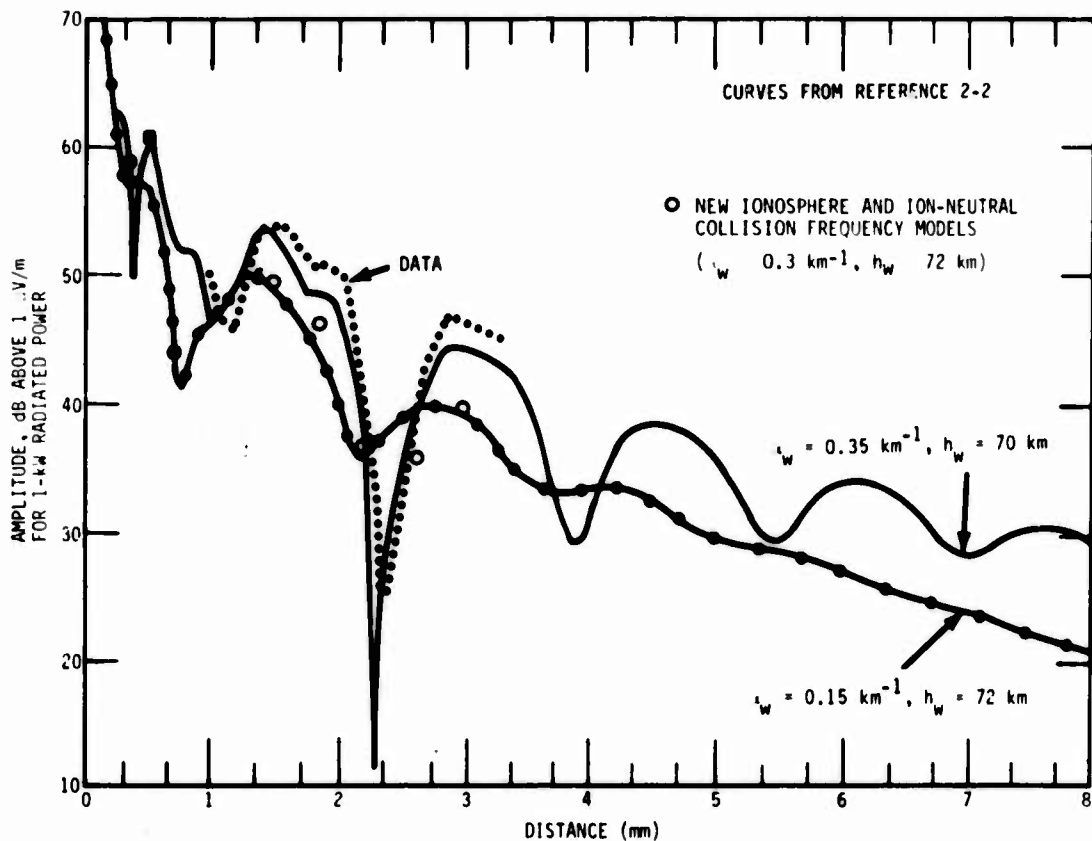


Figure 2-11. Propagation from San Francisco to Hawaii, May 18-19, 1965 (NPM 24 kHz).

midway between the two NOSC curves as would be expected from the value of h_w and α_w predicted in the new model.

The results for the 28 kHz propagation during winter show more variation from the data and from the NOSC calculations than for the previous case. Calculations were made with an exponential profile ($h_w = 75$, $\alpha_w = 0.15$) to check the propagation calculations. The results are essentially the same as the NOSC results and the small differences remaining can probably be attributed to differences in magnetic field, propagation angles and the number of profiles used to define propagation. Calculations were also made with the new ionosphere model with $\alpha_w = 0.15$ and $h_w = 75$ to see how much of the

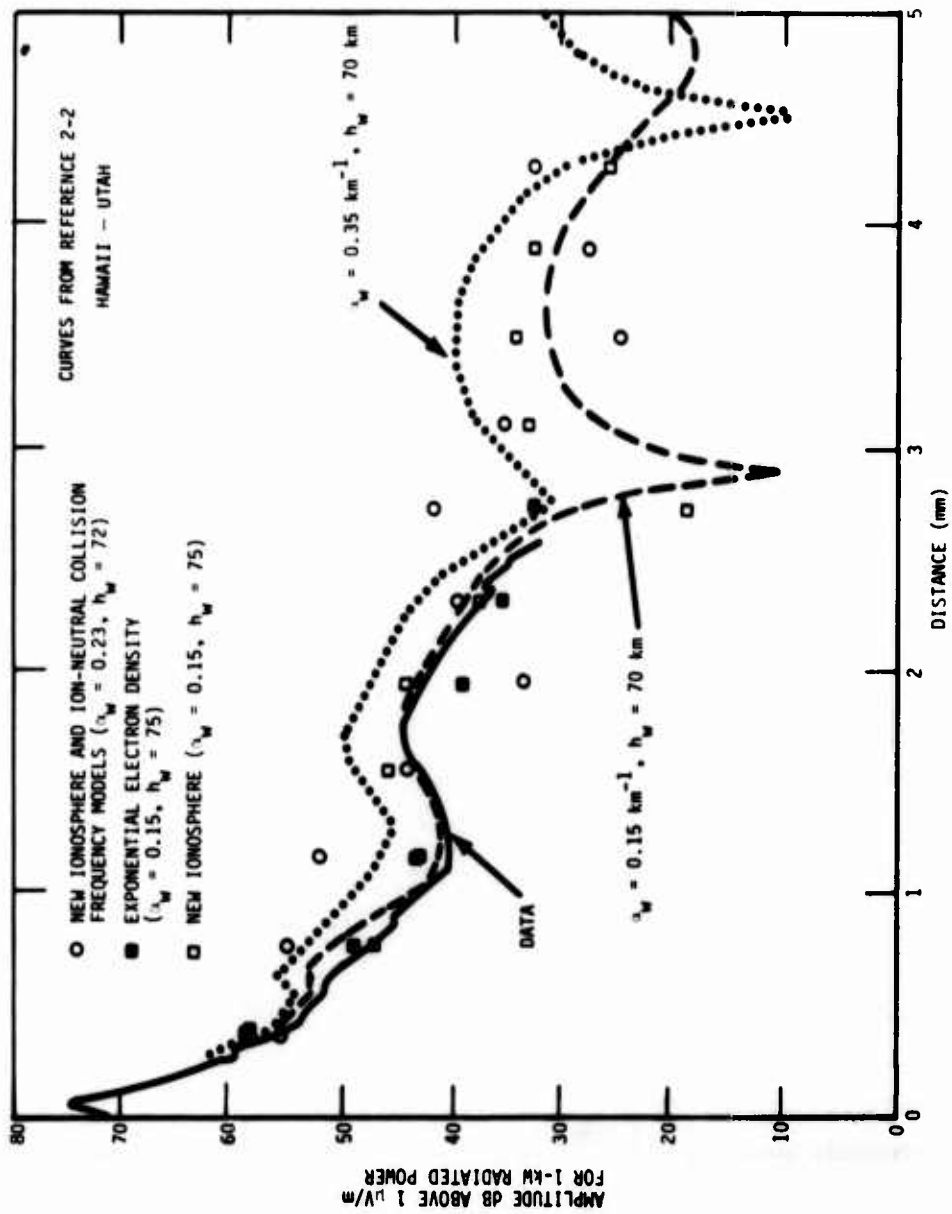


Figure 2-12. Propagation from Utah to Hawaii (daytime, February 1974), (28 kHz).

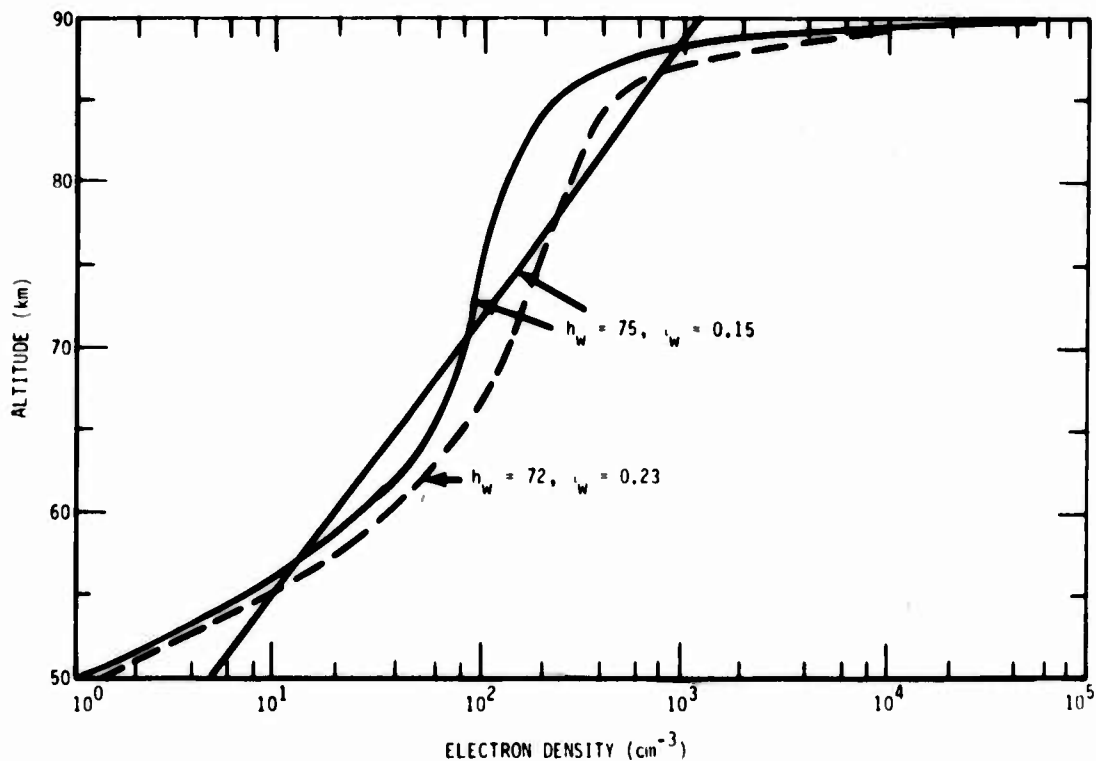


Figure 2-13. Daytime electron density profiles used for VLF calculations.

difference in results was due to the use of an exponential profile and how much was due to the profile parameters h_w and α_w . The several electron density profiles used are shown in Figure 2-13. For the case shown the electron density profile obtained with the preliminary and final versions of the new model are essentially the same. It would appear that the profile parameters recommended by NOSC provide better agreement with the data than those obtained from Equations 2-5 and 2-6. Note that the field strength calculated as the vector mode sum is sensitive to relatively small changes in the electron density profile. While specific profile parameters may be chosen empirically for ambient conditions, there is not sufficient data to do this for disturbed conditions. A more useful calculation for disturbed conditions is the rms mode sum which is not as sensitive to the details of electron density profile.

Figure 2-14 shows results of nighttime VLF measurements presented in Reference 2-2 for propagation between Hawaii and Ontario, California. As described in Reference 2-2, nighttime measurements show variation in propagation conditions from night to night and throughout a given night. WEDCOM calculations made with the exponential profile do not show the same interference pattern at close-in distances as the NOSC calculations. This is due to limiting the number of modes considered in the WEDCOM propagation model. The WEDCOM calculations for distances beyond 3000 km are slightly larger than those by NOSC and would be even larger if additional modes were considered. However, the attenuation rate is sensitive to the electron-neutral collision frequency used and the signal strength would be reduced if the exact collision frequency model used at NOSC was used in the WEDCOM calculations.

The calculations for the new ionosphere model with h_w and α_w determined from Equations 2-5 and 2-6 and set equal to NOSC values result in larger signal strengths than the exponential model. This is due to the larger electron density gradient near the reflection altitude (see Figure 2-15). The electron density gradient is larger for the new model, both because α_w is larger and because of the effect of the WEPH code chemistry model as previously described. When the NOSC values for h_w and α_w are used in the new model, the total production rates are less than the nominal cosmic ray values, and the method of reducing the cosmic ray ion production rate and determining the total production rate results in a larger electron density gradient. The final version of the new model results in an electron density profile similar to that for the preliminary model when the NOSC parameters are used.

Nighttime calculations at the upper end of the VLF band are the most difficult to do accurately and are affected by relatively small changes in the electron density gradient. As for daytime calculations, the vector mode sum is particularly sensitive to changes

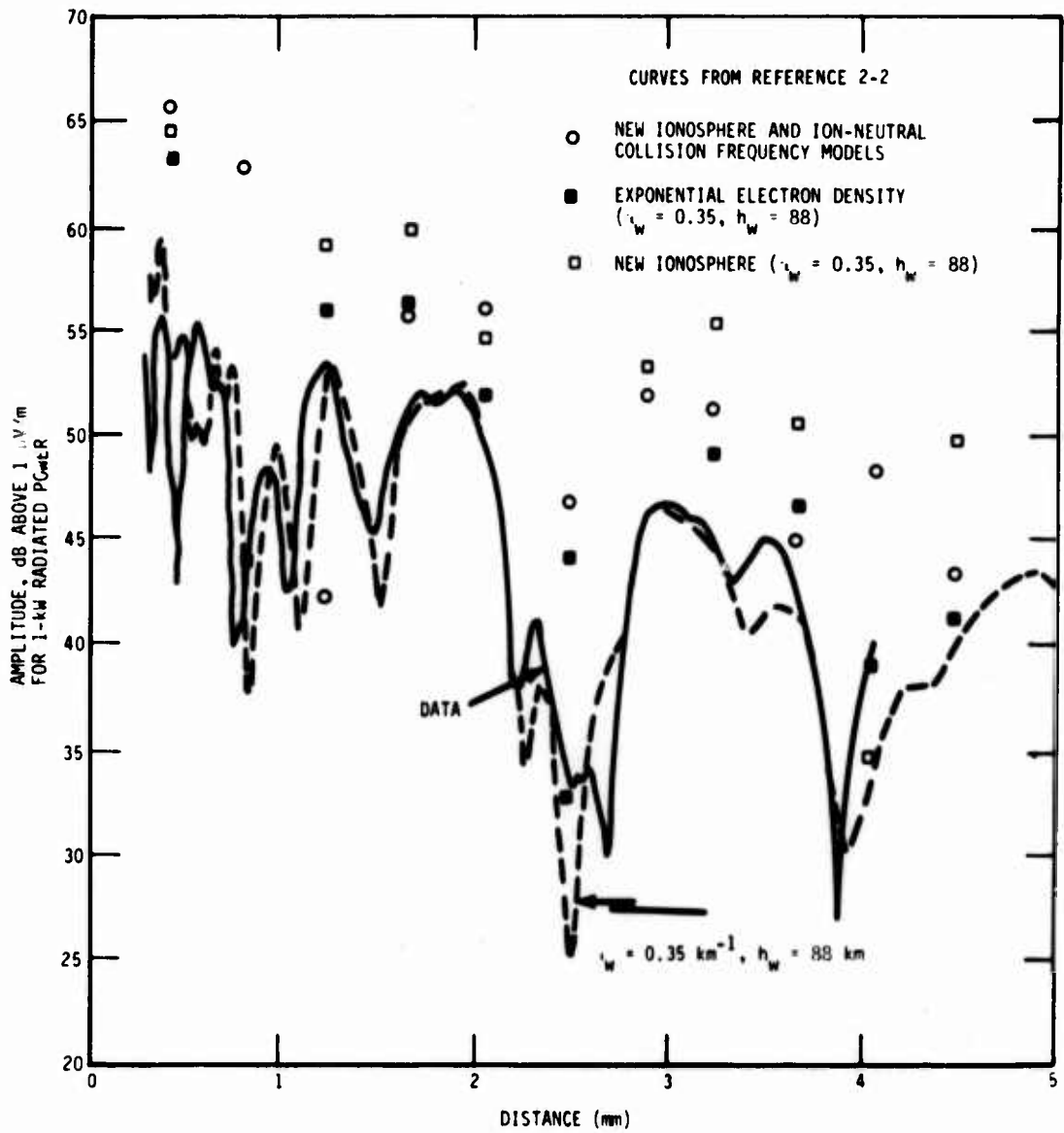


Figure 2-14. Propagation from Ontario, California to Hawaii (nighttime, 7 February 1969), (28 kHz).

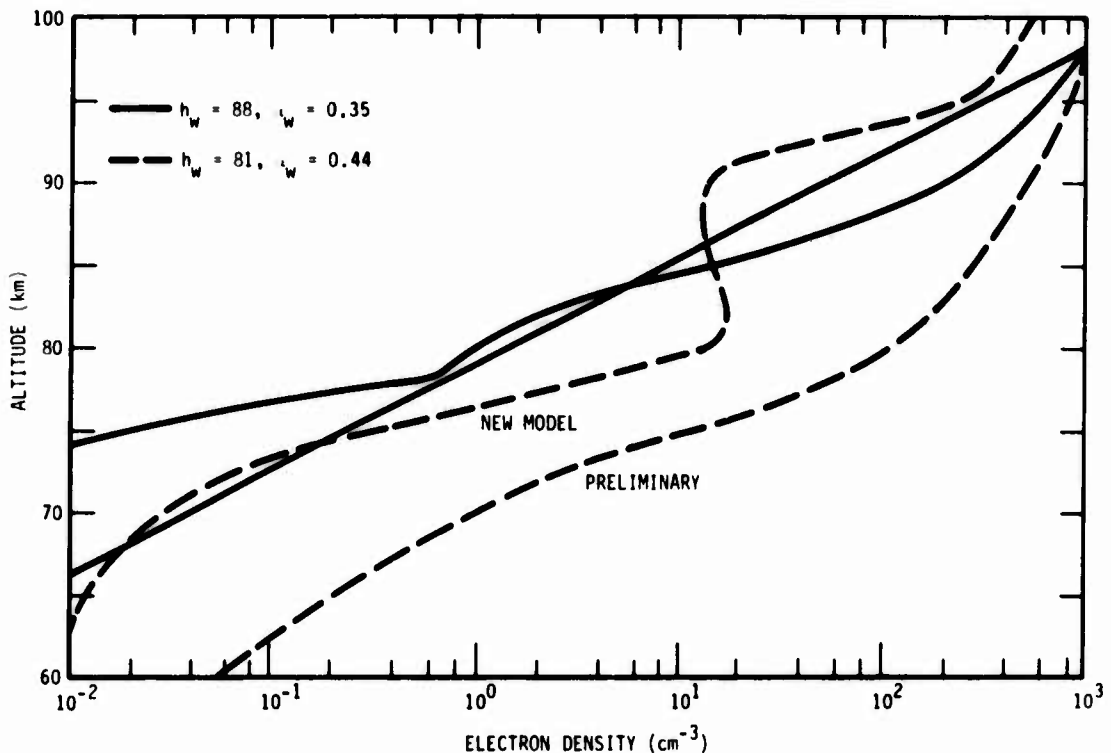


Figure 2-15. Nighttime electron density profile used for VLF calculation.

in the electron density profile and requires detailed matching to predict measured values (and consideration of a relatively large number of modes). The rms mode sum is less sensitive and, while more variable with electron density profile parameters than the daytime results, gives estimates of expected signal strength that are within the variations occurring from night to night.

HF Propagation Data

An ambient HF absorption relation is used in the ITS prediction code that is based on propagation data (Reference 2-18). When converted to one-way vertical absorption for 12:00 hours local time the relation becomes

$$A = \frac{143(1 + 0.0087|\theta|)W}{10.2 + (f + 1.4)^2} \cdot [(1 + 0.005 S) \cos^m x] \quad (2-23)$$

where

$$W = \begin{cases} 1.807 - 0.0269||\theta| - 60| & \text{for winter and } |\theta| \geq 30 \\ 1 & \text{for other conditions} \end{cases}$$

m = maximum (1.3, 2.25 - 0.032 $|\theta|$)

f = frequency (MHz)

S = smoothed 13-month sunspot number

x = solar zenith angle at noon

θ = geographic latitude (degrees) .

The ITS prediction program is being revised and a new absorption relation (Reference 2-19) developed. A preliminary version of the relation (converted to one-way vertical, noon time absorption) is

$$A = \frac{338 I}{10.2 + (f + 1.4)^2} \quad (2-24)$$

where

$$I = -0.04 + \exp(-2.937 + 0.8445 f_{OE}) .$$

In this expression the relation for absorption index I is in terms of f_{OE} , which includes the variation in latitude and solar activity. Table 2-9 shows comparisons of the predicted and calculated one-way vertical absorption at 15 MHz for different latitudes, seasons, and sunspot numbers.

The absorption results obtained with the new model (final version) are generally between those obtained with Equations 2-23 and 2-24. The summer predictions tend to be low except for 60 degrees latitude where the prediction is high. Changes in the NO concentration

Table 2-9. 15 MHz one-way vertical absorption, noon.

LATITUDE (DAY)	SEASON	SSN	COS X	EQUATION 23	EQUATION 24	NEW MODEL
10	Spring	111	0.98	0.8	2.5	1.8
10	Summer	96	0.97	0.8	2.1	0.7
10	Winter	68	0.	0.5	1.7	1.0
10	Spring	3	0.98	0.5	1.4	0.5
10	Summer	7	0.97	0.6	1.3	0.4
10	Winter	23	0.83	0.4	1.3	0.6
30	Spring	111	0.84	0.8	2.3	1.6
30	Summer	96	0.99	1.0	2.0	0.9
30	Winter	68	0.59	0.4	1.2	0.7
30	Spring	3	0.84	0.5	1.3	0.5
30	Summer	7	0.99	0.7	1.3	0.4
30	Winter	23	0.59	0.4	1.0	0.5
60	Spring	111	0.47	0.5	0.9	0.9
60	Summer	96	0.80	0.9	1.2	2.3
60	Winter	68	0.11	0.1	0.4	0.3
60	Spring	3	0.47	0.3	0.6	0.3
60	Summer	7	0.80	0.6	0.8	0.5
60	Winter	23	0.11	0.1	0.3	0.3

in the upper D-region would affect the results as well as changes in the scaling for h_w and α_w . Since the electron density profile in the new model is dependent on both the E-region critical frequency and the D-region parameters h_w and α_w , the variation with latitude and season is different than the new ITS model, which is only dependent on the E-region critical frequency.

SUMMARY

The structure of the new ionosphere model provides for latitude, season, and solar cycle variations. A better data base for D-region electron density profiles is needed to improve calculations of h_w and α_w . Partial reflection measurements being made on a routine basis at several latitudes by the U.S. Army Electronics Command may be useful in providing the data base.

Values for h_w and α_w obtained by NOSC from propagation measurements can be used in the model instead of values obtained from fits to electron density data (Equations 2-5 and 2-6). This would improve comparisons with measured VLF data presented by NOSC, particularly for daytime conditions. Additional scaling parameters to aid in modeling the electron density between h_w and the bottom of the E-region are needed. The D-region predictions would also be improved by having the atmospheric chemistry model dependent on latitude, season, and solar conditions. Use of the current WEPH code model may result in errors in predicting ion densities for both day and night conditions and the electron density gradient near 80 km for nighttime conditions. Use of steady-state relation may also underestimate nighttime electron and ion densities.

Further study of ELF propagation data is needed to determine the critical aspects of the E-region profile and whether the predicted profiles are adequate for propagation calculations. For both day and night conditions the VLF vector mode sum is critically dependent on the electron density profile and the rms mode sum is the more useful

descriptor for weapon effects codes. Benchmark data for comparison of HF absorption predictions are needed to determine whether the model is adequate for propagation calculations.

The major change to the ion-neutral collision frequency model was to parameterize the model in terms of ion mobility. While ambient propagation measurements show some sensitivity to the ion-neutral collision frequency model, uncertainties in electron and ion density profiles prevent further refinement of the ion mobility expression.

REFERENCES

- 2-1. Davis, R.M., Jr., and L.A. Berry, *A Revised Model of the Electron Density in the Lower Ionosphere*, TR111-77 Defense Communication Agency, Arlington, VA, prepared by Institute for Telecommunications Sciences, Office of U.S. Department of Commerce, 1 February 1977.
- 2-2. Morfitt, D.G., *Effective Electron Density Distributions Describing VLF/LF Propagation Data*, TR141, Naval Ocean Systems Center, San Diego, CA, 21 September 1977.
- 2-3. Baumann, E.J., et al, *Documentation of NUCOM II - An Updated HF Nuclear Effects Code*, private communications, April 1973.
- 2-4. Hamlin, D.A., and M.R. Schoonover, *The ROSCOE Manual, Volume 14a - Ambient Atmosphere (Major and Minor Neutral Species and Ionosphere)*, DNA3964F-14a, SAI-75-609-LF-2A, Science Applications, Inc., La Jolla, CA, 12 June 1975.
- 2-5. Shkarafsky, I., *Generalized Appleton-Hartree Equations for any Degree of Ionization, and Application to the Atmosphere*, Proc. IRE, vol 49, p 1857, 1961.
- 2-6. Arnold, H.R. and E.T. Pierce, *The Ionosphere Below 100 km (D-Region)*, RM11, Stanford Research Institute, Menlo Park, CA, September 1963.
- 2-7. Knapp, W.S., et al, *Reaction Rate, Collision Frequency, and Ambient Ionosphere Models for use in Studies of Radio Propagation in a Nuclear Environment*, DASA 1765, 66TMP-18, General Electric-TEMPO, Santa Barbara, CA, 1 March 1966.
- 2-8. Heaps, M.G., *The Ion Pair Production Rate due to Cosmic Rays*, MRC2641, USA Ballistic Research Laboratories, Aberdeen Proving Ground, Maryland, June 1976.
- 2-9. Whitten, R.C., et al, *HF Communication Effects Simulation: The Ionosphere Above 100 km, A Simple Model*, DASA 1539, ITR-6, Stanford Research Institute, Menlo Park, CA, August 1964.

- 2-10. Booker, H.G., "Fitting of Multi-Region Ionospheric Profiles of Electron Density by a Single Analytic Function of Height," *J. Atmos. Phys.*, vol 39, pp 619-623, 1977.
- 2-11. Olsen, R., private communication, Atmospheric Science Laboratory, White Sands Missile Range, White Sands, New Mexico, January 1978.
- 2-12. Phelps, A.V., *Electron Collision Frequencies and Radio-Frequency Absorption*, published as Chapter 21 of the Reaction Rate Handbook, DNA1948H, March 1972.
- 2-13. Rose, G., and H.U. Widdel, *Results of Concentration and Mobility Measurements for Positively and Negatively Charged Particles Taken Between 85 and 22 km in Sounding Rocket Experiments*, Radio Science, vol7, no. 1, pp 81-87, January 1972.
- 2-14. Pappert, R.A., and W.F. Moler, *Propagation Theory and Calculations at Lower Extremely Low Frequencies (ELF)*, IEEE Transaction on Communications, vol COM-22, no. 4, pp 438-451, April 1974.
- 2-15. Ginsberg, L.H., *Extremely Low Frequency (ELF) Propagation Measurements Along a 4900-km Path*, IEEE Transactions on Communications, vol COM-22, no. 4, pp 452-457, April 1974.
- 2-16. Bannister, P.R., *Far-Field Extremely Low Frequency (ELF) Propagation Measurements, 1970-1972*, IEEE Transactions on Communications, vol COM-22, no. 4, pp 468-474, April 1974.
- 2-17. Pappert, R.A., and L.R. Shockey, *Ionospheric Reflection and Absorption Properties of Normal Modes at ELF*, Interim Report, No. 772, EM Propagation Division, Naval Ocean Systems Center, San Diego, CA, 15 September 1977.
- 2-18. Barghausen, A.F., et al, *Predicting Long-Term Operational Parameters of High-Frequency Sky-Wave Telecommunication Systems*, ERL110-ITS-78, U.S. Department of Commerce (ESSA), Boulder, CO, May 1968.
- 2-19. Lloyd, John, *Ionospheric Communications Program (IONCAP) (U)*, ITS, Boulder, CO, Draft - to be published.

SECTION 3 HEAVE MODEL

INTRODUCTION

The fireball motion and atmospheric heave models are uncoupled in the current WEPH code and the heave model can underestimate atmospheric motion near the burst point. Thus, it is possible to have a highly heated and highly ionized region below the fireball that should have risen with the fireball. Because of fireball-like properties, this region has been called a "ghost fireball". In the RANC code, the ghost fireball problem was minimized by enlarging the initial fireball size to include air that could remain highly ionized. However, when the ROSCOE energy deposition models are used in conjunction with RANC fireball models, the initial fireball size is too small to prevent a ghost fireball for certain burst conditions.

The atmospheric heave model in the WEPH VI code was developed for the WOE code to reduce computation time relative to the previous heave model developed for the RANC code. The WOE code model also allows for "tying" the fireball and upwelling atmosphere together in terms of a fireball wake model (Reference 3-1). The fireball wake model forces the ghost fireball into the same region occupied by the real fireball.

Fireball Wake Model

The fireball wake is described by a right circular cylinder with radius

$$R_w = \text{minimum} \left(10 \frac{R_U + R_D}{2}, \sqrt{1.5} R_M \right) \quad (3-1)$$

where

R_U, R_D = upper and downward initial fireball radii,
respectively

R_M = fireball magnetic radius .

The top of the wake column is determined as the maximum of either the altitude a sonic wave would reach (assumed velocity is 0.5 km s^{-1}) or one-half of the upward fireball radius beyond the fireball; this modeling produces results somewhat similar to the bow wave that forms around a blunt object at subsonic velocities in much denser air.

The wake model is initialized by obtaining the Lagrangian coordinates of the top and a point near the bottom of the initial fireball. The Lagrangian coordinate of a point is the mass inventory of the air column above that point:

$$L_H = \int_H^{\infty} \rho \, dh \quad . \quad (3-2)$$

After some variations, a point one scale height below the bottom of the initial fireball was chosen as the bottom boundary of the rising fireball for the WEPH code model. This encompasses air that can be highly heated, dissociated, and ionized by the initial energy deposition.

A one-dimensional model allowing only vertical flow maintains the Lagrangian coordinate of every air parcel as an invariant property. By adjusting the computed Lagrangian coordinates in the burst axis air column to fit the predicted fireball position and its initially obtained coordinates, the developing fireball "draws" external air up with it as it rises. Figures 3-1 and 3-2 schematically indicate the initial definition of the fireball's Lagrangian coordinates and their subsequent use to adjust the heave model predictions in the vicinity of the fireball.

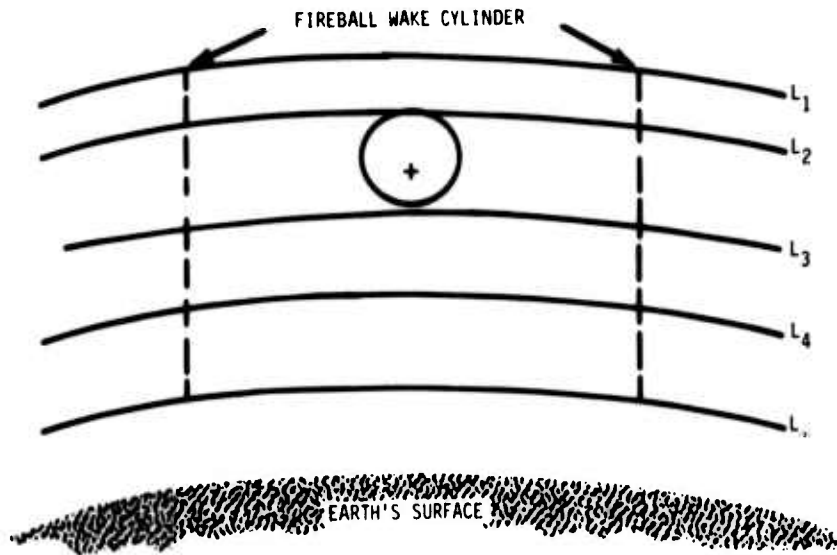


Figure 3-1. Lagrangian contours at burst time.

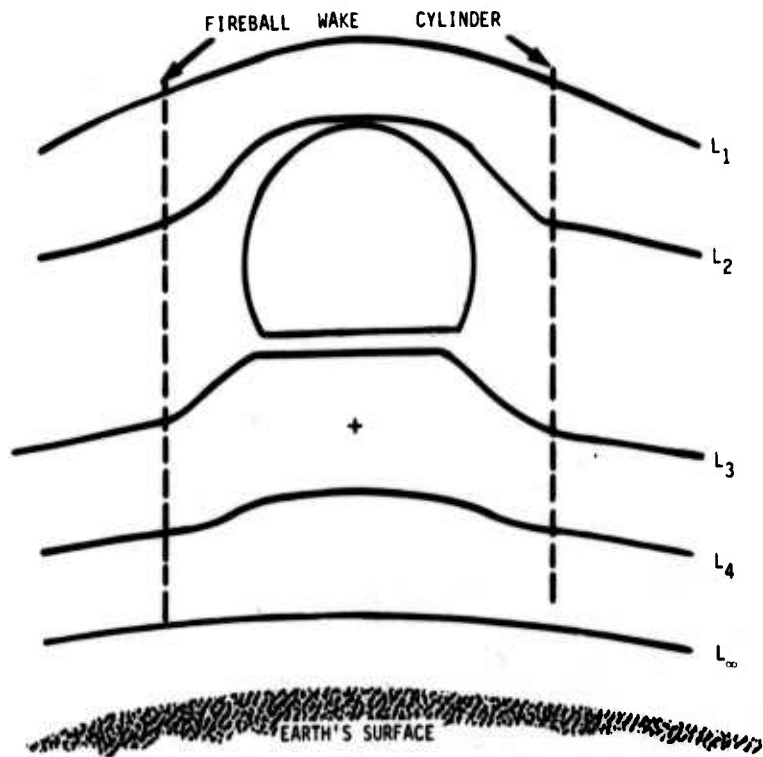


Figure 3-2. Lagrangian contours adjusted for fireball rise by the wake model.

A weighting function controls the adjustment of Lagrangian coordinates horizontally within the wake cylinder. It is a function of the ratio of horizontal range from the cylinder axis and the cylinder's radius:

$$W = \frac{2}{1 + \exp[16(r/R_w)^4]} \quad (3-3)$$

where r is the horizontal range. Vertically, a linear adjustment is made for points above the top of the fireball or below the bottom boundary (taken as one scale height below the fireball bottom). For points between the bottom boundary and the top of the fireball the Lagrangian coordinate value is scaled to match the boundary values and to approximate air motion within the fireball region. However, the model is not intended for detailed modeling of the fireball air properties and has been adjusted to underestimate electron density within the fireball region. The fireball overlay model provides estimates of fireball electron density.

Up to 10 fireball wakes may be superimposed. When overlaps occur, bursts are treated in their detonation order. In a multiburst scenario, Lagrangian coordinates are determined by the composite effect of atmospheric heave and existing fireball wakes. The coordinates of each successive fireball are determined in the wake environment of all previous fireballs.

Table 3-1 shows a comparison of electron density versus altitude along the vertical through the burst point 240 seconds after a multimegaton burst detonated in the E-region with and without the wake model. The bottom of the initial fireball (on the burst axis) is at 104 km and the bottom of the fireball at 240 seconds is at 486 km. Also shown in Table 3-1 is the starting altitudes for air reaching a given altitude at 240 seconds. When the wake model is not used the air starts at points within the initial fireball and even though the energy deposition is modified to not be larger than that at the fireball edge, the air is dissociated and remains highly ionized. When

Table 3-1. Comparison of electron density and initial air altitude at 240 seconds after burst on the burst axis with and without wake model.

Altitude (km)	No Wake		Wake	
	Electron Density (cm^{-3})	Initial Altitude (km)	Electron Density (cm^{-3})	Initial Altitude (km)
120	6.9(10)	107.8	3.8(4)	93.2
140	3.4(10)	110.2	2.6(4)	93.5
160	2.6(10)	112.3	2.2(4)	93.7
180	2.0(10)	114.4	1.8(4)	93.8
200	1.6(10)	116.3	1.2(3)	93.9
220	1.3(10)	118.3	9.3(2)	93.9
240	1.2(10)	120.0	7.4(2)	94
260	1.1(10)	122.2	6.0(2)	94
280	1.1(10)	124.1	6.0(2)	94
300	9.7(9)	126.2	6.0(2)	94

the wake model is used the air starts far enough below the fireball that ionization is quickly lost by dissociative recombination.

A late-time ghost fireball can also be caused by procedures used in modeling air motion and changes in air density for times after burst when air has returned to its initial altitude. In the current WEPH code model early-time motion is estimated by computing the air location and density at 100-second intervals starting at 300 seconds after the last burst and continuing until 100 seconds after the first burst. While generally providing good estimates of the air motion, the procedure does miss the apogee time sufficiently in some case to significantly underestimate the amount of volume expansion during rise. A new procedure in which the apogee times between bursts and after the last burst are estimated has been prepared that provides much better estimates of apogee times and thus the maximum effects of volume expansion.

After reaching apogee the air falls and the air density increases. In the WEPH code model the increase in air density is interpreted as air entrainment. This procedure is intended to return air to preburst conditions when the heave motion has ended. In the current model the properties of the entrained air are taken as those of the ambient air at the altitude of the air parcel as it falls. This procedure tends to underestimate air entrainment near the final altitude and in some cases the air temperature remains above ambient after reaching the final altitude. In the revised model the properties of the entrained air are always taken as those of ambient air at the final altitude.

The heave model was developed to provide estimates of changes in air density and interpretation of the model in terms of particle motion is fictitious, particularly after the air parcels reach apogee. The current modeling including the use of entrainment is a method for using the heave model in a manner that is expected to provide reasonable estimates for a few hundred seconds (until apogee times) and that will return the atmosphere to ambient conditions at late times. However, since the motion model is independent of the air temperature, there can still be cases where air temperatures remain above ambient at late times. These cases occur when the air motion due to X-rays and heavy particle energy deposition is small and heating due to UV energy deposition raises the gas temperature. It can also occur when energy in metastable states is returned to kinetic energy and heats the gas. Generally, the increase in air temperature above ambient is relatively small for these cases.

REFERENCES

- 3-1. Stanton, M.J., et al, private communication describing the Weapon Optical Effects Code, General Electric—TEMPO, September 1975.

SECTION 4 CHEMISTRY MODELS

INTRODUCTION

Outside the fireball, separate atmospheric chemistry models are used in the WEPH VI code for the D-region (altitudes below 100 km) and the E- and F-regions (altitudes above 100 km). Because of simplifications used in the models, there can be discontinuities in ionization near the boundary between the two models. While this is allowed for in some calculations (eg, refraction), it can result in potential errors in calculating propagation effects. The following describes chemistry model improvements to minimize ionization discontinuities and to incorporate new chemistry modeling recently prepared for ROSCOE.

D-REGION CHEMISTRY MODEL

The D-region chemistry model used in the WEPH VI code was first developed for ROSCOE (Reference 4-1). For daytime conditions the effect of burst produced odd nitrogen on the ambient values of O, O₃, O₂(¹Δ), NO, and NO₂ is estimated from the total odd nitrogen produced and effective photodissociation rates determined from the preburst ambient species concentrations. The ROSCOE chemistry models have recently been updated to include species required in optical predictions (Reference 4-2). In performing this work it was found that including the odd hydrogen species H, OH, and HO₂ in the model could significantly modify the effect of burst-produced odd nitrogen on the late-time, ambient daytime atmosphere.

In order to include the new species in the WEPH code it is first necessary to add the species to the ambient atmosphere model.

The ambient model prepared for ROSCOE by SAI (Reference 4-3) has been used to modify the WEPH code ambient model. Table 4-1 shows the day and night ambient values for the odd hydrogen species used in the model. The species concentrations are not functions of location, season, or solar conditions. Next, the relations determining the effective photodissociation rates are modified to include the new species and reactions involving the new species are added to those determining the effect of burst-produced odd nitrogen. In determining the new ambient species concentrations and the transient decay from burst-produced conditions the formulations given in Reference 4-1 have been modified to simplify the calculations and to insure convergence of the solutions (Reference 4-2).

Figure 4-1 shows the change in the daytime ambient odd oxygen species ($O + O_3$) versus the amount of odd nitrogen ($NO + NO_2$). The subscript 0 refers to preburst ambient conditions. The two curves shown in Figure 4-1 labeled WEPH code are calculations for the WEPH code neutral species model (developed by SAI for ROSCOE) and show the effect of including and neglecting the odd hydrogen species. While including the odd hydrogen species has considerable effect on the reduction of the oxygen species, the effect is less than expected based on benchmark calculations prepared by Schiebe for development of the new chemistry models for ROSCOE. The two curves in Figure 4-1 labeled ROSCOE Benchmark are for the ambient neutral species used by Scheibe in preparing the benchmark calculations. Note that the reduction in odd oxygen is much less for Scheibe's neutral species model even when the odd hydrogen species are neglected. In order to determine the cause of the difference, calculations were made for a weapon-produced odd-nitrogen concentration of $4 \times 10^{10} \text{ cm}^{-3}$ and changes were made in the preburst distribution of oxygen and nitrogen species. Figure 4-2 shows calculation as a function of the ratio of $[O]_0$ to ξ_0 where $\xi_0 = [O]_0 + [O_3]_0$ was held constant at $2 \times 10^{10} \text{ cm}^{-3}$. Figure 4-3 shows similar results as a function of the ratio of

Table 4-1. Ambient species concentrations (cm^{-3})
for H, OH, and HO₂ used in ROSCOE.

Altitude (km)	H		OH		HO ₂	
	Day	Night	Day	Night	Day	Night
0	7.0(-3)	0.0	1.0(6)	1.7(2)	1.0(5)	4.9(1)
5	7.6(-3)	0.0	1.0(6)	1.8(2)	7.5(5)	4.2(2)
10	1.0(-3)	0.0	1.05(6)	2.1(2)	2.4(6)	1.6(3)
15	1.6(-2)	0.0	1.15(6)	2.7(2)	6.9(6)	5.9(3)
20	5.2(-2)	0.0	1.5(6)	4.2(2)	1.15(7)	1.4(4)
25	3.2(-1)	0.0	2.3(6)	8.1(2)	1.5(7)	2.7(4)
30	2.9(0)	0.0	4.0(6)	2.0(3)	1.6(7)	4.7(4)
35	1.0(2)	0.0	6.8(6)	8.0(3)	1.5(7)	8.3(4)
40	4.0(4)	0.0	1.05(7)	5.7(4)	1.2(7)	1.3(5)
45	1.0(5)	0.0	1.1(7)	2.9(5)	9.1(6)	2.4(5)
50	2.4(5)	0.0	9.5(6)	1.2(6)	6.6(6)	4.6(5)
55	5.1(5)	0.0	7.2(6)	4.4(6)	4.2(6)	6.9(5)
60	1.0(6)	0.0	5.3(6)	6.5(6)	2.2(6)	7.3(5)
65	1.8(6)	0.0	3.7(6)	5.9(6)	7.9(5)	4.6(5)
70	4.9(6)	0.0	2.5(6)	4.5(6)	4.2(6)	3.5(6)
75	1.25(7)	5.0(2)	1.6(6)	3.2(6)	1.2(7)	1.2(7)
80	3.5(7)	1.0(8)	7.0(5)	1.6(6)	9.2(6)	9.2(6)
85	8.6(7)	8.6(7)	7.0(4)	1.7(5)	5.7(4)	5.7(4)
90	7.4(7)	7.4(7)	6.3(3)	1.7(4)	5.7(3)	5.7(3)
95	5.0(7)	5.0(7)	5.7(2)	1.7(3)	4.9(2)	4.9(2)
100	3.0(7)	3.0(7)	6.7(1)	2.2(2)	7.4(1)	7.4(1)

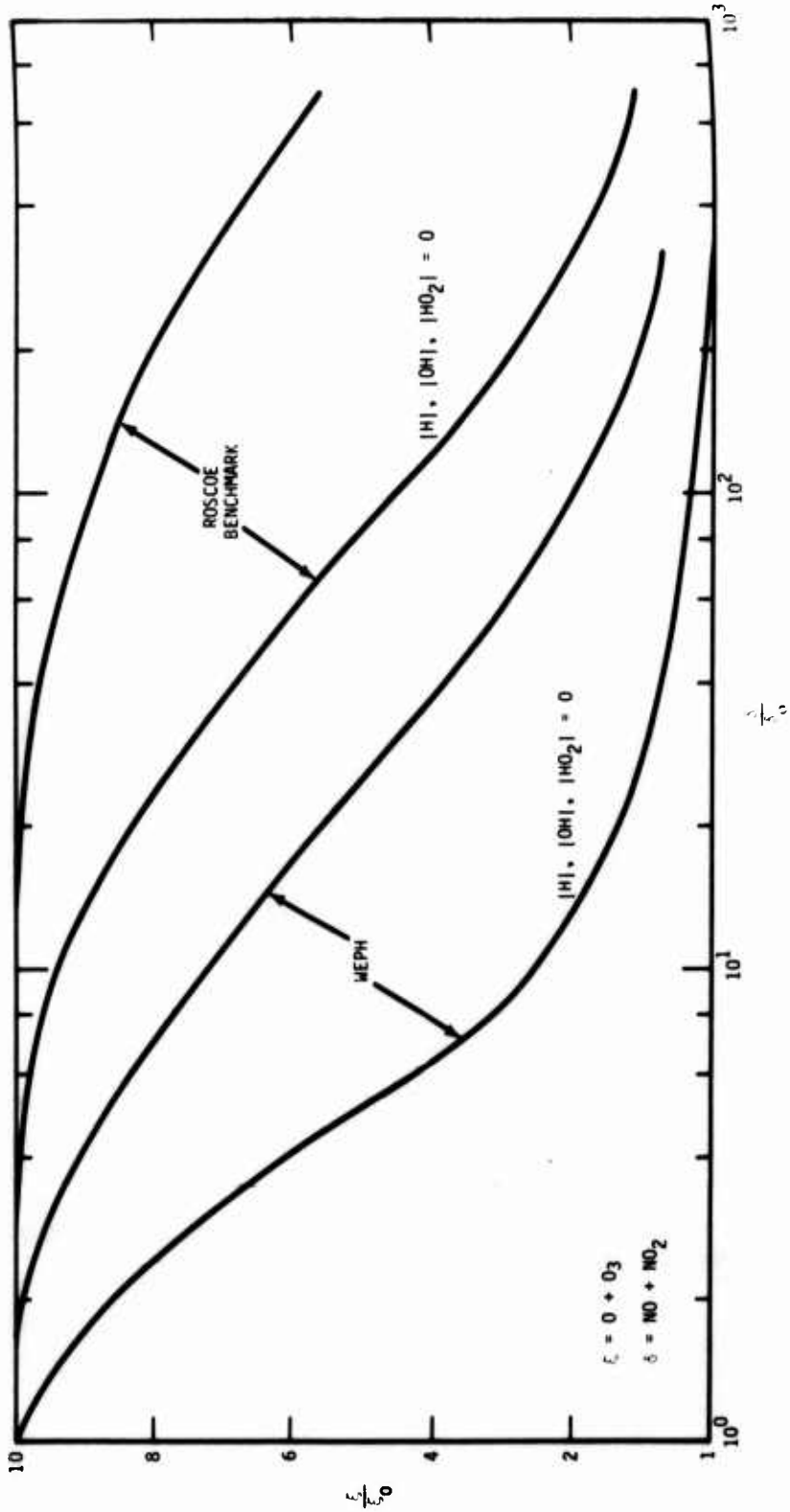


Figure 4-1. Changes in the steady-state odd oxygen concentration at 60 km as a function of the odd nitrogen concentration.

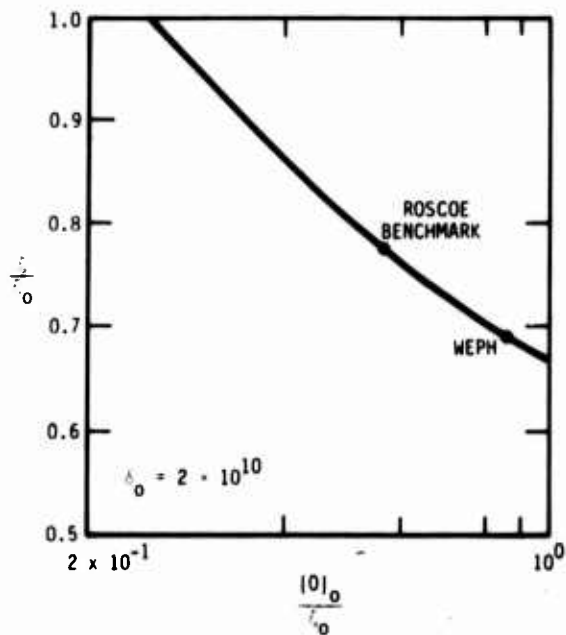


Figure 4-2. Changes in the steady-state odd oxygen concentration as a function of $[O]_0/\epsilon_0$, $\delta = 4 \times 10^{10} \text{ cm}^{-3}$.

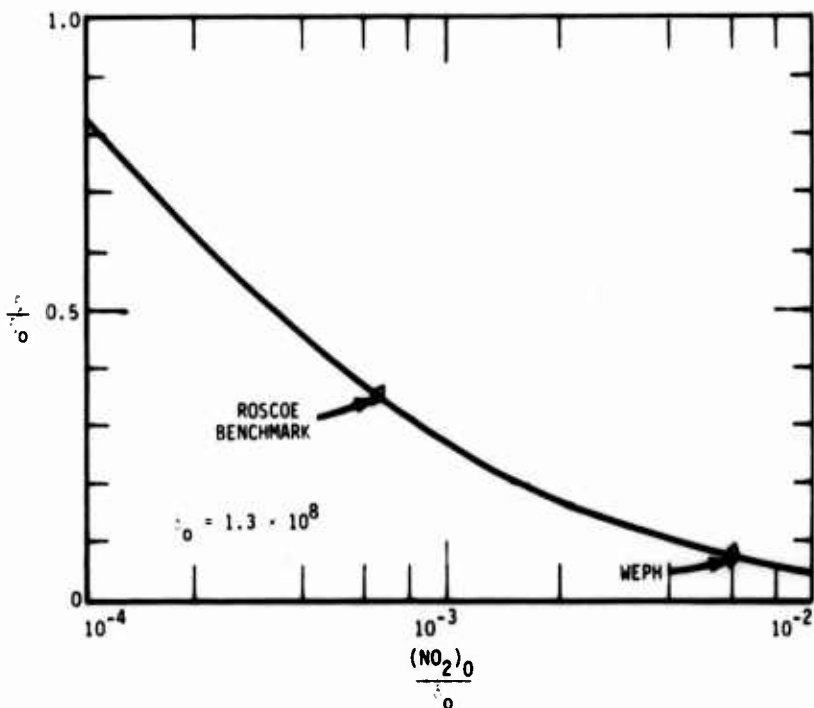


Figure 4-3. Changes in the steady-state odd oxygen concentration at 60 km as a function of $[NO_2]_0/\delta_0$, $\delta = 4 \times 10^{10} \text{ cm}^{-3}$.

the ratio of $[\text{NO}_2]_0$ to δ_0 where $\delta_0 = [\text{NO}_2]_0 + [\text{NO}]_0$ was held constant at $1.3 \times 10^8 \text{ cm}^{-3}$. The calculations show that the reduction in odd oxygen caused by burst-produced odd nitrogen is very sensitive to the preburst ratio of $[\text{NO}_2]_0$ to δ_0 . This is due to the computation of effective photodissociation rates from the preburst ambient species. In the WEPH code model the ambient NO_2 density at 60 km is large enough to cause the effective photodissociation of NO_2 to become negative. Further detailed studies with multispecies chemistry codes are needed to determine the critical parameters affecting the reduction in oxygen species and the allowable range in these parameters. A better way of determining the preburst ambient species is also needed that is consistent with the chemistry models used. Above about 50 km the daytime concentration of NO_2 is determined by photodissociation and the ambient daytime value should be limited by the photodissociation rate. Figure 4-4 shows the current WEPH code daytime ambient values for NO_2 and modified values determined by computing the NO_2 concentration from the photodissociation rate used by Scheibe when the effective photodissociation rate determined from the species concentrations becomes less than that used by Scheibe. Use of the modified ambient NO_2 concentration results in a much smaller reduction in odd oxygen concentration at 60 km for a given burst-produced odd nitrogen concentration as shown in Figure 4-3. Figure 4-5 shows the reduction in daytime odd oxygen as a function of altitude due to the odd nitrogen produced by an ionization impulse of 10^{11} ion pairs cm^{-3} . Since most of the daytime detachment rate is due to oxygen species, the amount of reduction, particularly above about 55 km, can be significant in propagation predictions.

In the current WEPH code the nitrogen vibrational temperatures and electron kinetic temperature are not modified by energy deposition in the D-region chemistry model. This causes a discontinuity in the reaction rate coefficients (primarily the dissociative recombination coefficient) and thus the electron density near 100 km. In addition to the odd hydrogen species, the new D-region chemistry model for

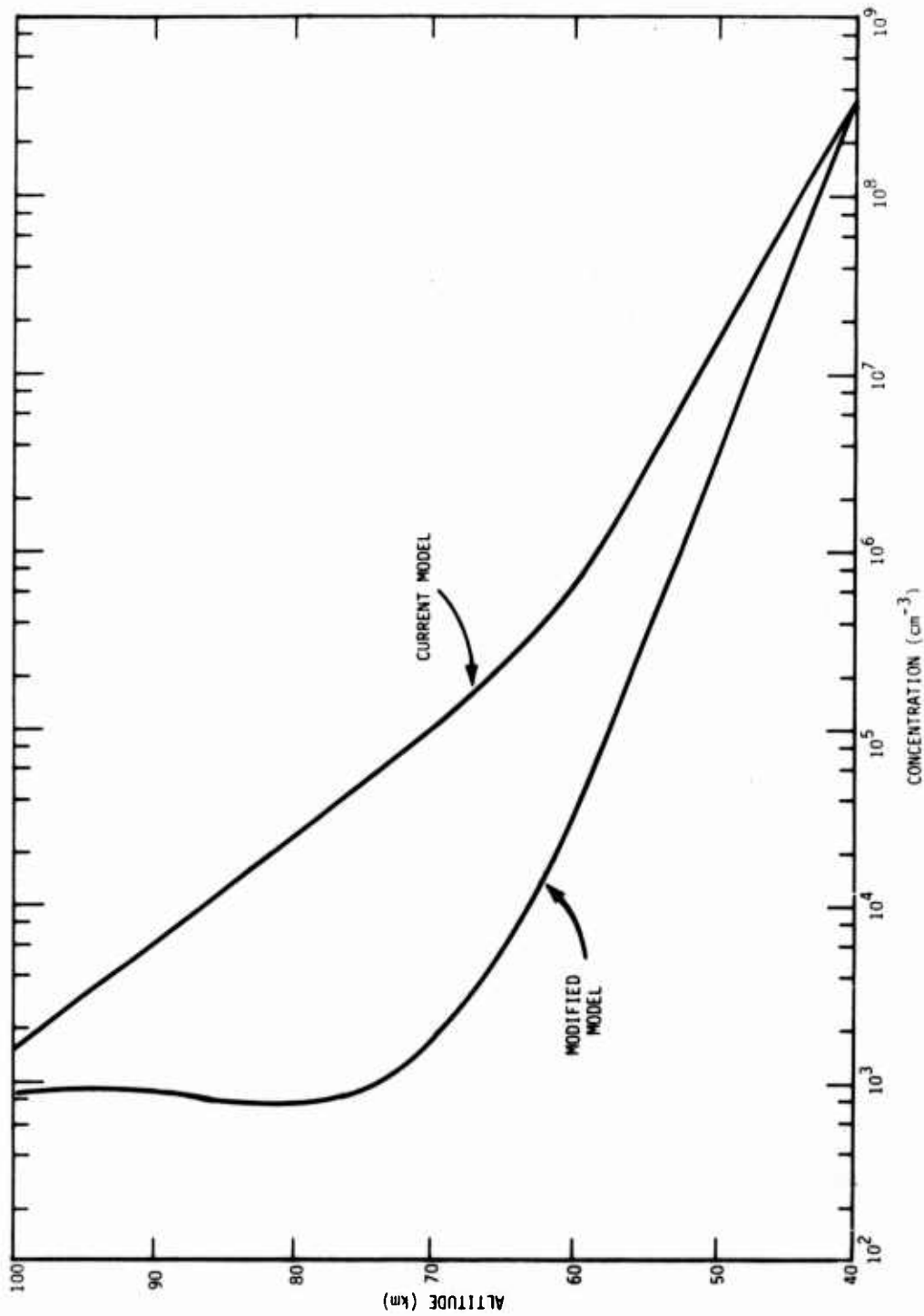


Figure 4-4. Current and modified values for ambient daytime NO₂ concentration.

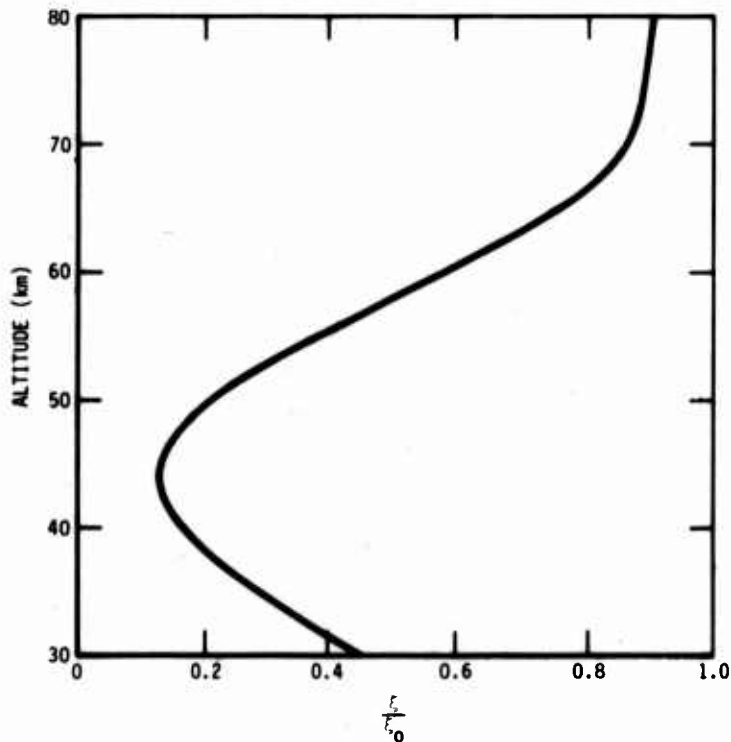


Figure 4-5. Reduction in odd oxygen as a function of altitude, $N_0 = 10^{11}$ ion pairs cm^{-3} .

ROSCOE includes a prediction for the concentration of the first vibrational level of molecular nitrogen. If a Boltzmann distribution for the number density in the excited state is assumed, a nitrogen vibrational temperature can be computed from

$$T_X = \frac{-0.3}{\ln(B)} \text{ ev} \quad (4-1)$$

where

$$B = 0.5 - (0.25 - N_2(v=1)/N_2)^{1/2}$$

$N_2(v=1)$ = concentration of molecular nitrogen in first vibrational level

N_2 = total concentration of molecular nitrogen .

If it is also assumed that the nitrogen vibrational and electron kinetic temperatures are equilibrated, then

$$T_e = T_X \quad (4-2)$$

where T_e is the electron temperature. A modified dissociative recombination coefficient can be computed from

$$\alpha'_d = \alpha_d \frac{T_g}{T_e} \quad (4-3)$$

where

α_d = dissociative recombination coefficient computed assuming $T_e = T_g$ and T_g equals the gas kinetic temperature .

Figure 4-6 shows T_X versus time for parametric D-region altitudes following an energy deposition impulse producing 10^{11} ion pairs cm^{-3} .

A number of the D-region rates have been modified since preparation of the chemistry model for ROSCOE. Appendix A shows rates given in Reference 4-1 (used in the current WEPH code) and revised rates suggested by Niles (Reference 4-4) and Scheibe (Reference 4-5).

E- AND F-REGION CHEMISTRY MODEL

The E- and F-region chemistry model used in the WEPH code was developed for ROSCOE and includes modeling of an excitation temperature that describes equilibrium Boltzmann distributions of free electron kinetic energy, oxygen electronic states, and nitrogen vibrational states. The excitation energy is modified due to the changing species concentrations, by elastic collisions between electrons and heavy particles, quenching of the $O(^1D)$ by N_2 , quenching of the N_2 vibrational states by CO_2 and heating or cooling of electrons during collisional excitation of $N(^4S)$ or deexcitation of $N(^2D)$. In order to improve the interface between the E- and F-region chemistry model and the D-region chemistry model, quenching of N_2 vibrational states

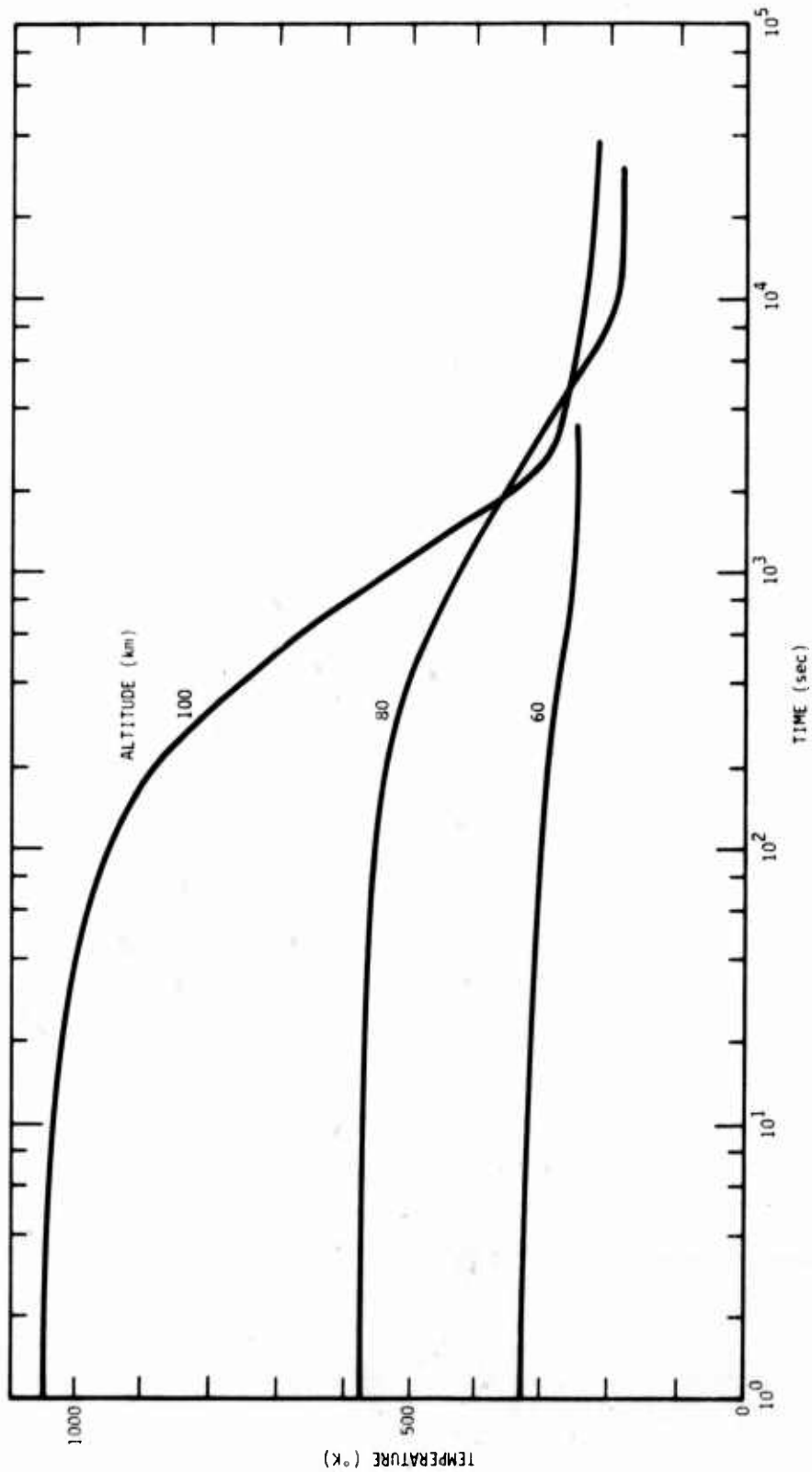


Figure 4-6. Nitrogen vibrational temperature following ionization impulse of 10^{11} ion pairs cm^{-3} .

by O and O₂ has been added and the modeling of collisional excitation and deexcitation of nitrogen atoms has been modified. Also, the formation of N(⁴S) and N(²D) by X-rays has been modified and reactions affecting the formation and loss of NO from nitrogen atoms have been revised to account for the rapid formation of NO by N(²D).

In the E- and F-region model the initial species concentrations are determined from relations developed by SAI for X-rays, heavy particles, and UV (Reference 4-6). For X-rays the change in species due to the initial dissociation is neglected. In the D-region model the effects of dissociation are included and result in 0.45 N(⁴S) atoms and 0.61 N(²D) atoms per ion pair. Neglect of the production of N(²D) by dissociation can significantly affect the decay of N(⁴S) near 100 km. The relations used below 100 km have also been used above 100 km to account for quenching of N₂ vibrational energy. Since water molecules are not modeled above 100 km, reactions involving water molecules in Archer's model were eliminated (Reference 4-2). Figure 4-7 shows a comparison of the nitrogen vibrational temperature computed at 100 km altitude with the D-region model and the E- and F-region model following a particular energy deposition impulse. The initial decay of vibrational temperature is nearly the same for both models. The ambient gas temperature at 100 km is 200°K. When the D-region model is used the vibrational temperature decays until reaching about 220°K. This temperature is due to the production of vibrational energy by the ambient ion-pair production rate. When the E- and F-region model is used the vibrational temperature decays until reaching about 400°K. This temperature is the gas kinetic temperature which has been raised in the E- and F-region model due to energy deposition. The heave model does not predict enough motion to result in cooling the air and it remains above ambient.

The calculation procedure used in the current E- and F-region chemistry model is to first treat the ion chemistry (reactions 1 through 16 in Appendix B), including changes in ion concentrations

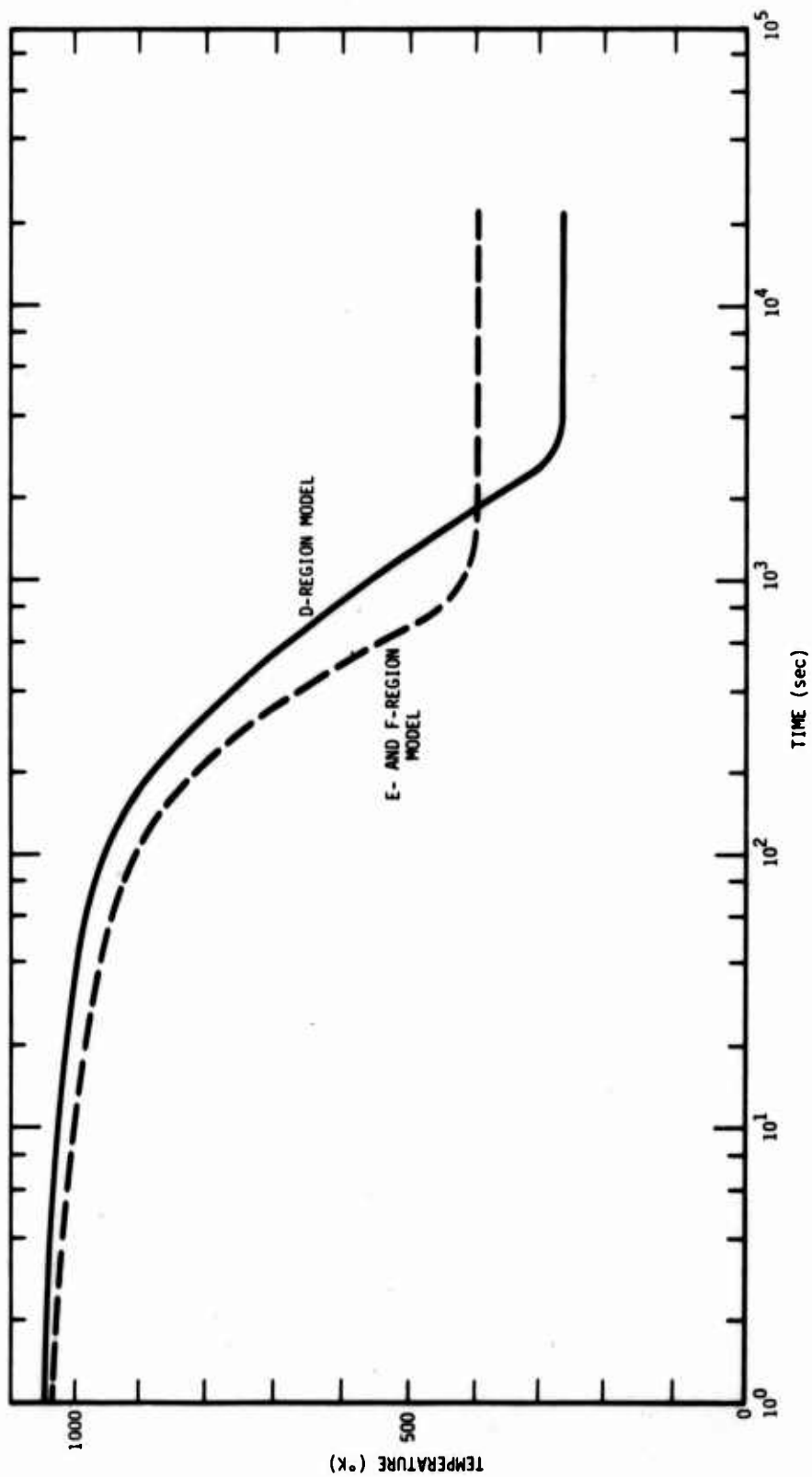


Figure 4-7. Comparison of nitrogen vibrational temperature at interface between D-region and E- and F-region models.

and the associated changes in neutral species concentrations. Then the neutral chemistry (reactions 19 through 25) is computed using effective mean values of the species determined from the result of the ion chemistry. The mean values are computed assuming an exponential change in species concentration with time during the time interval. It has been found that the assumption of an exponential change can overestimate the mean value of electron density when dissociative recombination dominates the early decay of ionization. Also, the use of mean values can overestimate reactions between species produced during the time interval.

In order to improve the neutral chemistry calculations, particularly near the boundary between the D-region and E- and F-region models, the order of the neutral chemistry calculations and the approximations used have been modified. In the current model the nitric oxide chemistry (reactions 5, 19 through 22, and 25) is computed first and then the equilibration of $N(^4S)$ and $N(^2D)$ due to reactions 23 and 25 is determined. This has been changed to the following steps:

1. Determine the equilibration of the $N(^4S)$ and $N(^2D)$ available at the start of the time interval using an approximate form for the electron density decay during the interval. Nitrogen atoms produced by the ion chemistry are not equilibrated in this step.
2. Determine the loss of $N(^2D)$ by reactions 20 and 22.
3. Determine the loss of $N(^4S)$ by reactions 19 and 21.
4. Determine the production and loss of NO by reactions 5 and 25.
5. Estimate the equilibration of $N(^4S)$ and $N(^2D)$ after the NO chemistry using the electron density at the end of the time interval.

In step 1 the electron density is assumed to decay by recombination during the time interval and an effective recombination coefficient determined from

$$\alpha_e = \frac{\frac{N_{e1}}{N_{e2}} - 1}{N_{e1}(t_2 - t_1)} \quad (4-4)$$

where

N_{e1}, N_{e2} = electron densities at start and end of time interval respectively.

The equilibration of $N(^4S)$ and $N(^2D)$ by reactions 23 and 24 can be determined by assuming that the total number of nitrogen atoms remains constant,

$$N_T = [N(^4S)]_1 + [N(^2D)]_1 \quad (4-5)$$

and using the assumed form for the electron density decay. Solving for $N(^2D)$ gives

$$\frac{d[N(^2D)]}{dt} = - (k_{23} + k_{24}) [N(^2D)] N_e + k_{23} N_e N_T \quad (4-6)$$

$$N(^2D)_2 = \frac{[N(^2D)]_1 - [N(^2D)]_\infty}{[1 + \alpha_e N_{e1}(t_2 - t_1)]^y} + [N(^2D)]_\infty \quad (4-7)$$

where

$$[N(^2D)]_\infty = \frac{k_{23}}{k_{23} + k_{24}} N_T$$

$$y = \frac{k_{23} + k_{24}}{\alpha_e} .$$

The concentration of $N(^4S)$ after equilibration is then

$$[N(^4S)]_2 = N_T - [N(^2D)]_2 \quad (4-8)$$

In step 2 the loss of $N(^2D)$ due to reactions 20 and 22 is determined. For these reactions

$$\frac{d[N(^2D)]}{dt} = -k_{20}[N(^2D)][O_2] - k_{22}[N(^2D)][NO] \quad (4-9)$$

$$\frac{d[NO]}{dt} = k_{20}[N(^2D)][O_2] - k_{22}[N(^2D)][NO] \quad (4-10)$$

These equations are similar to the ozone-oxygen equations in the D-region for which the following approximate solutions have been given by Scheibe (Reference 4-7).

$$\begin{aligned} \xi = \xi_0 + \left(\frac{C}{D} - \xi_0\right) \left(1 - e^{-ADt}\right) + \frac{C^4}{D^5} \left(1 - e^{-ADT}\right)^4 + \\ \frac{4C^7}{D^9} \left(1 - e^{-ADt}\right)^7 + \dots \end{aligned} \quad (4-11)$$

$$\eta = \eta_0 \exp(-A(1 + \xi_m)t) \quad (4-12)$$

where

t = time interval

$$\xi = \frac{B}{A} [NO]$$

$$\eta = \frac{B}{A} [N(^2D)]$$

$$A = k_{20}[O_2]$$

$$B = k_{22}$$

$$C = \eta_0 - \xi_0 - \ln(1 - \xi_0)$$

$$D = 1 + C$$

$$\xi_m = \xi_0 + \left(\frac{C}{D} - \xi_0\right) L + \frac{C^4}{D^5} L^4 + \frac{4C^7}{D^9} L^7 + \dots$$

$$L = \left(1 - \frac{1 - e^{-ADt}}{ADt} \right) .$$

In the above equations it is assumed that the concentration of O_2 remains constant. The loss of O_2 can be computed from

$$\frac{d[O_2]}{dt} = - k_{20} [N(^2D)] [O_2] . \quad (4-13)$$

Substituting for $N(^2D)$ from Equation 4-12 and solving for O_2 gives

$$[O_2] = [O_2]_1 \exp \left\{ \frac{k_{20} [N(^2D)]_2 - [N(^2D)]_1}{A(1 + \xi_m)} \right\} . \quad (4-14)$$

If the value of $N(^2D)$ is larger than the value of O_2 at the start of the time interval, the loss of O_2 and $N(^2D)$ by reaction 20 is computed first from

$$\frac{d[O_2]}{dt} = - k_{20} [O_2] [(O_2) + \delta] \quad (4-15)$$

where

$$\delta = (N(^2D)_1 - [O_2]_1) .$$

The solution for Equation 4-15 is

$$[O_2]_2 = \frac{\delta G}{1 - G} \quad (4-16)$$

where

$$G = \frac{[O_2]_1}{[O_2]_1 + \delta} \exp \left\{ - k_{20} \delta t \right\} .$$

For $k_{20} \delta t \ll 1$

$$[O_2]_2 = \frac{[O_2]_1 - [O_2]_1 k_{20} \delta t}{1 + k_{20} [O_2]_1 t} . \quad (4-17)$$

The amount of $N(^2D)$ at the end of the interval is

$$[N(^2D)]_2 = [O_2]_2 + \delta \quad (4-18)$$

and the amount of NO produced is just equal to the loss of O_2

$$[NO] = [O_2]_1 - [O_2]_2 \quad (4-19)$$

Next, the loss of $N(^2D)$ and NO by reaction 22 is computed. The solution is similar to that given above where the O_2 is replaced with the smaller of the $N(^2D)$ and NO and δ is equal to the difference between them.

In step 3 the loss of $N(^4S)$ due to reactions 19 and 21 is determined using the solutions described for step 2.

In step 4 the production and loss of NO by reactions 5 and 25 are completed using the solutions described in Reference 4-2.

In steps 2, 3, and 4 the appropriate changes in neutral species are made to maintain conservation of atoms and the energy released by each reaction is determined in order to modify the pressure and gas temperature at the end of the time interval.

Since it is possible to significantly reduce the $N(^2D)$ relative to the $N(^4S)$ in steps 2 and 3, it is necessary to estimate the equilibration of $N(^4S)$ and $N(^2D)$ to prevent oscillation in the predicted species concentrations. In performing this estimate the electron density is assumed constant with a value equal to that at the end of the time interval. This prevents using electrons for equilibration that were used in the formation of the nitrogen atoms.

REFERENCES

- 4-1. Knapp, W.S., et al, *Weapon Output, Energy Deposition, and Atmospheric Chemistry Models for ROSCOE, Volume 1: Atmospheric Chemistry Models*, General Electric—TEMPO, December 1974 (to be published by DNA, probably under document number DNA3964F-10).
- 4-2. Jordano, R.J., *Low Altitude External Chemistry*, Section 7 of a report to DNA describing new models for ROSCOE, General Electric—TEMPO, in preparation.
- 4-3. Hamlin, D., private communication describing new ambient atmosphere models being prepared for ROSCOE, Science Applications Incorporated.
- 4-4. Niles, F.E., and M. Heap, private communication, Atmospheric Sciences Laboratory, U.S. Army Electronics Research and Development Command, April 1978.
- 4-5. Scheibe, M., private communication, Mission Research Corporation, July 1978.
- 4-6. Hamlin, D.A. et al, *The ROSCOE Manual, Volume 17 - High Altitude Debris-Energy Deposition*, DNA3964F-17, Science Applications, Inc., 27 September 1975.
- 4-7. Scheibe, M., *An Analytic Model for Nuclear Induced D-region Chemistry*, DNA2920F, MRC-R-24, Mission Research Corporation, October 1972.

SECTION 5 POST STABILIZATION DEBRIS MODELS

INTRODUCTION

In the current WEPH code the debris cloud location and size after stabilization are computed from one of two models selected as a user input option. One model neglects motion of the debris center and determines debris expansion analytically in terms of an empirical wind velocity profile. The second model determines the location and size of the debris region from a numerical evaluation of debris motion in atmospheric wind fields specified as a function of location and time.

For debris stabilization altitudes above about 100 km the two models result in similar debris sizes and the center of the debris region determined numerically is generally within the debris region determined from the analytic model. However, for debris stabilization altitudes below about 60 km the debris size determined numerically is much smaller than that determined from the analytic model. The following is a brief review of the two models with suggested revisions to bring them into better agreement.

NUMERICAL MODEL

In the numerical model the location of particles separated in altitude between the bottom and top of the debris are followed in the wind field by computing their motion during N time steps from

$$\Delta X = v \Delta T \quad (5-1)$$

where ΔX is the east-west or north-south motion during a time step, v is the average east-west or north-south wind velocity at the start

of the time step and T is the duration of the time step (≈ 1 hour). At the end of N time steps the debris center is determined as the center of the particles and the debris radius is determined from the particle dispersion.

For east-west motion let

\bar{X} = location of debris center at T hours ($\Delta T = \frac{T}{N}$)

σ_x = standard deviation of debris center at T hours .

If the wind velocities at the start of each time step are uncorrelated, then (see, for example Reference 5-1)

$$\sigma_x = \sqrt{\sigma_{v1}^2 + \sigma_{v2}^2 + \dots + \sigma_{vN}^2} \Delta T \quad (5-2)$$

where

σ_{vi} = standard deviation for the velocity at the start of the i th time step

for

$$\sigma_{v1} = \sigma_{v2} = \dots = \sigma_{vN} = \sigma_v$$

$$\sigma_x = \sqrt{N} \sigma_v \Delta T = \frac{\sigma_v T}{\sqrt{N}} .$$

If the wind velocities at the start of each time step are correlated, then

$$\sigma_x = (\sigma_{v1} + \sigma_{v2} + \dots + \sigma_{vN}) \Delta T \quad (5-3)$$

and for equal standard deviations

$$\sigma_x = N \sigma_v \Delta T = \sigma_v T . \quad (5-4)$$

In Reference 5-2 variations of wind velocities from the mean are described in terms of small scale and large scale components. The large scale component is related to tides, gravity waves and planetary waves, and the small scale component is related to turbulence. In the

horizontal direction the small scale correlation distances vary from about 20 km at the surface to about 150 km at 100 km altitude and the large scale correlation distances vary from about 900 km at the surface to about 1500 km at 100 km altitude. The small and large scale standard deviations are related to the total standard deviation by (see Reference 5-2)

$$\sigma_L^2 = f_L \sigma_T^2$$

$$\sigma_S^2 = (1 - f_L) \sigma_T^2$$

where

σ_T = total standard deviation

σ_L, σ_S = large and small scale standard deviations respectively.

The fraction f_L of the total variance contained in the large scale variance is given in Reference 5-2 as a function of altitude and latitude and varies from about 0.85 at 20 km altitude to 0.65 at 100 km altitude.

Assuming that the step sizes used in computing the debris location are large in comparison to the small scale correlation distance and small in comparison to the large scale correlation distance, σ_x becomes

$$\sigma_x = \sqrt{0.25(\sigma_{v1}^2 + \sigma_{v2}^2 + \dots + \sigma_{vN}^2) \Delta T + \sqrt{0.75}(\sigma_{v1} + \sigma_{v2} + \dots + \sigma_{vN}) \Delta T} \quad (5-5)$$

where f_L has been chosen as 0.75 and σ_{vi} is the total standard deviation at the start of the i th step. For equal standard deviations

$$\sigma_x = 0.5 \frac{\sigma_v T}{\sqrt{N}} + 0.87 \sigma_v T \quad (5-6)$$

Thus, since there is a high degree of correlation in the wind velocity in regions of about 1000 km, the standard deviation of the debris center is essentially the same as for perfect correlation. This results in a considerably larger uncertainty in determining the location of the debris centers than indicated in Reference 5-1 where uncorrelated velocities were assumed.

The debris radius in the numerical model is found in terms of the particle displacement. The east-west debris diameter is found from

$$D_{EW} = |\bar{X}_a - \bar{X}_b| \quad (5-7)$$

where

\bar{X}_a, \bar{X}_b = location of the two particles having the greatest east-west separation after N time steps.

While this is a reasonable estimate of the debris size when the horizontal velocities at different altitudes are correlated, it can underestimate the size when the velocities are uncorrelated. In Reference 5-2 the small scale vertical correlation distance is given as about 4 km and the large scale correlation distance as about 30 km (mid-latitudes). Thus, for typical debris regions the particles are separated by a distance comparable to or larger than the small scale correlation distance and less than the large scale correlation distance.

Let

$$Z = X_a - X_b$$

\bar{X}_a, \bar{X}_b = mean position of X_a and X_b

σ_{xa}, σ_{xb} = standard deviations of the uncorrelated variation in X_a and X_b .

Then

$$\bar{Z} = \bar{X}_a - \bar{X}_b, \quad \bar{X}_a > \bar{X}_b \quad (5-9)$$

$$\sigma_Z = \sqrt{\sigma_{xa}^2 + \sigma_{xb}^2} \quad (5-10)$$

Assuming a normal distribution for Z the mean value of D_{ew} is derived as (see Appendix C)

$$\bar{D}_{EW} = \bar{Z} \left\{ 1 - 2F \left(-\frac{\bar{Z}}{\sigma_Z} \right) \right\} + \frac{2\sigma_Z}{\sqrt{2\pi}} e^{-\frac{1}{2} \left(\frac{\bar{Z}}{\sigma_Z} \right)^2} \quad (5-11)$$

where

$$F(X) = \frac{1}{\sqrt{2\pi}} \int_{-\infty}^x e^{-\frac{t^2}{2}} dt \quad .$$

Note that for $\bar{Z} = 0$

$$\bar{D}_{EW} = \frac{2\sigma_Z}{\sqrt{2\pi}} \quad (5-12)$$

In order to estimate the mean debris spread from velocity data (standard deviation data are not currently modeled in the WEPH code) the variance in velocity is assumed to be the same at each altitude within the debris region and equal to the value of the largest velocity.

$$\sigma_{vi} = v_{mi} \quad (5-13)$$

where v_{mi} is the largest velocity at the start of the i th step. Then,

$$\sigma_Z = \sqrt{2} \sigma_x \quad (5-14)$$

$$\sigma_x^2 = 0.25(v_{m1}^2 + v_{m2}^2 + \dots + v_{mN}^2)(\Delta T)^2 \quad (5-15)$$

where as before the quantity $1 - f_L$ is taken as 0.25. The average east-west diameter becomes

$$\bar{D}_{EW} \approx \bar{z} \left\{ 1 - 2F\left(-\frac{\bar{z}}{z}\right) \right\} + \frac{1}{\sqrt{\pi}} \sqrt{v_{m1}^2 + v_{m2}^2 + \dots + v_{mN}^2} \Delta T_e - \frac{1}{2} \left(\frac{\bar{z}}{\sigma_z} \right)^2 \quad (5-16)$$

or considering the approximations

$$\bar{D}_{EW} \approx \bar{z} + \frac{1}{\sqrt{\pi}} \sqrt{v_{m1}^2 + v_{m2}^2 + \dots + v_{mN}^2} \Delta T_e - \frac{1}{2} \left(\frac{\bar{z}}{\sigma_z} \right)^2 \quad (5-17)$$

A similar calculation is made for the north-south debris diameter and the debris radius computed from

$$\bar{R} = R_S + \frac{1}{2} \left[\frac{\bar{D}_{EW}}{2} + \frac{\bar{D}_{NS}}{2} \right] \quad (5-18)$$

where

R_S = debris radius at stabilization time.

Figure 5-1 shows comparisons of the debris radii computed from the current model and from the above relations.

ANALYTIC MODEL

In the analytic model the debris radius is computed from

$$R = R_S + v_w (T - T_S) \quad (5-19)$$

where

$$v_w = v_{wp} \min \left[1, \frac{D_V(T_S)}{H_{wp}} \right]$$

v_{wp} = characteristic wind speed at the debris stabilization altitude

$D_V(T_S)$ = vertical dimension of the debris at the stabilization time

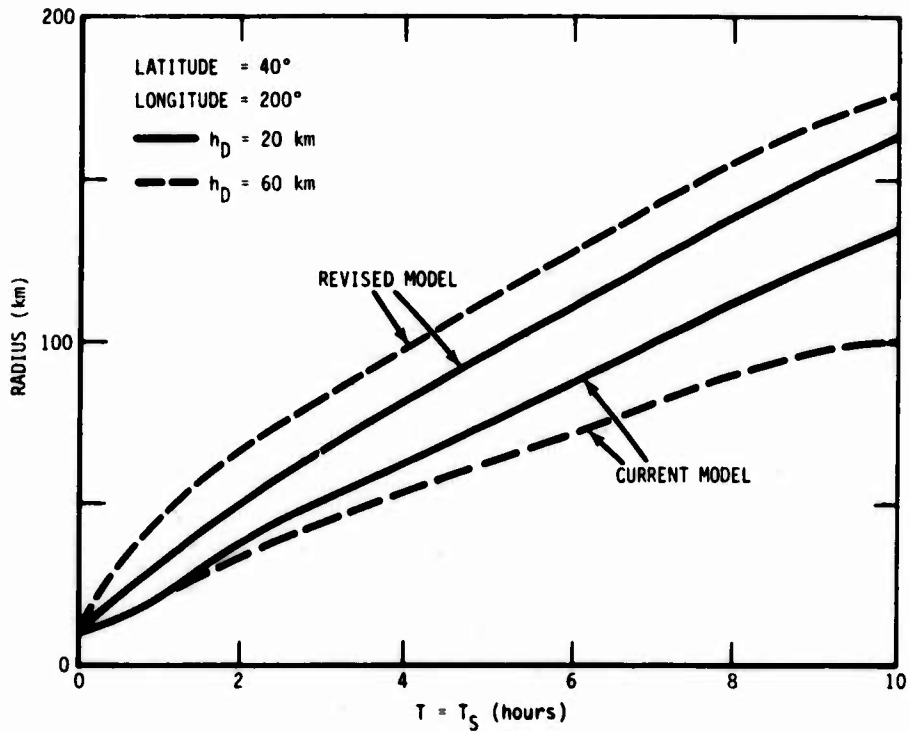


Figure 5-1. Comparison of current and revised numerical models.

H_{wp} = the characteristic distance over which the wind either changes direction or velocity sufficiently to disperse the debris, taken as 10 km.

The profile of the wind speed is assumed to be

$$v_{wp} = \begin{cases} 0.01 + 0.02 \frac{h_D}{15} \text{ km/sec} & 0 < h_D < 15 \\ 0.03 - 0.02 \frac{h_D - 15}{15} & 15 < h_D < 30 \\ 0.01 + 0.04 \frac{h_D - 30}{50} & 30 < h_D < 80 \\ 0.05 & h_D > 80 \end{cases} \quad (5-20)$$

where h_D is the debris stabilization altitude.

The above model predicts much larger debris regions at low altitudes than the numerical model due to overestimating the amount of wind shear and neglecting the difference in east-west and north-south velocities. In order to reduce the debris expansion the following revised model is proposed. For times after debris stabilization compute the debris radius from

$$R = R_S + \frac{1}{2} v_w (1 + r_w) (T - T_S) \quad (5-21)$$

where

v_w = effective east-west debris spreading velocity

r_w = ratio of the north-south to east-west wind velocity.

The proposed debris spreading velocity is

$$v_w = v_{wp} \min \left[1, \frac{D_V(T_S)}{H_{wp}} \right] \quad (5-22)$$

where

$$v_{wp} = \begin{cases} 0.01 & \text{km/sec} & h_D \leq 60 \\ -0.11 + 0.002 h_D & & 60 < h_D < 80 \\ 0.05 & & h_D \geq 80 \end{cases}$$

and $D_V(T_S)$ and H_{wp} are as previously defined. The proposed velocity ratio is

$$r_w = \begin{cases} 0.2 & & h_D \leq 60 \\ -2.2 + 0.04 h_D & & 60 < h_D < 80 \\ 1 & & h_D \geq 80 \end{cases} \quad (5-23)$$

Figure 5-2 shows comparisons of debris radii computed from the current and revised analytical models. Also shown on Figure 5-2 is the debris radii for the revised numerical model. The proposed changes result in nearly equal debris expansions for the analytical and numerical models.

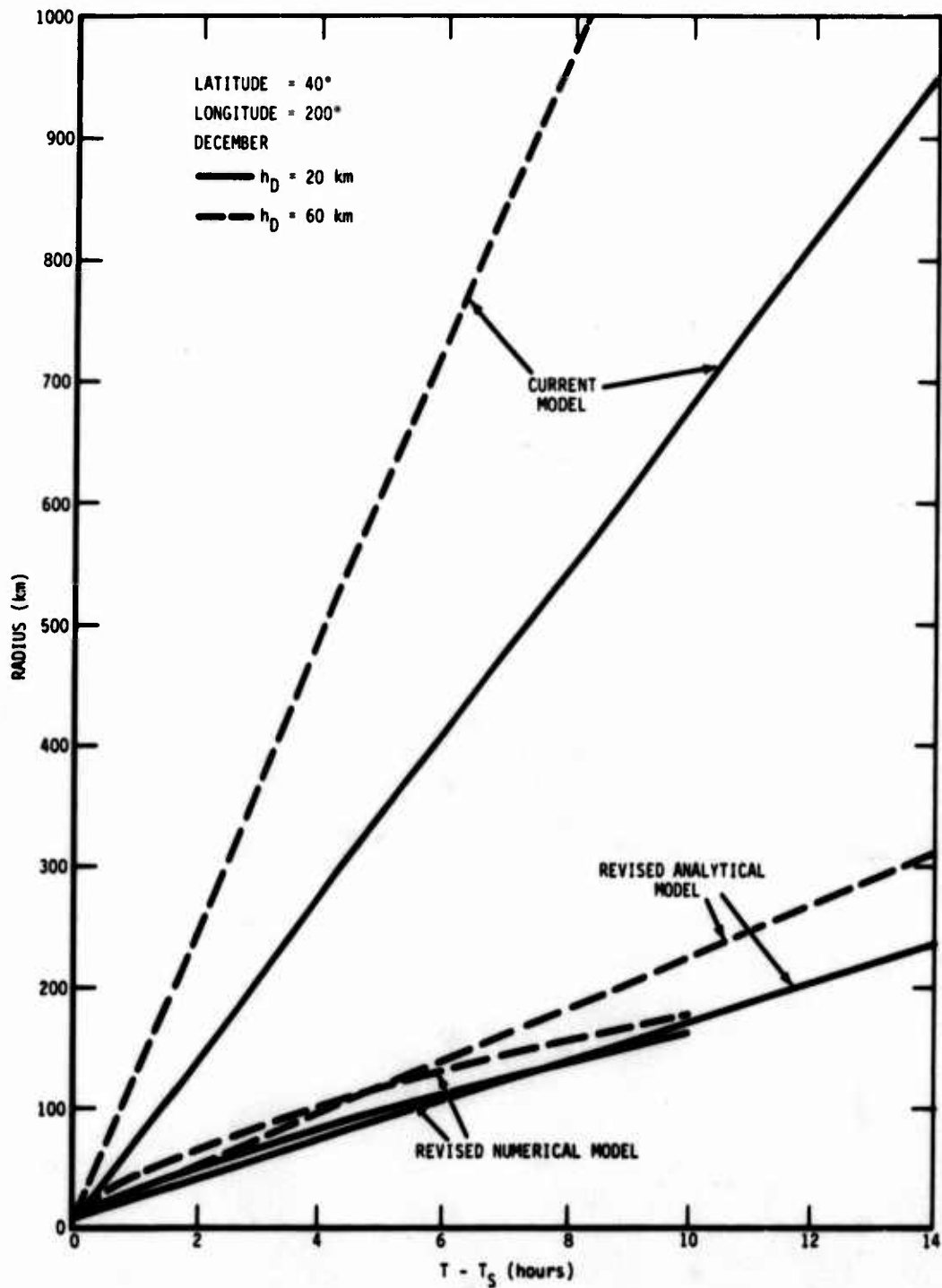


Figure 5-2. Comparison of current and revised analytic models.

REFERENCES

- 5-1. Gutsche, S.L., *A Simple Statistical Treatment of Cloud Movement*, Mission Research Corporation, September 1976.
- 5-2. Justus, C.G., and W.R. Hargraves, *The Global Reference Atmosphere Model—MOD 2 (With Two Scale Perturbation Model)*, School of Aerospace Engineering, Georgia Institute of Technology, Atlanta, Georgia, prepared for NASA George C. Marshal Space Flight Center, July 1976.

APPENDIX A
REACTIONS AND REACTION RATE COEFFICIENTS
USED IN D-REGION CHEMISTRY MODEL

The following reactions and reaction rate coefficients are for use in the D-region chemistry model (see Section 4). The reaction rate coefficients given are in the form

$$k = A \left(\frac{T}{300} \right)^B e^{-c/T} .$$

Reactions	Current Code Values			Revised Code Values		
	A	B	C	A	B	C
Neutral Species Reactions:						
1 $O_3 + hv \rightarrow O_2 + O$						
2 $O_3 + hv \rightarrow O_2(^1\Delta) + O$						
3 $O_2 + hv \rightarrow O + O$						
4 $NO_2 + hv \rightarrow NO + O$						
5 $N(^2D) + O_2 \rightarrow NO + O$	7.0[-12]*	-0.5		7.5[-12]	0.5	
6 $O_2(^1\Delta) \rightarrow O_2 + hv$	2.6[-4]			U†		
7 $O_2(^1\Delta) + N \rightarrow O_2 + N$	3.0[-15]			2.0[-14]		600
8 $O_2(^1\Delta) + N_2 \rightarrow O_2 + N_2$	1.0[-20]			0		
9 $O_2(^1\Delta) + O \rightarrow O_2 + O$	1.0[-16]			0		
10 $O_2(^1\Delta) + O_2 \rightarrow 2O_2$	2.2[-18]	0.8		U		
11 $O_2(^1\Delta) + O_3 \rightarrow O_2 + O_2 + O$	4.5[-11]		2800	U		
12 $N + NO \rightarrow N_2 + O$	1.4[-11]			4.1[-11]		410
13 $N + NO \rightarrow O(^1D) + N_2$	1.4[-11]			4.1[-11]		410
14 $N + NO_2 \rightarrow 2NO$	9.0[-12]			0		
15 $N + NO_2 \rightarrow N_2O + O$	9.0[-12]			2.0[-11]		800
16 $N + O \rightarrow NO$	1.2[-17]	-0.35		1.9[-17]	-0.35	
17 $N + O + M \rightarrow NO + M$	1.1[-32]	-0.5		U		
18 $N + O_2 \rightarrow NO + O$	3.3[-12]	1.0	3150	U		
19 $N + O_3 \rightarrow NO + O_2$	3.4[-11]	0.5	1200	3.1[-11]		1200
20 $N + O \rightarrow NO_2 + hv$	6.6[-17]	-1.9		U		

* Read 7.0[-12] as 7.0×10^{-12}

† Rate coefficient unchanged from current code value

	Reactions	Current Code Values			Revised Code Values		
		A	B	C	A	B	C
21	$\text{NO} + \text{O} + \text{M} \rightarrow \text{NO}_2 + \text{M}$	4.1[-33]		-940	1.6[-32]		-580
22	$\text{NO} + \text{O}_3 \rightarrow \text{NO}_2 + \text{O}_2$	1.5[-12]		1330	2.1[-12]		1450
23	$\text{NO}_2 + \text{O} \rightarrow \text{NO} + \text{O}_2$	9.1[-12]			U		
24	$\text{O} + \text{O}_2 + \text{M} \rightarrow \text{O}_3 + \text{M}$	1.1[-34]		-510	U		
25	$\text{O} + \text{O}_3 \rightarrow \text{O}_2(^1\Delta) + \text{O}_2$	1.0[-11]		2300	U		
26	$\text{O} + \text{O}_3 \rightarrow 2\text{O}_2$	1.0[-11]		2300	U		
27	$\text{O} + \text{OH} \rightarrow \text{H} + \text{O}_2$	Not included in current Model			4.2[-11]		
28	$\text{O} + \text{HO}_2 \rightarrow \text{OH} + \text{O}_2$				3.5[-11]		
29	$\text{O} + \text{H}_2 \rightarrow \text{H} + \text{OH}$				9.0[-12]	1.0	4500
30	$\text{OH} + \text{H}_2 \rightarrow \text{H} + \text{H}_2\text{O}$				3.6[-11]		2590
31	$\text{OH} + \text{N} \rightarrow \text{H} + \text{NO}$				5.3[-11]		
32	$\text{H} + \text{O}_3 \rightarrow \text{OH} + \text{O}_2$				1.0[-10]		520
33	$\text{H} + \text{O}_3 \rightarrow \text{HO}_2 + \text{O}$				0		
34	$\text{OH} + \text{O}_3 \rightarrow \text{HO}_2 + \text{O}_2$				1.5[-12]		1000
35	$\text{H} + \text{O}_2 + \text{M} \rightarrow \text{HO}_2 + \text{M}$				2.1[-32]		-290
36	$\text{H} + \text{NO}_2 \rightarrow \text{OH} + \text{NO}$				4.8[-10]		400
37	$\text{NO} + \text{H}_2\text{O} \rightarrow \text{NO}_2 + \text{OH}$				8.1[-12]		
38	$\text{HO}_2 + \text{O}_3 \rightarrow \text{OH} + \text{O}_2 + \text{O}_2$				1.0[-13]		1250
39	$\text{NO} + \text{OH} + \text{M} \rightarrow \text{HNO}_2 + \text{M}$				5.6[-31]*	-2.4	400
40	$\text{NO}_2 + \text{OH} + \text{M} \rightarrow \text{HNO}_3 + \text{M}$				2.2[-30] [†]	-2.5	

* Maximum 2-body rate 5.0[-12]

† Maximum 2-body rate 1.1[-11]

	Reactions	Current Code Values			Revised Code Values		
		A	B	C	A	B	C
41	$\text{NO}_2 + \text{HO}_2 \rightarrow \text{HNO}_2 + \text{O}_2$				3.0[-14]		
42	$\text{OH} + \text{HO}_2 \rightarrow \text{H}_2\text{O} + \text{O}_2$				2.0[-11]		
43	$\text{O}({}^1\Delta) + \text{H}_2\text{O} \rightarrow \text{OH} + \text{OH}$				2.3[-10]		
44	$\text{O}({}^1\Delta) + \text{N}_2 \rightarrow \text{O} + \text{N}_2$				2.5[-11]		
45	$\text{O}({}^1\Delta) + \text{O}_2 \rightarrow \text{O} + \text{O}_2$				3.0[-11]		
46	$\text{O}({}^1\Delta) + \text{H}_2 \rightarrow \text{H} + \text{OH}$				1.0[-10]		
47	$\text{O}({}^1\Delta) + \text{H}_2\text{O}_2 \rightarrow \text{OH} + \text{HO}_2$				5.2[-10]		
48	$\text{H} + \text{HO}_2 \rightarrow \text{H}_2 + \text{O}_2$				4.2[-11]		350
49	$\text{H} + \text{HO}_2 \rightarrow \text{H}_2\text{O} + \text{O}$				8.3[-11]		500
50	$\text{H} + \text{HO}_2 \rightarrow \text{OH} + \text{OH}$				4.2[-10]		950
Positive Ion and Electron Reactions:							
100	$\text{H}_3\text{O}^+ + \text{H}_2\text{O} + \text{M} \rightarrow \text{H}^+(\text{H}_2\text{O})_2 + \text{M}$	3.4[-27]	-2.0		U		
101	$\text{H}^+(\text{H}_2\text{O})_2 + \text{M} \rightarrow \text{H}_3\text{O}^+ + \text{H}_2\text{O} + \text{M}$	8.0	-2.0	18000	4.0[-1]	-5.0	17100
102	$\text{H}_3\text{O}^+ + \text{N}_2 + \text{M} \rightarrow \text{H}_3\text{O}^+(\text{N}_2) + \text{M}$	1.4[-30]	-2.0		1.4[-30]	-4.0	
103	$\text{H}_3\text{O}^+(\text{N}_2) + \text{M} \rightarrow \text{H}_3\text{O}^+ + \text{N}_2 + \text{M}$	1.2[-8]	-2.0	2780	2.0[-6]	-5.0	4500
104	$\text{H}_3\text{O}^+(\text{HO}) + \text{H}_2\text{O} \rightarrow \text{H}^+(\text{H}_2\text{O})_2 + \text{HO}$	1.4[-9]			U		
105	$\text{H}_3\text{O}^+(\text{HO}) + \text{M} \rightarrow \text{H}_3\text{O}^+ + \text{HO} + \text{M}$	1.0[-1]	-2.0	11800	5.0[1]	-5.0	13000
105A	$\text{H}_3\text{O}^+(\text{N}_2) + \text{H}_2\text{O} \rightarrow \text{H}^+(\text{H}_2\text{O})_2 + \text{N}_2$	1.0[-9]			U		
106	$\text{H}^+(\text{H}_2\text{O})_2 + \text{H}_2\text{O} + \text{M} \rightarrow \text{H}^+(\text{H}_2\text{O})_3 + \text{M}$	2.3[-27]	-2.0		2.3[-27]	-4.0	
107	$\text{H}^+(\text{H}_2\text{O})_3 + \text{M} \rightarrow \text{H}^+(\text{H}_2\text{O})_2 + \text{H}_2\text{O} + \text{M}$	1.0[-1]	-2.0	11200	8.0[-2]	-5.0	11000
108	$\text{H}^+(\text{H}_2\text{O})_3 + \text{H}_2\text{O} + \text{M} \rightarrow \text{H}^+(\text{H}_2\text{O})_4 + \text{M}$	2.4[-27]	-2.0		2.4[-27]	-4.0	
109	$\text{H}^+(\text{H}_2\text{O})_4 + \text{M} \rightarrow \text{H}^+(\text{H}_2\text{O})_3 + \text{H}_2\text{O} + \text{M}$	1.0[-1]	-2.0	8600	5.6[-2]	-5.0	8360
110	$\text{H}^+(\text{H}_2\text{O})_4 + \text{H}_2\text{O} + \text{M} \rightarrow \text{H}^+(\text{H}_2\text{O})_5 + \text{M}$	8.8[-28]	-2.0		9.0[-28]	-4.0	
111	$\text{H}^+(\text{H}_2\text{O})_5 + \text{M} \rightarrow \text{H}^+(\text{H}_2\text{O})_4 + \text{H}_2\text{O} + \text{M}$	3.0[-3]	-2.0	6000	2.8[-1]	-5.0	7700
112	$\text{N}^+ + \text{O}_2 \rightarrow \text{O}_2^+ + \text{N}({}^2\text{D})$	3.0[-10]			U		
113	$\text{N}^+ + \text{O}_2 \rightarrow \text{NO}^+ + \text{O}$	3.0[-10]			U		
114	$\text{NO}^+ + \text{CO}_2 + \text{M} \rightarrow \text{NO}^+(\text{CO}_2) + \text{M}$	2.0[-29]	-2.0		7.0[-30]	-3.0	
115	$\text{NO}^+(\text{CO}_2) + \text{M} \rightarrow \text{NO}^+ + \text{CO}_2 + \text{M}$	1.0[-8]	-2.0	5000	3.8[-6]	-4.0	4590

	Reactions		Current Code Values			Revised Code Values		
			A	B	C	A	B	C
116	$\text{NO}^+ + \text{H}_2\text{O} + \text{M}$	$\rightarrow \text{NO}^+(\text{H}_2\text{O}) + \text{M}$	1.5[-28]	-2.0		1.8[-28]	-4.7	
117	$\text{NO}^+ + \text{N}_2 + \text{M}$	$\rightarrow \text{NO}^+(\text{N}_2) + \text{M}$	2.0[-31]	-2.0		2.0[-31]	-4.4	
118	$\text{NO}^+(\text{N}_2) + \text{M}$	$\rightarrow \text{NO}^+ + \text{N}_2 + \text{M}$	1.2[-8]	-2.0	2780	6.3[-8]	-5.4	2450
119	$\text{NO}^+(\text{CO}_2) + \text{H}_2\text{O}$	$\rightarrow \text{NO}^+(\text{H}_2\text{O}) + \text{CO}_2$	1.0[-9]			U		
120	$\text{NO}^+(\text{H}_2\text{O}) + \text{HO}$	$\rightarrow \text{H}_3\text{O}^+ + \text{NO}_2$	1.0[-9]			6.0[-11]		
121	$\text{NO}^+(\text{H}_2\text{O}) + \text{HO}_2$	$\rightarrow \text{H}_3\text{O}^+ + \text{NO} + \text{O}_2$	1.0[-9]			1.0[-10]		
122	$\text{NO}^+(\text{H}_2\text{O}) + \text{H}_2\text{O} + \text{M}$	$\rightarrow \text{NO}^+(\text{H}_2\text{O})_2 + \text{M}$	1.1[-27]	-2.0		1.1[-27]	-4.7	
123	$\text{NO}^+(\text{H}_2\text{O})_2 + \text{M}$	$\rightarrow \text{NO}^+(\text{H}_2\text{O}) + \text{H}_2\text{O} + \text{M}$	1.0[-4]	-2.0	7000	9.7[-3]	-5.7	8100
124	$\text{NO}^+(\text{H}_2\text{O})_2 + \text{H}_2\text{O} + \text{M}$	$\rightarrow \text{NO}^+(\text{H}_2\text{O})_3 + \text{M}$	1.6[-27]	-2.0		1.0[-27]	-4.7	
125	$\text{NO}^+(\text{H}_2\text{O})_3 + \text{M}$	$\rightarrow \text{NO}^+(\text{H}_2\text{O})_2 + \text{H}_2\text{O} + \text{M}$	2.0[-2]	-2.0	7000	1.2[-2]	-5.7	6800
126	$\text{NO}^+(\text{H}_2\text{O})_3 + \text{H}_2\text{O}$	$\rightarrow \text{H}^+(\text{H}_2\text{O})_3 + \text{HNO}_2$	7.0[-11]			U		
127	$\text{NO}^+(\text{N}_2) + \text{CO}_2$	$\rightarrow \text{NO}^+(\text{CO}_2) + \text{N}_2$	1.0[-9]			U		
128	$\text{NO}^+(\text{N}_2) + \text{H}_2\text{O}$	$\rightarrow \text{NO}^+(\text{H}_2\text{O}) + \text{N}_2$	1.0[-9]			U		
129	$\text{NO}_2^+ + \text{NO}$	$\rightarrow \text{NO}^+ + \text{NO}_2$	2.9[-10]			U		
130	$\text{N}_2^+ + \text{O}_2$	$\rightarrow \text{O}_2^+ + \text{N}_2$	5.0[-11]	-0.5		5.0[-11]	-0.8	
131	$\text{O}^+ + \text{N}_2$	$\rightarrow \text{NO}^+ + \text{N}$	1.2[-12]	-0.5		1.2[-12]	-1.0	
132	$\text{O}^+ + \text{N}_2 + \text{M}$	$\rightarrow \text{NO}^+ + \text{N} + \text{M}$	1.6[-29]	-2.0		6.0[-29]	-2.0	
133	$\text{O}^+ + \text{O}_2$	$\rightarrow \text{O}_2^+ + \text{O}$	2.0[-11]	-0.5		2.0[-11]	-0.4	
134	$\text{O}_2^+ + \text{H}_2\text{O} + \text{M}$	$\rightarrow \text{O}_2^+(\text{H}_2\text{O}) + \text{M}$	2.8[-28]	-2.0		U		
135	$\text{O}_2^+ + \text{N}$	$\rightarrow \text{NO}^+ + \text{O}$	1.8[-10]			1.2[-10]		

	Reactions		Current Code Values			Revised Code Values		
			A	B	C	A	B	C
136	O_2^+	$+ NO \rightarrow NO^+ + O_2$	6.3[-10]			4.5[-10]		
137	O_2^+	$+ NO_2 \rightarrow NO_2^+ + O_2$	6.6[-10]			U		
138	O_2^+	$+ NO_2 \rightarrow NO^+ + O_3$	1.0[-11]			U		
139	O_2^+	$+ N_2 \rightarrow NO^+ + NO$	1.0[-16]			U		
140	O_2^+	$+ N_2 + M \rightarrow O_2^+(N_2) + M$	8.0[-31]	-2.0		9.0[-31]	-2.0	
141	$O_2^+(N_2)$	$+ M \rightarrow O_2^+ + N_2 + M$	2.0[-11]			U		
142	O_2^+	$+ O_2 + M \rightarrow O_4^+ + M$	2.8[-30]	-2.0		3.9[-30]	-3.2	
143	O_4^+	$+ M \rightarrow O_2^+ + O_2 + M$	5.0[-7]	-2.0	5000	2.0[-5]	-4.2	5400
144	$O_2^+(H_2O)$	$+ H_2O \rightarrow H_3O^+ + HO + O_2$	2.0[-10]			U		
145	$O_2^+(H_2O)$	$+ H_2O \rightarrow H_3O^+(HO) + O_2$	1.0[-9]			U		
146	$O_2^+(H_2O)$	$+ NO \rightarrow NO^+ + H_2O + O_2$	1.0[-10]			U		
147	$O_2^+(H_2O)$	$+ O_2(^1\Delta) \rightarrow O_2^+ + H_2O + O_2$	1.0[-10]			U		
148	$O_2^+(N_2)$	$+ O_2 \rightarrow O_4^+ + N_2$	1.0[-9]			U		
149	O_4^+	$+ H_2O \rightarrow O_2^+(H_2O) + O_2$	1.5[-9]			U		
150	$O_2^+(H_2O)$	$+ O_2 \rightarrow O_4^+ + H_2O$	2.0[-10]		2300	U		
151	O_4^+	$+ NO \rightarrow NO^+ + 2O_2$	5.0[-10]			U		
152	O_4^+	$+ NO_2 \rightarrow NO_2^+ + 2O_2$	5.0[-10]			U		
153	O_4^+	$+ O \rightarrow O_2^+ + O_3$	3.0[-10]			U		
154	$H^+(H_2O)_3$	$+ e \rightarrow H + 3H_2O$	4.0[-6]			5.1[-6]		
155	$H^+(H_2O)_4$	$+ e \rightarrow H + 4H_2O$	4.9[-6]			6.1[-6]		

	Reactions			Current Code Values			Revised Code Values		
				A	B	C	A	B	C
156	$H^+(H_2O)_5 + e$	$\rightarrow H + 5H_2O$	6.0[-6]			7.4[-6]			
157	$NO^+ + e$	$\rightarrow \frac{3}{4}N(^2D) + \frac{1}{4}N + O$	4.0[-7]	-1.0		U			
158	$NO^+(H_2O)_2 + e$	$\rightarrow 2H_2O + NO$	2.0[-6]	-1.0		2.0[-6]	-0.2		
159	$NO^+(H_2O)_3 + e$	$\rightarrow 3H_2O + NO$	3.0[-6]	-1.0		5.0[-6]	-0.2		
160	$NO^+(N_2) + e$	$\rightarrow NO + N_2$	1.0[-6]	-1.0		1.5[-6]			
161	$N_2^+ + e$	$\rightarrow N(^2D) + N$	2.7[-7]	-0.2		2.7[-7]			
162	$O_2^+ + e$	$\rightarrow O(^1D) + O$	2.1[-7]	-0.7		2.1[-7]	-0.63		
163	$O_2^+(H_2O) + e$	$\rightarrow H_2O + O_2$	1.5[-6]	-1.0		1.5[-6]	-0.2		
164	$O_4^+ + e$	$\rightarrow 2O_2$	2.0[-6]	-1.0		U			
165	$e + NO_2$	$\rightarrow NO_2^-$	4.0[-11]			U			
166	$e + O_2 + N_2$	$\rightarrow O_2^- + N_2$	1.0[-31]			U			
167	$O_2^- + N_2$	$\rightarrow e + O_2 + N_2$	1.9[-12]	1.5	4990	U			
168	$e + O_2 + O_2$	$\rightarrow O_2^- + O_2$	1.4[-29]	-1.0	600	U			
169	$O_2^- + O_2$	$\rightarrow e + O_2 + O_2$	2.7[-10]	0.5	5590	1.9[-10]	0.5	5600	
170	$e + O_3$	$\rightarrow O^- + O_2$	9.0[-12]	1.5		U			
171	$O^- + N$	$\rightarrow e + NO$	2.2[-10]			U			
172	$O^- + NO$	$\rightarrow e + NO_2$	2.0[-10]			2.5[-10]	-0.8		
173	$O^- + O$	$\rightarrow e + O_2$	2.0[-10]			U			
174	$O^- + O_2(^1\Delta_g)$	$\rightarrow e + O_3$	3.0[-10]			U			
175	$O_2^- + N$	$\rightarrow e + NO_2$	3.0[-10]			U			

	Reactions	Current Code Values			Revised Code Values		
		A	B	C	A	B	C
176	$O_2^- + O \rightarrow e + O_3$	3.0	[-10]		1.5	[-10]	
177	$O_2^- + O_2(^1\Delta_g) \rightarrow e + 2O_2$	2.0	[-10]		U		
178	$O + e \rightarrow O^- + h\nu$	1.3	[-15]		U		
179	$e + O_2 \cdot H_2O \rightarrow O_2^- + H_2O$	1.4	[-29]		U		
Negative Ion Reactions:							
200	$CO_3^- + H_2O + M \rightarrow CO_3^-(H_2O) + M$	1.0	[-28]	-1.0	U		
201	$CO_3^- + NO \rightarrow NO_2^- + CO_2$	1.8	[-11]		1.1	[-11]	-1.1
202	$CO_3^- + NO_2 \rightarrow NO_3^- + CO_2$	8.0	[-11]		2.0	[-10]	
203	$CO_3^- + O \rightarrow O_2^- + CO_2$	8.0	[-11]		1.1	[-10]	
204	$CO_3^-(H_2O) + NO \rightarrow NO_2^-(H_2O) + CO_2$	1.8	[-11]		7.0	[-12]	
205	$CO_4^- + H_2O + M \rightarrow CO_4^-(H_2O) + M$	5.0	[-29]	-1.0	U		
206	$CO_4^- + NO \rightarrow NO_3^- + CO_2$	4.8	[-11]		U		
207	$CO_4^- + O \rightarrow CO_3^- + O_2$	1.5	[-10]		U		
208	$CO_4^- + O_3 \rightarrow O_3^- + CO_2 + O_2$	1.3	[-10]		U		
209	$CO_4^-(H_2O) + NO \rightarrow NO_3^-(H_2O) + CO_2$	5.0	[-10]		1.0	[-11]	
210	$NO_2^- + H_2O + M \rightarrow NO_2^-(H_2O) + M$	1.3	[-28]	-1.0	U		
211	$NO_2^- + NO_2 \rightarrow NO_3^- + NO$	4.0	[-12]		2.0	[-13]	
212	$NO_2^- + O_3 \rightarrow NO_3^- + O_2$	1.8	[-11]		9.0	[-11]	
213	$NO_2^-(H_2O) + O_3 \rightarrow NO_3^-(H_2O) + O_2$	5.0	[-10]		1.0	[-11]	
214	$NO_3^- + H_2O + M \rightarrow NO_3^-(H_2O) + M$	7.5	[-29]	-1.0	U		
215	$O^- + CO_2 + M \rightarrow CO_3^- + M$	3.1	[-28]	-1.0	U		

	Reactions		Current Code Values			Revised Code Values		
			A	B	C	A	B	C
216	$O^- + NO_2$	$\rightarrow NO_2^- + O$	1.2[-9]			U		
217	$O^- + O_2 + M$	$\rightarrow O_3^- + M$	1.1[-30]	-1.0		U		
218	$O^- + O_3$	$\rightarrow O_3^- + O$	5.3[-10]			U		
219	$O_2^- + CO_2 + M$	$\rightarrow CO_4^- + M$	2.0[-29]	-1.0		U		
220	$O_2^- + H_2O + M$	$\rightarrow O_2^-(H_2O) + M$	3.0[-28]	-1.0		U		
221	$O_2^- + N$	$\rightarrow O^- + NO$	1.0[-10]			U		
222	$O_2^- + NO_2$	$\rightarrow NO_2^- + O_2$	8.0[-10]			1.2[-9]		
223	$O_2^- + O$	$\rightarrow O^- + O_2$	3.3[-10]			1.5[-10]		
224	$O_2^- + O_2 + M$	$\rightarrow O_4^- + M$	3.5[-31]	-1.0		U		
225	$O_4^- + M$	$\rightarrow O_2^- + O_2 + M$	1.0[-3]	-1.0	7500	2.0[-5]	-1.0	6300
226	$O_2^- + O_3$	$\rightarrow O_3^- + O_2$	4.0[-10]			6.0[-10]		
227	$O_2^-(H_2O) + CO_2$	$\rightarrow CO_4^- + H_2O$	5.8[-10]			U		
228	$O_2^-(H_2O) + NO$	$\rightarrow NO_3^- + H_2O$	3.1[-10]			U		
229	$O_2^-(H_2O) + O_3$	$\rightarrow O_3^- + H_2O + O_2$	3.1[-10]			2.3[-10]		
230	$O_3^- + CO_2$	$\rightarrow CO_3^- + O_2$	5.5[-10]			U		
231	$O_3^- + NO$	$\rightarrow NO_2^- + O_2$	1.0[-11]			2.8[-12]		
232	$O_3^- + NO_2$	$\rightarrow NO_2^- + O_3$	1.4[-10]			0		
233	$O_3^- + NO_2$	$\rightarrow NO_3^- + O_2$	1.4[-10]			2.8[-10]		
234	$O_3^- + O$	$\rightarrow O_2^- + O_2$	1.0[-11]			3.2[-10]		
235	$O_4^- + CO_2$	$\rightarrow CO_4^- + O_2$	4.3[-10]			U		

	Reactions		Current Code Values			Revised Code Values		
			A	B	C	A	B	C
236	$\text{CO}_4^- + \text{O}_2$	$\rightarrow \text{O}_4^- + \text{CO}_2$	4.3[-10]		3000	8.4[-12]		
237	$\text{O}_4^- + \text{H}_2\text{O}$	$\rightarrow \text{O}_2(\text{H}_2\text{O}) + \text{O}_2$	1.4[-9]			U		
238	$\text{O}_4^- + \text{NO}$	$\rightarrow \text{NO}_3^- + \text{O}_2$	2.5[-10]			0		
239	$\text{O}_4^- + \text{O}$	$\rightarrow \text{O}_3^- + \text{O}_2$	4.0[-10]			0		
240	$\text{O}_4^- + \text{O}_3$	$\rightarrow \text{O}_3^- + 2\text{O}_2$	5.0[-10]			3.0[-10]		
241	$\text{NO}_3^- + \text{NO}$	$\rightarrow \text{NO}_2^- + \text{NO}_2$	1.5[-11]			U		
242	$\text{M}^+ + \text{M}^-$	$\rightarrow \text{Products}$	2.0[-7]	-0.5		6.0[-8]		
243	$\text{M}^+ + \text{M}^- + \text{M}$	$\rightarrow \text{Products}$	5.6[-25]	-1.5		1.0[25]	-2.5	

APPENDIX B

REACTIONS AND REACTION RATE COEFFICIENTS USED IN E- AND F-REGION AND HEATED REGION CHEMISTRY MODELS

The following reactions and reaction rate coefficients are used in the E- and F-region chemistry model (see Section 4) and the heated region chemistry models (see Reference 4-1). The reaction rate coefficients given are in the form

$$k = A \left(\frac{T}{300} \right)^B e^{-c/T} .$$

Reactions			Current Code Values			Revised Code Values		
			A	B	C	A	B	C
1	$N^+ + O_2$	$\rightarrow NO^+ + O$	3.0[-10]*			U†		
2	$N^+ + O_2$	$\rightarrow O_2^+ + N$	3.0[-10]			U		
3	$N^+ + O_2$	$\rightarrow O^+ + NO$	1.0[-12]			U		
4	$N^+ + N_2$	$\rightarrow N_2^+ + N$	4.0[-11]		20060	4.0[-11]		20100
5	$N^+ + NO$	$\rightarrow NO^+ + N$	8.0[-10]			U		
6	$N^+ + O$	$\rightarrow O^+ + N$	1.0[-12]			2.6[-13]	1.0	
7	$N^+ + E$	$\rightarrow N + h\nu$	4.4[-12]	-0.75		U		
8	$N^+ + E + E$	$\rightarrow N + E$	1.2[-19]	-5.0		U		
9	$O^+ + O_2$	$\rightarrow O_2^+ + O$	2.0[-11]	-0.5		2.0[-11]		
10	$O^+ + N_2$	$\rightarrow NO^+ + N$	6.0[-14]	2.0	-900	U		
11	$O^+ + E$	$\rightarrow O + h\nu$	4.4[-12]	-0.75		U		
12	$O^+ + E + E$	$\rightarrow O + E$	1.2[-19]	-5.0		U		
13	$NO^+ + E$	$\rightarrow N(^4S) + O$	1.0[-7]	-1.0		U		
14	$NO^+ + E$	$\rightarrow N(^2D) + O$	3.0[-7]	-1.0		U		
15	$N(^4S) + O$	$\rightarrow NO^+ + E$	2.1[-13]	0.5	31900	2.1[-13]	0.5	31900
16	$N(^2D) + O$	$\rightarrow NO^+ + E$	2.4[-13]	0.5	4300	2.5[-13]	0.5	4300
17	$N + O$	$\rightarrow NO + h\nu$	1.2[-17]	-0.35		1.9[-17]	-0.35	
18	$N + N$	$\rightarrow N_2 + h\nu$	1.0[-17]	-1.0		U		
19	$N(^4S) + O_2$	$\rightarrow NO + O$	3.3[-12]	1.0	3150	U		
20	$N(^2D) + O_2$	$\rightarrow NO + O$	6.9[-12]	0.5		7.0[-12]	0.5	

* Read 3.0[-10] as 3.0×10^{-10}

† Rate coefficient unchanged from current value.

	Reactions		Current Code Values			Revised Code Values		
			A	B	C	A	B	C
21	$N(^4S) + NO$	$\rightarrow N_2 + O$	2.7[-11]			U		
22	$N(^2D) + NO$	$\rightarrow N_2 + O$	7.0[-11]			6.0[-11]	0.5	
23	$N(^4S) + E$	$\rightarrow N(^2D) + E$	1.3[-9]		26000	1.3[-9]		27700
24	$N(^2D) + E$	$\rightarrow N(^4S) + E$	5.0[-10]			U		
25	$O + N_2$	$\rightarrow NO + N$	2.5[-10]		37900	1.2[-10]		37800
26	$E + O_2 + O_2$	$\rightarrow O_2^- + O_2$	1.4[-29]	-1.0	600	U		
27	$O_2^- + O_2$	$\rightarrow E + O_2 + O_2$	2.7[-10]	0.5	5590	1.9[-10]	0.5	5600
28	$O_2^- + O$	$\rightarrow O_3 + E$	3.0[-10]			1.5[-10]		
29	$O_3 + E$	$\rightarrow O_2^- + O$	1.4[-3]	-1.98	7194	1.5[-3]	-2.5	7200
30	$O_2^- + O_2 + M$	$\rightarrow O_4^- + M$	3.5[-31]	-1.5		3.5[-31]	-1.0	
31	$O_4^- + M$	$\rightarrow O_2^- + O_2 + M$	2.1[-4]	-1.71	6230	2.0[-5]	-1.0	6300
32	$O_4^- + O$	$\rightarrow O_3^- + O_2$	4.0[-10]			0		
33	$O_3^- + O_2$	$\rightarrow O_4^- + O$	4.4[-11]	-0.23	25423	5.7[-10]	-2.0	24200
34	$O_4^- + NO$	$\rightarrow OONO^- + O_2$	2.5[-10]			0		
35	$OONO^- + O_2$	$\rightarrow O_4^- + NO$	1.8[-8]	-0.97	28338	2.5[-9]	-0.25	22900
36	$O_3^- + O$	$\rightarrow O_2^- + O_2$	1.0[-11]			2.5[-10]		
37	$O_2^- + O_2$	$\rightarrow O_3^- + O$	5.0[-11]	0.15	27711	5.0[-12]		29000
38	$O_3^- + NO$	$\rightarrow NO_2^- + O_2$	1.0[-11]			U		
39	$O_2 + NO_2^-$	$\rightarrow O_3^- + NO$	6.2[-11]	-0.09	28281	5.5[-11]		28100
40	$OONO^- + NO$	$\rightarrow NO_2^- + NO_2$	1.5[-11]			U		

Reactions			Current Code Values			Revised Code Values		
			A	B	C	A	B	C
41	$\text{NO}_2^- + \text{NO}_2$	$\rightarrow \text{OONO}^- + \text{NO}$	8.3[-13]	0.4	2167	7.0[-11]	-2.0	6300
42	$\text{O}_2^- + \text{NO}_2$	$\rightarrow \text{NO}_2^- + \text{O}_2$	8.0[-10]			1.2[-9]		
43	$\text{NO}_2^- + \text{O}_2$	$\rightarrow \text{O}_2^- + \text{NO}_2$	2.3[-9]	0.02	23769	2.5[-9]		22400
44	$\text{NO}_2 + \text{E}$	$\rightarrow \text{NO}_2^- + h\nu$	4.0[-11]			U		
45	NO_2^-	$\rightarrow \text{NO}_2 + \text{E}$	1.5[9]	1.45	28776	1.5[9]	1.5	27400
46	$\text{NO}_2^- + \text{NO}_2$	$\rightarrow \text{NO}_3^- + \text{NO}$	4.0[-12]			2.0[-13]		
47	$\text{NO}_3^- + \text{NO}$	$\rightarrow \text{NO}_2^- + \text{NO}_2$	7.2[-11]	-0.4	6113	4.0[-.2]		7600
48	$\text{X}^+ + \text{Y}^-$	$\rightarrow \text{Products}$	2.0[-7]	-0.5		6.0[-8]		
49	$\text{X}^+ + \text{Y}^- + \text{M}$	$\rightarrow \text{Products}$	5.6[-26]	-1.5		1.0[-25]	-2.5	
50	$\text{Al}^+ + \text{E} + \text{M}$	$\rightarrow \text{Al} + \text{M}$	3.2[-28]	-1.5		U		
51	$\text{UO}_2^+ + \text{E}$	$\rightarrow \text{U} + \text{O}_2$	1.6[-7]	-1.0	54200	U		
52	$\text{UO}_2^+ + \text{E}$	$\rightarrow \text{U} + \text{O}$	1.0[-6]		24600	U		
53	$\text{UO}_2^+ + \text{E}$	$\rightarrow \text{UO} + \text{O}$	1.3[-4]	-3.0	22300	U		
54	$\text{U}^+ + \text{E} + \text{M}$	$\rightarrow \text{U} + \text{M}$	1.0[-26]	-2.5		U		
55	$\text{O} + \text{E}$	$\rightarrow \text{O}^- + h\nu$	1.3[-15]			U		
56	$\text{O}^- + \text{O}$	$\rightarrow \text{O}_2 + \text{E}$	2.0[-10]			U		
57	$\text{O}^- + \text{NO}$	$\rightarrow \text{NO}_2 + \text{E}$	2.0[-10]	-1.0		2.0[-10]	-0.8	
58	$\text{O}^- + \text{N}$	$\rightarrow \text{NO} + \text{E}$	2.2[-10]			U		
59	$\text{O}^- + \text{O}_2$	$\rightarrow \text{O}_3 + \text{E}$	2.0[-17]	3.0	4600	U		
60	$\text{AlO}_2 + \text{E} + \text{M}$	$\rightarrow \text{AlO}_2^- + \text{M}$	5.6[-29]	-1.6	600	7.0[-30]	-1.5	

	Reactions		Current Code Values			Revised Code Values		
			A	B	C	A	B	C
61	$\text{AlO}_2^- + \text{M}$	$\rightarrow \text{AlO}_2 + \text{E} + \text{M}$	7.3[-9]	-0.03	51429	1.0[-9]		50800
62	$\text{AlO}^+ + \text{E}$	$\rightarrow \text{Al} + \text{O}$	5.0[-7]	-1.0		U		
63	$\text{O} + \text{NO}_2$	$\rightarrow \text{NO} + \text{O}_2$	9.0[-12]			U		
64	$\text{NO} + \text{O}_2$	$\rightarrow \text{O} + \text{NO}_2$	6.4[-12]	-0.25	23200	1.5[-17]	-0.25	23200
65	$\text{O}_2^- + \text{NO}$	$\rightarrow \text{NO}_2^- + \text{O}$	1.0[-12]			U		
66	$\text{NO}_2^- + \text{O}$	$\rightarrow \text{O}_2^- + \text{NO}$	6.2[-6]	-1.5	3900	1.2[-9]	-1.5	3900
67	$\text{O} + \text{NO} + \text{M}$	$\rightarrow \text{NO}_2 + \text{M}$	Not included in Current Model			1.6[-32]		-580
68	$\text{NO} + \text{O}_3$	$\rightarrow \text{NO}_2 + \text{O}_2$				2.1[-12]		1450
69	$\text{O} + \text{N}_2$	$\rightarrow \text{NO} + \text{N}({}^4\text{S})$				1.23[-10]		37800
70	$\text{O} + \text{H}_2\text{O}$	$\rightarrow \text{OH} + \text{OH}$				9.5[-11]		9000
71	$\text{N}({}^4\text{S}) + \text{NO}_2$	$\rightarrow \text{N}_2\text{O} + \text{O}$				2.0[-11]		800
72	$\text{N}({}^4\text{S}) + \text{O}_3$	$\rightarrow \text{NO} + \text{O}_2$				3.1[-11]		1200
73	$\text{O} + \text{O}_2 + \text{M}$	$\rightarrow \text{O}_3 + \text{M}$				1.1[-34]		-510
74	$\text{N}_2^+ + \text{O}_2$	$\rightarrow \text{O}_2^+ + \text{N}_2$				5.0[-11]	-0.8	
75	$\text{N}_2^+ + \text{NO}$	$\rightarrow \text{NO}^+ + \text{N}_2$				3.3[-10]		
76	$\text{N}({}^4\text{S}) + \text{O}$	$\rightarrow \text{N}({}^2\text{D}) + \text{O}$				5.0[-13]	0.50	27700
77	$\text{N}({}^2\text{D}) + \text{O}$	$\rightarrow \text{N}({}^4\text{S}) + \text{O}$				2.0[-13]	0.50	
78	$\text{O} + \text{N}_2 + \text{M}$	$\rightarrow \text{N}_2\text{O} + \text{M}$				1.0[-34]		7500
79	$\text{O} + \text{N}_2\text{O}$	$\rightarrow \text{NO} + \text{NO}$				1.7[-10]		14000
80	$\text{O} + \text{OH}$	$\rightarrow \text{H} + \text{O}_2$				4.2[-11]		

	Reactions		Current Code Values			Revised Code Values		
			A	B	C	A	B	C
81	$H + O_2$	$\rightarrow OH + O$	Not included in Current Model			1.1[-9]	-0.30	8400
82	$N + NO + M$	$\rightarrow NO_2 + M$				1.0[-31]	-2.50	
83	$H + O_3$	$\rightarrow OH + O_2$				2.6[-11]		
84	$O_3 + M$	$\rightarrow O + O_2 + M$				3.8[-8]	-1.50	12200
85	$O_2^+ + NO$	$\rightarrow NO^+ + O_2$				6.3[-10]		

APPENDIX C
 PROBABILITY DISTRIBUTION OF THE ABSOLUTE
 DIFFERENCE OF TWO INDEPENDENT RANDOM VARIABLES *

Let x_1 and x_2 be two independent random variables with mean values of μ_1 and μ_2 and standard deviations of σ_1 and σ_2 . Define a new variable y by

$$y = |x_1 - x_2| .$$

The following deviation is for the mean value and standard deviation of y . First define $z = x_1 - x_2$. Then for $\mu_1 \geq \mu_2$

$$\begin{aligned} \mu_z &= \mu_1 - \mu_2 \\ \sigma_z &= \sqrt{\sigma_1^2 + \sigma_2^2} \end{aligned}$$

If we assume that z is normally distributed

$$P[z(t)] = \frac{1}{\sqrt{2\pi}\sigma_z} e^{-\frac{1}{2}\left(\frac{t - \mu_z}{\sigma_z}\right)^2}$$

then $y(t) = |z(t)|$ has the distribution

$$\begin{aligned} P[y(t)] &= P[z(t)] + P[z(-t)] \\ &= \frac{1}{\sqrt{2\pi}\sigma_z} \left[e^{-\frac{1}{2}\left(\frac{t - \mu_z}{\sigma_z}\right)^2} + e^{-\frac{1}{2}\left(\frac{-t - \mu_z}{\sigma_z}\right)^2} \right] \quad t \geq 0 \end{aligned}$$

The mean value of y is found from

* Prepared by James H. Thompson

$$\begin{aligned} \mu_y &= \int_0^{\infty} ty(t)dt = \frac{1}{\sqrt{2\pi} \sigma_z} \left\{ \int_0^{\infty} t e^{-\frac{1}{2} \left(\frac{t - \mu_z}{\sigma_z} \right)^2} dt + \int_0^{\infty} t e^{-\frac{1}{2} \left(\frac{-t - \mu_z}{\sigma_z} \right)^2} dt \right\} \\ &= \frac{1}{\sqrt{2\pi} \sigma_z} \left\{ \int_0^{\infty} t e^{-\frac{1}{2} \left(\frac{t - \mu_z}{\sigma_z} \right)^2} dt - \int_{-\infty}^0 t e^{-\frac{1}{2} \left(\frac{t - \mu_z}{\sigma_z} \right)^2} dt \right\} \end{aligned}$$

Let $s = \frac{t - \mu_z}{\sigma_z}$

then

$$\begin{aligned} \mu_y &= \frac{1}{\sqrt{2\pi} \sigma_z} \left\{ \int_{-\frac{\mu_z}{\sigma_z}}^{\infty} (s\sigma_z + \mu_z) e^{-\frac{1}{2} s^2} \sigma_z ds \right. \\ &\quad \left. - \int_{-\infty}^{-\frac{\mu_z}{\sigma_z}} (s\sigma_z + \mu_z) e^{-\frac{1}{2} s^2} \sigma_z ds \right\} \\ &= \frac{1}{\sqrt{2\pi}} \left\{ \int_{-\frac{\mu_z}{\sigma_z}}^{\infty} \mu_z e^{-\frac{1}{2} s^2} ds - \int_{-\infty}^{-\frac{\mu_z}{\sigma_z}} \mu_z e^{-\frac{1}{2} s^2} ds \right. \\ &\quad \left. + \int_{-\frac{\mu_z}{\sigma_z}}^{\infty} \sigma_z s e^{-\frac{1}{2} s^2} ds - \int_{-\infty}^{-\frac{\mu_z}{\sigma_z}} \sigma_z s e^{-\frac{1}{2} s^2} ds \right\} \end{aligned}$$

The cumulative distribution function of a standardized normal random variable is

$$F(x) = \frac{1}{\sqrt{2\pi}} \int_{-\infty}^x e^{-\frac{1}{2}t^2} dt$$

The values of $F(x)$ are listed in tables or can be found from the error function using the relation

$$F(x) = \frac{1}{2} \left[1 + \operatorname{erf} \left(\frac{x}{\sqrt{2}} \right) \right]$$

Hence

$$\mu_y = \mu_z \left\{ 1 - 2F \left(-\frac{\mu_z}{\sigma_z} \right) \right\} + \frac{2\sigma_z}{\sqrt{2\pi}} e^{-\frac{1}{2} \left(\frac{\mu_z}{\sigma_z} \right)^2}$$

Now $\sigma_y^2 = \overline{t^2} - \mu_y^2$, and

$$\begin{aligned} \overline{t^2} &= \int_0^{\infty} t^2 y(t) dt \\ &= \frac{1}{\sqrt{2\pi} \sigma_z} \left\{ \int_0^{\infty} t^2 e^{-\frac{1}{2} \left(\frac{t - \mu_z}{\sigma_z} \right)^2} dt + \int_0^{\infty} t^2 e^{-\frac{1}{2} \left(\frac{-t - \mu_z}{\sigma_z} \right)^2} dt \right\} \\ &= \frac{1}{\sqrt{2\pi} \sigma_z} \left\{ \int_0^{\infty} t^2 e^{-\frac{1}{2} \left(\frac{t - \mu_z}{\sigma_z} \right)^2} dt + \int_{-\infty}^0 t^2 e^{-\frac{1}{2} \left(\frac{t - \mu_z}{\sigma_z} \right)^2} dt \right\} \\ &= \frac{1}{\sqrt{2\pi} \sigma_z} \int_{-\infty}^{\infty} t^2 e^{-\frac{1}{2} \left(\frac{t - \mu_z}{\sigma_z} \right)^2} dt \end{aligned}$$

This is in the standard form for a normal random variable so that

$$\overline{t^2} = \sigma_z^2 + \mu_z^2, \text{ hence } \sigma_y^2 = \sigma_z^2 + \mu_z^2 - \mu_y^2$$

Hence for the variable $y = |x_1 - x_2|$

$$\mu_y = \mu_z \left\{ 1 - 2 F \left(\frac{-\mu_z}{\sigma_z} \right) \right\} + \frac{2\sigma_z}{\sqrt{2\pi}} e^{-\frac{1}{2} \left(\frac{\mu_z}{\sigma_z} \right)^2}$$

$$\sigma_y^2 = \sigma_z^2 + \mu_z^2 - \mu_y^2$$

where

$$\mu_z = \mu_1 - \mu_2 \text{ and we have assumed } \mu_1 \geq \mu_2$$

$$\sigma_z = \sqrt{\sigma_1^2 + \sigma_2^2}$$